EXPERIMENTAL STUDIES OF TURBULENT JET IGNITION: COMBUSTION VISUALIZATION AND PRESSURE TRACE ANALYSIS USING AN OPTICALLY ACCESSIBLE RAPID COMPRESSION MACHINE

By

Gerald Raymond Gentz

A DISSERTATION

Submitted to
Michigan State University
in partial fulfillment of the requirements
for the degree of

Mechanical Engineering—Doctor of Philosophy

2016

ABSTRACT

EXPERIMENTAL STUDIES OF TURBULENT JET IGNITION: COMBUSTION VISUALIZATION AND PRESSURE TRACE ANALYSIS USING AN OPTICALLY ACCESSIBLE RAPID COMPRESSION MACHINE

By

Gerald Raymond Gentz

This dissertation presents several series of experiments on turbulent jet ignition (TJI) using an optically accessible rapid compression machine (RCM), presenting pressure trace data and combustion visualization. Chapter 2 gives a detailed overview of the RCM and, and a general testing procedure. However, each series of experiments uses different TJI igniters and optical head geometries. Therefore, in the following chapters, the RCM and TJI configurations are first introduced, and then the experimental results are presented. Chapter 3 presents experimental results on TJI without any auxiliary fuel injection, using propane. Chapter 4 investigates auxiliary fueled TJI with liquid propane used as the auxiliary fuel, and gaseous propane as the main chamber fuel. Chapter 5 presents dual injector TJI experiments performed using methane as the main chamber and pre-chamber fuel. This chapter also investigates the effect of charge dilution using both nitrogen and exhaust gases. Chapter 6 utilizes an auxiliary fueled TJI system using liquid iso-octane as the auxiliary fuel. This chapter studies the effects of auxiliary fuel injection and ignition distribution due to single orifice and dual orifice nozzle geometry. Finally, Chapter 7 presents a summary of the most important experimental results, and some concluding remarks.

ACKNOWLEDGMENTS

In 2012 during my senior year in my undergraduate program here at Michigan State, I decided that I wanted to go to graduate school and get my PhD to fulfil my potential and to have a more interesting career than what I might have if I went straight into industry. I was not quite sure what I wanted to study, or if I wanted to stay at MSU or go to another University. In fact, I was considering aerospace and robotics programs, when Dr. Tonghun Lee had approached me after his combustion class one day, and asked if I would like to come out to the Engineering Research Complex for a meeting, and to consider joining his research group if it was a good fit. As it turns out, Tonghun would not be able to bring me on as his graduate students as he was going to be accepting a faculty position at the University of Illinois the next year, but he did introduce me to Dr. Elisa Toulson who was looking for a student. Elisa became my primary advisor and I am very grateful for the endless support, experience, and guidance that she has provided me during my studies, including countless revisions to the various papers that we have written together. During the first year of my PhD Tonghun also acted as a co-advisor, and provided support and guidance when needed. I would like to express my thanks to Tonghun for this support and the opportunity that he presented to me during this influential first year. I also had the chance to work with and get to know a few of his graduate students at the time, whom I respect and still consider friends. This includes Steve Hammack, Dan Valco, and Bryce Thelen. Bryce was also Tonghun's student, but chose to stay at MSU and became Elisa's students as well. Bryce has been a great friend, and someone whom I have been able to confide in. Masumeh Gholamisheeri is another one of Elisa's students that I have had a chance to work with and gotten to know very well, and I appreciate her friendship. I would also like to thank several others including Dr. Miller, Dr. Schock, and Dr. Wichman for agreeing to be a part of my research committee.

The support staff at MSU also deserves recognition, as this dissertation would not be possible without all of their hard work. Many thanks to Jeff Higel, Jen Higel, Brian Rowley, Tom Stueken, Kevin Moran, and Melissa Flegal.

TABLE OF CONTENTS

LIST OF TABLES

LIST OF FIGURES

KEY TO ABBREVIATIONS

AFR	air-fuel ratio
BDC	bottom dead center
C_2*	diatomic carbon (electronically excited)
CFD	computational fluid dynamics
CH*	methylidyne radical (electronically excited)
CH_2O*	formaldehyde (electronically excited)
CO	carbon monoxide
CO_2*	carbon dioxide (electronically excited)
FR	frame rate
HAJI	hydrogen assisted jet ignition
HC	unburned hydrocarbons
IR	infrared
JPIC	jet plume injection combustion
LAG	avalanche activated combustion
LES	large eddy simulation
LPG	liquid petroleum gas
LTC	low-Temperature Combustion
MFB	mass fraction burned
m_i	injected mass fraction
NOx	oxides of nitrogen

PM	particulate matter
R	radical Species
R*	radical species (electronically excited)
RANS	Reynolds-averaged Navier-Stokes
RCM	rapid compression machine
SI	spark ignition
TJI	turbulent jet ignition
TDC	top dead center
TDC	top dead center
UV	ultraviolet
VIS	visible
λ	air-fuel equivalence ratio

CHAPTER 1: INTRODUCTION

1.1 Background and Motivation

Improving the efficiency and reducing emissions of internal combustion engines are a top priority for engine developers. Major initiatives are currently underway in the United States to improve fuel economy, and limit the emissions of particulate matter (PM), unburned hydrocarbons (HC), carbon monoxide (CO), and oxides of nitrogen (NOx). Advanced combustion engines that operate highly dilute with either excess air or residual gases can deliver high thermal efficiencies and low emissions through low-temperature combustion (LTC) strategies [1]. However, the combustion of highly dilute mixtures and lean burn technology is challenging to implement since as the mixture becomes increasing lean, the burning speed becomes much slower and combustion starts to become unstable [2]. In this case, ignition enhancement allows for faster burning rates and increased stability either by increasing the ignition energy supplied, and/or distributing the ignition source over many ignition sites [3-5]. Turbulent jet ignition (TJI) is one such advanced ignition enhancement technique for spark ignition (SI) engines, where a jet of hot combusting gases is used as the ignition source.

1.2 Overview of Turbulent Jet Ignition

TJI is an advanced pre-chamber ignition enhancement technique for SI engines that uses one or more jets of hot combusting gases as the ignition source. With TJI, combustion is initiated in a pre-chamber by conventional spark ignition, generating a rapid increase in temperature and pressure that force combusting gases out of the pre-chamber though one or more small orifices. Heat and radical species are distributed throughout the discharging jet volume, and act as the ignition source for the main chamber charge as the unburned mixture becomes entrained. This

distributed ignition effect leads to fast burn rates and increased combustion stability [5]. Figure 1-1 gives an illustration of the TJI process due to a single jet.

Figure 1-1. Illustration of TJI with a single orifice nozzle

Figure 1-2 shows TJI initiating main chamber combustion. From the image sequence, the initial jet penetration can be seen, followed by flame propagation and interaction of the jet with the walls of the cylinder.

1.13 ms 1.25 ms 1.38 ms 1.63 ms 2.00 ms

Figure 1-2. Combustion visualization of TJI initiating main chamber combustion

The components of a simple TJI igniter consists of a pre-chamber adapter body, a spark plug, and a nozzle with one or more small orifices. For systems that utilize auxiliary fueling in the pre-chamber, a fuel injector is added to the TJI assembly, such as the one shown in Figure 1-3.

Figure 1-3. TJI assembly: fuel injector, spark plug, pre-chamber adapter body, and nozzle.

Table 1-1. Components of a TJI System

Pre-chamber adapter body
– Volume
– Aspect ratio
Pre-chamber fueling strategy
– No auxiliary injection
– Auxiliary fuel injection
– Auxiliary air and fuel injection
Ignition system
– Ignition coil
– Spark plug
– Triggering circuit
TJI nozzle geometry
– Orifice diameter
– Number of orifices
– Orifice shape and orientation

Table 1-1 gives an overview of the components of a TJI system. Each aspect of a TJI system in the table deserves careful design considerations. For example, the pre-chamber is important since ignition is first initiated here by conventional spark ignition. The initial flame kernel develops into a deflagration that travels the length of the pre-chamber, compressing the unburned charge and forcing some of the unburned contents out into the main-chamber via one or more small orifices. Once the flame has reached the nozzle, then the hot products of combustion will discharge and initiate ignition in the main chamber. The volume of the pre-chamber will govern the mass of hot products that will be available to discharge and act as the ignition source for the main chamber. The aspect ratio of the pre-chamber or the ratio of the pre-chamber height to diameter will determine how far the flame front has to travel, as well as how much of the pre-chamber charge is initially consumed versus being pushed out of the main chamber. The surface area to volume ratio will govern the heat transfer losses in the pre-chamber. Any heat losses or combustion inefficiencies in the pre-chamber will propagate and directly influence the combustion in the main-cylinder since the enthalpy of the discharging jet will be diminished. The nozzle geometry is just as critical since this will determine the jet structure and distribution of heat and energy of the products into the main-chamber. If a nozzle orifice has too small of a cross sectional area, the flow may be become choked and the amount of mass that discharges from the pre-chamber may not be enough to initiate combustion. Alternatively, even if the flow is not choked, if the nozzle orifice area is too small and the resulting jet velocity is exceedingly fast, the ignition attempt may be unsuccessful due to excessive cooling and quenching by high strain rates [6]. In an engine, choked flow through the nozzle orifices will also cause an issue between cycles when trying to purge the pre-chamber cavity of residual gases.

An innovation by Schock et al. [7] to improve the TJI process in engines was to add a second injector that allows for the injection of air into the pre-chamber. By adding an injector for air, the options for controlling and tuning the combustion greatly increases. The air injection allows purging of residual gasses from the pre-chamber, creating an opposed jet flow during fuel injection to prevent wall wetting and enhance mixing, and better control of the local stoichiometry near the spark plug electrodes. This is particularly important when operating with high levels of exhaust gas recirculation, where combustion would be unstable or impossible without the additional air injection event. The dual injector TJI concept allows different TJI operating modes to be used depending on the engine conditions: TJI without auxiliary fuel injection, with auxiliary fuel injection only, or with both auxiliary air and fuel injection. Figure 4 shows an illustration of the dual injector TJI concept.

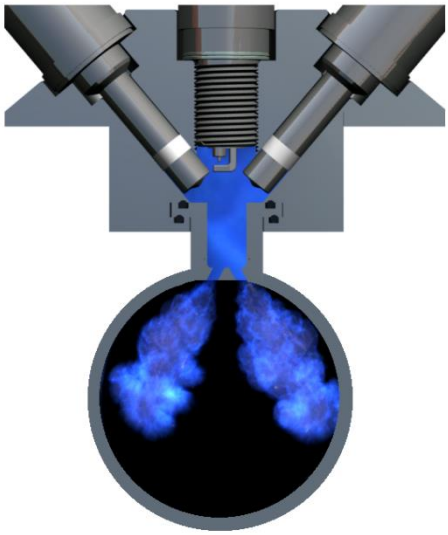

Figure 1-4. Illustration of the dual injector TJI concept with dual orifices and jets shown.

1.3 Research questions and objectives

The turbulent jet ignition process is complex, and involves coupled physics of thermal, chemical, and fluid mechanics. Further study necessary to better understand and characterize the TJI process. For instance, for a given TJI design it is difficult to know *a priori* the answers to following research questions

1. Will ignition be successful? Where does ignition occur once the jet discharges?
2. How does changing the nozzle orifice geometry affect the combustion process? More specifically, what about nozzle diameter, number of orifices, etc.?
3. How is the flow between the pre-chamber and main chamber characterized?
4. What is the lean limit of combustion? How far can TJI extend the lean limit over other ignition enhancement concepts?
5. How is the combustion due to TJI affected by increasing dilution levels (either excess air or residual gasses)?
6. Can TJI be used to control autoignition in the unburned mixture, leading to further ignition enhancement?

The work presented here attempts to address these research questions and add to the scientific body of knowledge about the jet ignition process.

1.4 Literature review

1.4.1 Ignition phenomena

Ignition describes the transition from an unburned state to an intensely burning state [8]. By definition, ignition is a transient phenomenon that deals with chemically reacting flows, the evolution of heat, and heat transfer losses to the surroundings. Fundamentally, ignition can

occur two distinct ways: either thermally due to the introduction of heat, or chemically due to chain-branching reactions [8, 9]. Quenching is closely related to ignition, and describes the opposite phenomena- a transition from a burning state to an unburned state. Quenching can occur due to removing heat from a flame, or by quenching a sufficient amount of the chain-branching radials that participate in the ignition process [10, 11].

Classical ignition theory attempts to describe the complex physics using models with one step reactions and chain reactions of a homogenous mixture [12-15]. Conceptually, it is useful to think of thermal ignition in terms of an energy balance between the heat generated and the heat lost to the surroundings, with the mixture reacting according to an Arrhenius model, causing the reaction rate to increase exponentially as the temperature increases, leading to further heat generation and ultimately resulting in a state of thermal runaway and ignition of the mixture [12]. Chemical ignition is due to a rapid rate of radical production and heat generation as a result of chain-branching reactions. This process is distinct from a purely thermal ignition in the sense that it can occur isothermally, with the possibility of the heat generated in the mixture due to exothermic reactions being dissipated by heat transfer losses to the walls [9, 13]. However, if the rate of radical production continues and chain-branching dominates, some additional heat will be evolved, and similar to the thermal ignition case thermal runaway will occur leading to ignition [8]. Of course, the literature on ignition theory only gives a model of the physics that occur. In reality the conditions during combustion will be quite different and even the most advanced ignition model will have difficulty accurately describing all of the complex phenomena including inhomogeneous mixture compositions and temperatures, turbulence, thermal expansion, chemical reaction rates, and other such effects associated with combustion. For this reason,

experimental work is often performed to characterize the ignition process for various conditions of interest, and is complementary to the fundamental theories.

Thermal ignition of a premixed fuel-air mixture can be characterized by how the heat is spatially and temporally distributed to the mixture. Kuchta [16] identified the following thermal ignition sources:

1. Electrical Spark Ignition
2. Hot Surfaces
    a. Heated vessels or walls
    b. Heated wires or rods
3. Hot Gases
    a. Adiabatic compression and shock compression
    b. Heated gas jets and pilot flames
4. Thermal radiation

For each of these thermal ignition sources, the characteristic rate of heating and the size of the ignition source vary greatly. For instance, electrical spark ignition is spatially highly localized and very high in temperature and heating rate. In contrast, for heated surfaces the heating rate and temperature is relatively low, while the surface area is large. Due to the different spatial characteristics, the ignition requirements for a highly concentrated source like spark ignition is given in terms of ignition energy, while for more distributed heat sources, the ignition requirements are given in terms of temperatures.

Ignition by hot gasses also has its own unique temporal and spatial characteristics. Shock wave heating, such as what occurs when igniting a fuel-air mixture in a shock tube, is the most localized in space in time due to the fast velocity and small thickness of the traveling shock wave that compresses and heats the fuel-air charge. Adiabatic compression ignition is more

distributed, with a slower heating rate as when using a rapid compression machine to study the chemical kinetics of fuels that exhibit auto-ignition. Another type of ignition involves a jet of hot gasses, either inert which is primarily a thermal ignition source, or a chemically active jet which will involve both thermal ignition and chemical ignition processes due to the participation of active radical species, such as during turbulent jet ignition.

It should be noted that not all fuel and air mixtures are capable of being ignited, and only a certain range of mixture strengths will allow for steady flame propagation. The critical concentrations of fuel and oxidizer are known as the limits of flammability [16, 17]. The upper limit of flammability gives the richest mixture for which a steady flame can propagate, while the lower limit, or lean limit of combustion, gives the leanest mixture that will allow for steady flame propagation. These limits are usually determined experimentally for laminar, pre-mixed flames, and are typically apparatus dependent due to heat transfer losses unique to each device. Generally, the limits of flammability are widened by increased temperature, pressure, oxygen concentration, and energy of the ignition source. The presence of turbulence and buoyancy also widen the flammability limits due to an increase in the resulting flame propagation rate [16].

Ignition enhancement refers to various techniques to improve the quality of the ignition process. Several technical papers have reviewed ignition enhancement concepts for internal combustion engines [4, 5, 18]. Of particular importance to this work is the paper written by Toulson et al. who gave a comprehensive review of pre-chamber jet ignition concepts [5].

1.4.2 Combustion and interpretation of flame color

Combustion is rapid oxidation of fuel and air mixture, generating heat or both heat and light [11]. One mode of combustion is a flame which is defined as a thin reaction zone. Generally, a

flame can be characterized as being premixed, where the reactants are well mixed at the molecular level or nonpremixed (diffusion) flames where the fuel and oxidizer are initially separated. Combustion can also occur in a non-flame mode [19], where there is not a well-defined reaction zone and ignition occurs volumetrically.

The emission of light during combustion can be used to study the physics and chemistry that are occurring, and there are various mechanisms of light emission associated with flames. Chemiluminesence is the spontaneous emission of light from electronically excited species due to a chemical reaction. During chemiluminesence, the emission of a photon occurs as an electronically excited radical species relaxes to its ground state. This photon emission can occur as a single wavelength, banded spectra, or a continuous spectrum depending on the species. Some common species that exhibit chemiluminesence in hydrocarbon flames are OH^*, CH^*, C_2^*, and CH_2O^*, where the asterisk indicates an electronically excited state.

A two-step mechanism further explains the emission of light due to chemiluminesence. Two species chemically react, and produce an excited radical and other species. This electronically excited radical species then relaxes to its ground state, releasing a photon that emits light at wavelengths characteristic of the species.

$$1.\ A + B \rightarrow R^* + others$$

$$2.\ R^* \rightarrow R + h\nu$$

Table 1-2 shows some common chemiluminescent species, the chemical reactions leading to chemiluminesence and the characteristic wavelengths at which light is emitted.

Table 1-2. Chemiluminescent species and reactions in HC flames

Species	Reactions	Wavelengths (nm)
OH*	$CH + O_2 \rightarrow CO + OH^*$ $H + O + M \rightarrow OH^* + M$	282.9, 308.9
CH^*	$C_2H + O_2 \rightarrow CO_2 + CH^*$ $C_2H + O \rightarrow CO + CH^*$	387.1, 431.4
C_2^*	$CH_2 + C = C_2^* + H_2$	513, 516.5
CO_2^*	$CO + O + M \rightarrow {CO_2}^* + M$	350-600

Figure 1-5 presents a schematic of the UV-VIS-IR spectrum for reference. It can be seen that the OH* and CH* chemiluminesence occurs near the blue and violet regions of the visible spectrum, which is what gives a premixed flame its characteristic blue hue. Apart from the direct formation of electronically excited species, species can become electronically excited due to high temperatures, which is referred to as thermal excitation. The last mechanism of light emission in a flame is due to black body radiation of solid particles such as soot. The solid particles act as black body emitters, absorbing and emitting radiation as described by Planck's law. This is what gives a diffusion flame the characteristic yellow-white color.

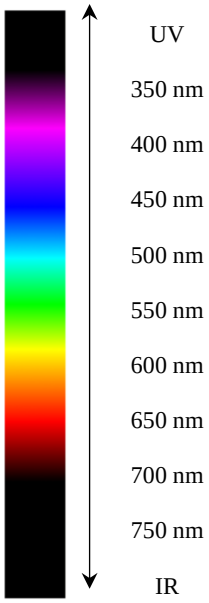

Figure 1-5. UV-VIS-IR Spectrum

1.4.3 Jet classification, dynamics and structure

In addition to the chemical and thermal processes associated with jet ignition, the physical processes due to fundamental jet dynamics will is important. Such processes include details about the transient jet development, entrainment and mixing mechanisms, regions of instability, and compressibility effects. Gholamisheeri et al. studied the behavior of transient, compressible, and combusting jets due to TJI in an RCM [20]. However, most of the literature on jets refers to the steady state processes that occur, and relatively little work has been done on transient jet development which is the most relevant to TJI.

The structure and behavior of a jet is often characterized by the pressure ratio across the nozzle or orifice. The jet is considered to be underexpanded when the jet pressure is greater than the ambient pressure, causing the jet to continue to expand after it has discharged from the nozzle [21]. An overexpanded jet occurs when the fluid exits at a lower pressure than the

ambient fluid, causing the flow to contract some distance after the nozzle. When the pressure of the jet equals the ambient pressure (referred to as an ambient or sonic jet), the velocity is axial and the jet does not expand nor contract. Furthermore, jets are classified according to if the jet is interacting with a surface or if the jet is free from any boundary interactions. In the case of no boundary interactions, the term free jet is used. When the jet is interacting with a surface, the term impinging jet or confined jet is often used. Franquet et al. [22] performed a review of free underexpanded jets in a quiescent mixture, which describes the flow conditions and jet structures, as well as introducing the most relevant mathematical descriptions for under expanded jets found in the literature.

Pawlak et al. characterized the starting jet dynamics of a laminar jet with numerical simulations and experimental observations [23]. The authors give the following detailed description of the development of a transient jet: "The initial development of a jet emanating from an orifice involves the roll-up of vortices into a vortex ring, which is trailed by a column of high-momentum fluid, subject to shear instabilities". The vortex rings and the shear instability regions are important since significant mixing occurs in these regions. With studying the jet dynamics we can gain some insight about where ignition will occur. The vortex rings and the stagnation front of the leading vortex are areas where local ignition may occur due to high spatial gradients, while ignition may be less likely to occur in areas of high strain rate [24].

1.4.4 Jet ignition literature

The concept of jet ignition was first introduced in the late 1950's in the USSR under the direction of Nikolai Semenov, who is famous for his contributions to chain reaction theory [25, 26]. Lev Gussak was one of the researchers working with Semenov to develop the first jet ignition engine. They gave the ignition concept the name LAG (Lavinaia Aktivatsia Gorenia)

which translates to "Avalanche Activated Combustion" [5, 25-29]. LAG is essentially a divided-chamber stratified-charge ignition concept that uses a chemically reacting jet of fuel-rich combustion products to initiate combustion in ultra-lean mixtures. The advantages to this combustion process include limiting the occurrence of engine knock, reducing the required fuel octane number, increasing combustion stability for lean mixtures, lowering specific fuel consumption, and decreased formation of pollutants [27]. In the pioneering experimental work on the LAG process performed by Gussak in a pre-chamber engine [27, 28], a rich mixture (λ=0.5) was delivered to the pre-chamber via a cam actuated injector, and a lean mixture of λ=2.0 was able to be ignited within the cylinder. λ is defined as the air-fuel equivalence ratio, or relative air-fuel ratio. Through extensive experiments, Gussak found that a pre-chamber volume 2-3% of the clearance volume and a total orifice area of 0.03-0.04 cm^2 per 1 cm^3 of pre-chamber volume optimized the LAG process.

Later, Oppenheim et al. [30-32] at the University of California, Berkeley developed a similar ignition concept termed Jet Plume Injection and Combustion (JPIC). The JPIC igniter is essentially a miniaturized version of the valve-operated LAG combustion system that can be installed into an engine similar to a direct injector [5, 31]. Ultra-lean mixtures of λ=2.22 could be ignited by JPIC, while the lean limit for spark ignition was determined to be λ=1.53. For nozzle diameters of 2.5 mm, 4 mm, and 6 mm, combustion performance was evaluated based on parameters of the pressure traces such as maximum pressure, and the slope of the pressure curves. Murase and Hanada [33-35], also performed extensive research on the JPIC ignition concept. In one study [35], jet ignition was used as a trigger to control the start of Homogenous Charge Compression Ignition (HCCI), with direct visualization of the jet discharging and initiating combustion.

In the 1990's, at the University of Melbourne, Watson et al. [36-38] developed a pre-chamber ignition concept named Hydrogen Assisted Jet Ignition (HAJI). HAJI is similar to the other pre-chamber jet ignition concepts mentioned in this paper; the hardware consists of a small pre-chamber and orifices, spark plug, and pre-chamber direct injector. As the name suggests, hydrogen is used as the pre-chamber fuel. Toulson et al. performed a study of the HAJI system in a single cylinder research engine with Liquefied Petroleum Gas (LPG) as an alternative pre-chamber fuel, with the LPG having a composition of 95% propane and 5% butane [37]. Main chamber fuels tested were both LPG and gasoline. In this study, the experimental lean limit was defined to be when the coefficient of variation of the indicated mean effective pressure exceeded 10%. As a baseline, spark ignition was determined to have a lean limit of 1.25. Using hydrogen as the pre-chamber fuel was shown to extend the lean limit the furthest to λ=2.6 with gasoline as the main-chamber fuel and λ=2.5 for the case when LPG was used as the main-chamber fuel. Using LPG as the pre-chamber fuel also showed a significant extension of the lean limit to λ=2.35 for both LPG and gasoline as main chamber fuels. Analysis of the exhaust indicated that when LPG was used as the main-chamber fuel, the NOx emissions were reduced. Furthermore, mass burn rate calculations derived from the pressure traces showed the effect of the different pre-chamber and main chamber fuel combinations.

TJI is a further refinement of the jet ignition concept for direct application to standard spark ignition engines. Attard et al. performed extensive engine studies of TJI [39-45], including a visualization study of TJI in a single cylinder optical engine using natural gas at several air to fuel ratios and engine speeds [46], as well as demonstrating successfully that vaporized gasoline is a viable pre-chamber fuel [44].

The work of previous authors includes testing various pre-chamber fuels and fueling strategies. Using a single fuel source in an engine is preferable, with a liquid gasoline system being the most convenient to implement into existing spark ignition engines that already operate using liquid gasoline as the primary fuel. However, liquid gasoline pre-chamber fueling systems in the literature exhibit diminished performance due to poor mixture preparation caused by limitations of the injector hardware [41].

When using different fuels, the physics that occur during jet ignition may change due to changes in the thermochemistry. For instance, Murase and Hanada studied jet ignition using n-butane mixtures in a rapid compression machine and found that jet ignition triggered autoignition of the mixtures [35]. By analyzing the pressure traces and rate of pressure rise, along with high-speed imaging, the effect of nozzle diameter and ignition timing were investigated. Two different single orifice nozzles were used with diameters of 2.5 mm and 4.0 mm, and the jet behavior was found to change with the orifice geometry and stoichiometric conditions [35].

1.5 Outline of the Dissertation

This dissertation presents several series of experiments on TJI using an RCM presenting pressure trace data and combustion visualization. Chapter 2 gives a detailed overview of the RCM and, and a general testing procedure. However, each series of experiments uses different TJI igniters and optical head geometries. Therefore, in the following chapters, the RCM and TJI configurations are first introduced, and then the experimental results are presented. Chapter 3 presents experimental results on TJI without any auxiliary fuel injection, using propane. Chapter 4 investigates auxiliary fueled TJI with liquid propane used as the auxiliary fuel, and gaseous propane as the main chamber fuel. Chapter 5 presents dual injector TJI experiments performed using methane as the main chamber and pre-chamber fuel. This chapter also investigates the

effect of charge dilution using both nitrogen and exhaust gases. Chapter 6 utilizes an auxiliary fueled TJI system using liquid iso-octane as the auxiliary fuel. This chapter studies the effects of auxiliary fuel injection and ignition distribution due to single orifice and dual orifice nozzle geometry. Finally, Chapter 7 presents a summary of the most important experimental results, and some concluding remarks.

CHAPTER 2: RCM AND EXPERIMENTAL METHODS

2.1 Rapid Compression Machine

The rapid compression machine used for the experiments is shown in Figure 2-1. The RCM operates using three pistons (combustion, hydraulic, and pneumatic) coupled together with two shafts such that any motion from one of the pistons is transferred to the others.

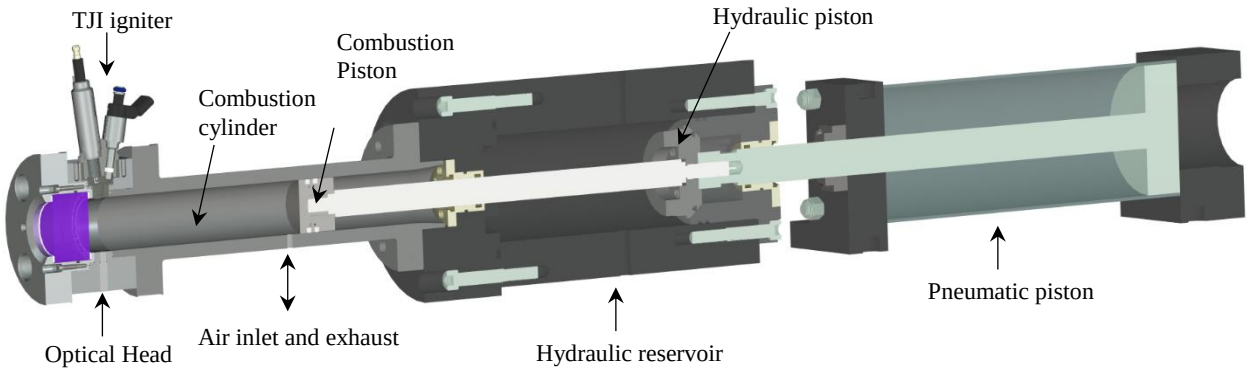

Figure 2-1. RCM illustration showing the location of the TJI igniter with the piston at BDC.

During operation, high-pressure oil in the hydraulic reservoir provides a holding force for the system, while pressurized air acting on the pneumatic piston serves as the driving force. When triggered, a solenoid valve vents the high-pressure oil in the hydraulic reservoir. No longer restrained, the piston system is driven forward until the hydraulic piston reaches the end of the reservoir where it is stopped due to mechanical interference. By introducing shims in the back flange of the hydraulic chamber, the stroke length may be adjusted, which allows the RCM compression ratio to be variable.

The motion of the RCM piston compresses the charge of fuel and air in the combustion cylinder to an elevated temperature and pressure suitable for combustion, which occurs at

constant volume when the piston has reached the end of its stroke. The RCM utilizes a single stroke, and the piston remains at the Top Dead Center (TDC) position until it is returned to the starting position after the test. Figure 2-2 shows a view of the RCM optical head and TJI Igniter when the piston has reached TDC. The TJI Igniter clamps onto the top of the optical head, and depending on the experiments being perfromed, different optical heads and TJI assemblies are used.

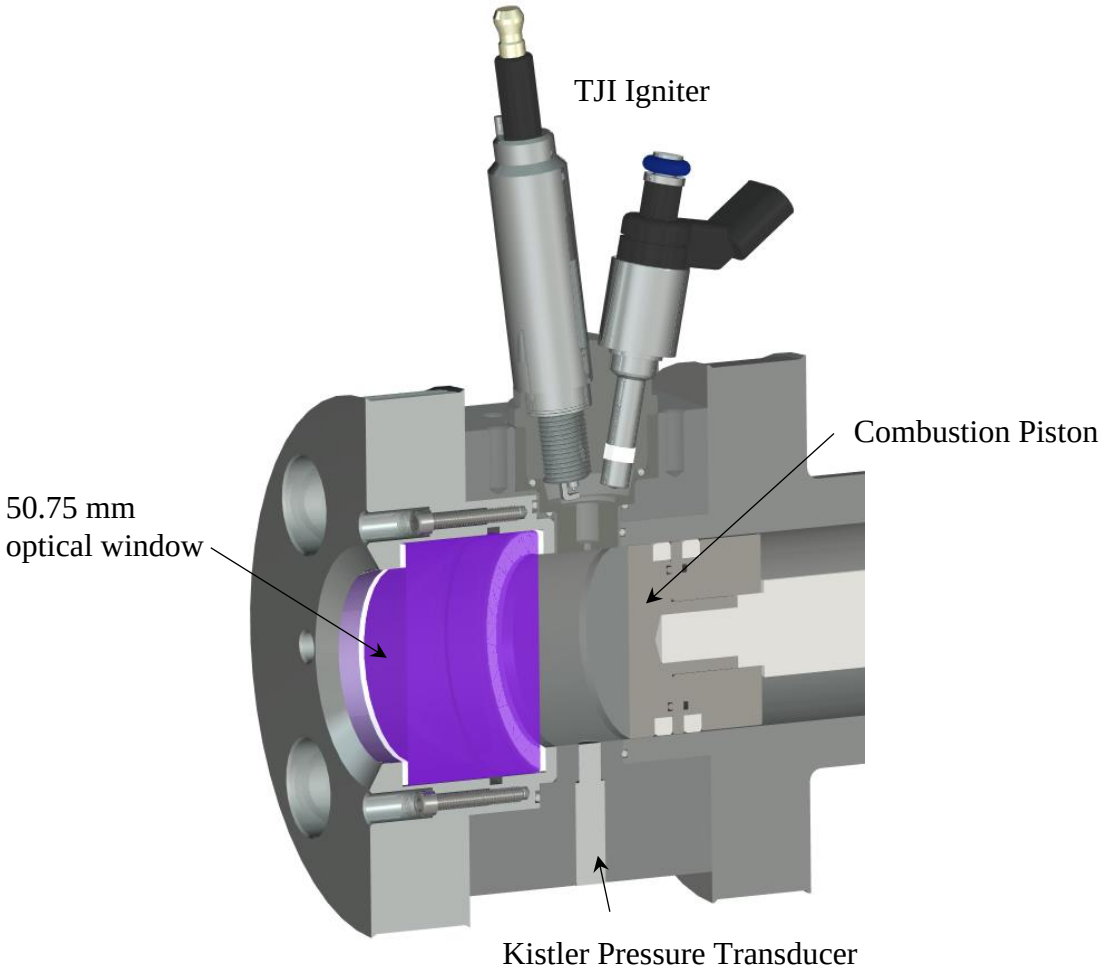

Figure 2-2. View of the RCM optical head showing the location of the TJI igniter at TDC.

The RCM optical head and cylinder are pre-heated using band heaters, which are controlled by a LabVIEW program. In order to maintain a uniform temperature and prevent heat transfer to the surroundings, a high-temperature insulating jacket is used. LabVIEW is also used for signal generation (ignition coil dwell signal, fuel and air injection pulses) and data acquisition (control signals, pre-chamber pressure, and main chamber pressure).

Prior to performing a test the combustion chamber is evacuated of all gasses using a vacuum pump through a small port at the bottom of the combustion cylinder. The fuel is then added to the cylinder using metering valves for gaseous fuels, or via a fuel injector for a liquid fuel. An absolute pressure transducer is installed onto a small manifold that is connected to the inlet port that allows the cylinder pressure to be measured. This provides the partial pressure of the fuel for the chosen stoichiometry, and the partial pressure of air can then be calculated and introduced to the cylinder via the inlet port by using a metering valve connected to a compressed air cylinder.

The entire bore of the RCM cylinder is optically accessible through a 50.75 mm sapphire window. A Photron SA4 high-speed color camera equipped with an objective lens is used to perform direct combustion visualization. Visualization of radical species such as OH^* and CH^* due to chemiluminesence is performed by coupling a Photron SA5 to a LaVision High Speed Intensifier, using a UV-VIS objective lens and bandpass filters. The band pass filters mount onto the end of the UV lens using a short threaded lens tube and retaining ring. For visualizing OH^* chemiluminesence a 307±10 nm band pass filter purchased from Edmund optics was used, while a 430 nm ± 10 nm band pass filter was used to image CH^* radical species. Further details regarding the experimental setup can be found in [47, 48].

2.2 Testing Protocol

In general, the following procedure was used for performing the experiments using the RCM.

1. Pre-heat the combustion chamber walls to the desired temperature, usually 80 ℃ to 110℃ to simulate the temperature of an engine cylinder block.
2. Using the LabVIEW control system, set the values for the relative spark timing and auxiliary injection timing.
3. Vacuum out the combustion chamber and pre-chamber completely of residual gasses.
4. Add fuel, followed by air, then other diluent gasses depending on the test to obtain the desired air/fuel ratio and dilution percentage.
5. Pressurize the hydraulic chamber by manually pumping the reservoir with hydraulic fluid to a pressure of 1000 psi. This acts as the holding pressure until the system is ready to fire, and prevents the pistons from moving.
6. Using compressed air that is stored in a pressure vessel, pressurize the pneumatic piston to a pressure of 140 psi. This acts as the driving force for the pistons.
7. Setup the high speed camera to begin image acquisition when it is sent a trigger signal.
8. Fire the RCM using the LabVIEW control system. This sends a control signal to a solenoid valve that is connected to the hydraulic reservoir, causing the valve to open and vent the high pressure hydraulic fluid. No longer restrained, the force from the pneumatic piston drives the piston rod and combustion cylinder piston forward, compressing the charge of fuel and air to an elevated temperature and pressure. The spark in the TJI pre-chamber is initiated, and if the test is successful, combustion occurs.
9. Manually bring the piston back to the starting position, begin vacuuming out the gasses from the combustion chamber, save the experimental data, and prepare for the next t

CHAPTER 3: TJI WITHOUT AUXILIARY INJECTION

3.1 Introduction and Motivation

The purpose of this series of experiments is to gain a better understanding of the TJI process by studying how the orifice diameter in a turbulent jet igniter affects the combustion performance of a TJI system. To accomplish this, a simple TJI system without any auxiliary injection was tested with several different orifice nozzle diameters and configurations in an optically accessible rapid compression machine. Quantitative pressure data was gathered in order to compare the relative combustion performance of each orifice diameter. In order to help interpret the pressure data, combustion visualization of the transient ignition process was also obtained by using a high-speed color camera. A second high speed camera coupled to an image intensifier was configured to capture the chemiluminesence of OH* and CH* radicals. A novel aspect of these experiments are the color optical images and radical imaging, which allow for additional observations about the flame structure and ignition zones of the jet ignition process. The experiments presented in this chapter also test a greater range of nozzle diameters and expand on efforts and results of other authors as presented in the literature.

3.2 Experimental Set-up and TJI igniter details

The TJI system tested consists of a steel adapter body, which is mounted to the RCM optical head and seals by an O-ring seal. A nozzle with one or more small orifices threads into the bottom and an NKG CR6E spark plug threads into the top of the adapter body. The pre-chamber volume is 1 cm^3, which is approximately 2% of the clearance volume of the RCM. A standard automotive ignition coil and a transistor ignition circuit is used with the spark plug to initiate combustion in the pre-chamber. Table 3-1 gives an overview of the RCM configuration and TJI igniter details. A detailed view of the igniter installed onto the combustion chamber is

shown in Figure 3-1. Cross sectional views of the different nozzle configurations that were tested, together with their respective diameters and total cross sectional areas are also shown in Figure 3-1. The thickness of each nozzle was 3 mm. Four single orifice nozzles with diameters of 1.0 mm, 1.5 mm, 2.0 mm, and 3.0 mm were tested together with four multiple orifice nozzles with different configurations. In order to study the influence of orifice number on the combustion process while keeping the mass flow rate similar, two and three orifice nozzles with nominally equivalent cross sectional areas were tested. Another interesting scenario that was tested was using an asymmetrical dual orifice nozzle with diameters of 1.25 mm and 2.0 mm. A six-orifice nozzle was also fabricated and tested with each orifice diameter being 1.25 mm.

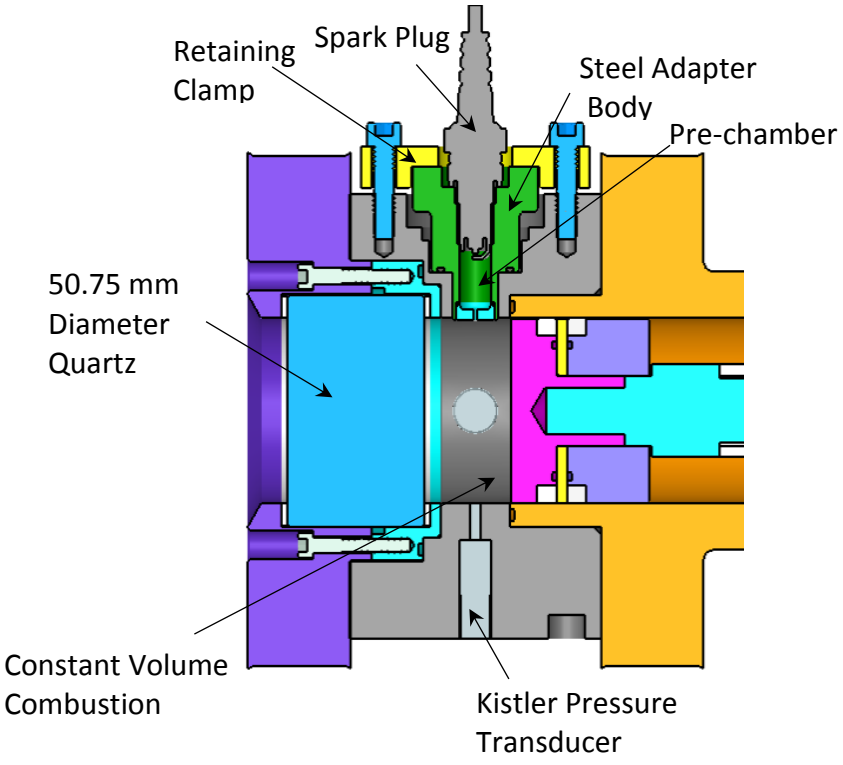

Figure 3-1. RCM optical head, showing TJI igniter location

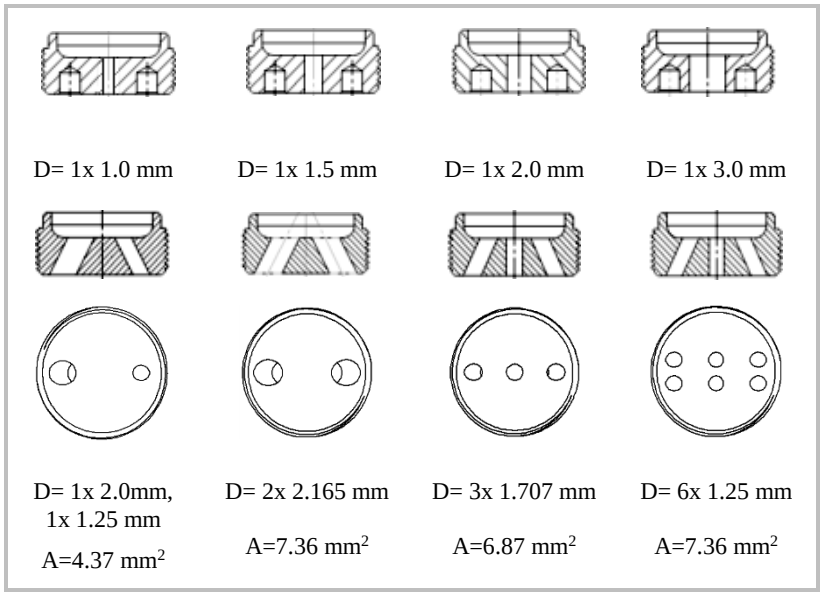

Figure 3-2. Nozzle geometries used in the experiments

Table 3-1. Overview of experimental set-up

Cylinder Wall Temperature	80° C
Compression Ratio	8.51
Cylinder Capacity	459.33 cm^3
Clearance Volume	53.91 cm^3
Piston Stroke Length	20.32 cm
Cylinder Bore	5.05 cm
Fuel used	Instrument grade Propane (99.5% purity)
TJI pre-chamber volume	1 cm^3
TJI Nozzle Orifice Length	3 mm
Electrical Ignition System	Conventional inductive discharge
Spark Plug	NKG CR6E
Objective Lens	Nikon 100 mm f/2.8 (Direct Visualization)

3.3 Experimental Pressure Data

The main-chamber pressure traces of TJI initiated combustion were obtained for each nozzle configuration shown in Figure 3**.** Experiments were also run for standard spark ignition without a pre-chamber in order to obtain a performance baseline. For each nozzle, λ (air to fuel ratio / stoichiometric air to fuel ratio) was varied from stoichiometric to the lean limit, which was defined as when no increase in pressure occurred after compression in the RCM. Each test was repeated three times to demonstrate repeatability. The nozzle orifice area governs the mass that can flow through the orifice into the pre-chamber before the ignition event, as well as influencing the jet velocity and distribution of ignition sites when initiating main chamber combustion.

Two important performance parameters that can be derived from the pressure trace are the 0-10% and 10-90% burn duration of the pressure rise due to combustion. Figure 3-2. shows a typical pressure trace obtained in the RCM with the TJI process, with annotations included to demonstrate how the performance parameters are calculated.

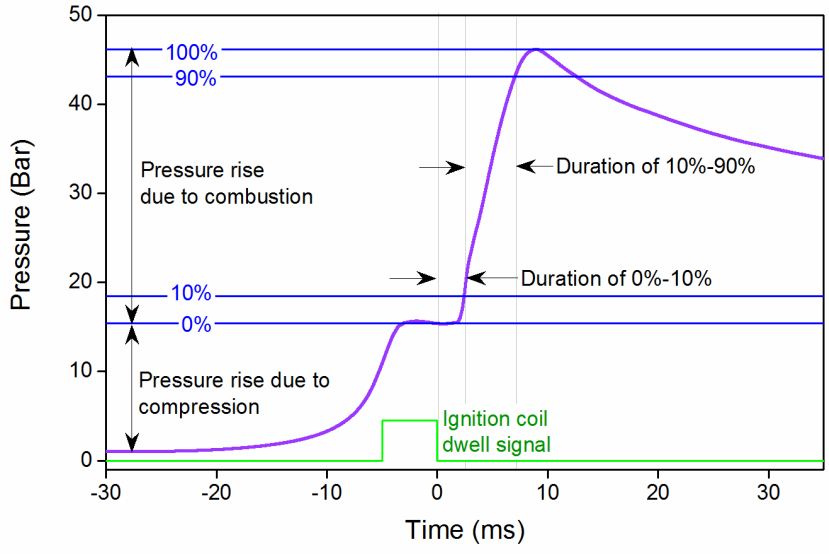

Figure 3-3. Typical pressure trace showing the definition of the burn durations.

As shown in the diagram, the first increase in pressure is due to the piston motion compressing the charge of fuel and air to an elevated temperature and pressure. When the piston reaches the end of its stroke length, or Top Dead Center (TDC), it remains in that position for the duration of the test resulting in a constant volume combustion chamber. A control signal is sent to the ignition triggering circuit 6 ms after TDC, which triggers the spark plug and initiates combustion in the pre-chamber and subsequently in the main chamber as the hot combustion products of the turbulent jet discharge through the nozzle orifice(s). This produces a pressure rise strictly due to combustion, since the piston is stationary and the combustion chamber is at a constant volume. The pressure reaches a maximum, and then falls due to the heat transfer to the surroundings. If the pressure is scaled such that at TDC when the spark plug is fired, the pressure is taken to be 0% of the pressure rise due to combustion, and the maximum pressure is taken to be 100 %, then the time interval, or burn duration for the pressure to increase from 0% to 10% of the pressure rise can be used to determine how quickly the flame is initiated. Similarly, the time interval that it takes for the pressure to increase from 10% to 90% of the maximum can be defined as the 10-90% burn duration and gives an overall indicator of the combustion progress once it has been initiated [49, 50].

The calculated 0-10% and 10-90% burn durations averaged over the three experimental runs are shown respectively in Figures 3-4 a and 3-4 b. The data is plotted using a binary logarithmic scale for the ordinate. Logarithmic scales are nonlinear scales that are useful for representing the data when there is a large range of quantities. While a base of ten is useful when the data covers several orders of magnitude, a binary logarithm with base two is more suitable when the data has a smaller range. Near stoichiometric conditions (λ=1), the shortest 0-10% burn durations were given by the 1.0 mm, 1.5 mm, and 2.0 mm diameter single orifice nozzles, which had

comparable performance. The 1.0 mm single orifice nozzle that was tested failed to ignite the mixture reliably in the main chamber for $\lambda > 1.25$. In this case the fast discharge velocity underlies high shear stresses between the jet and the unburned mixture, causing excessive cooling of the jet [6]. The multiple orifice nozzles had slower 0-10% burn duration, but were still faster at initiating combustion than the spark plug baseline tests. For $\lambda > 1.25$, the combustion performance of the D=3.0 mm single orifice approached the performance of the SI baseline case. These results indicate that for combustion initiation, a single small orifice diameter is more advantageous than the multiple orifice or larger office nozzle configurations.

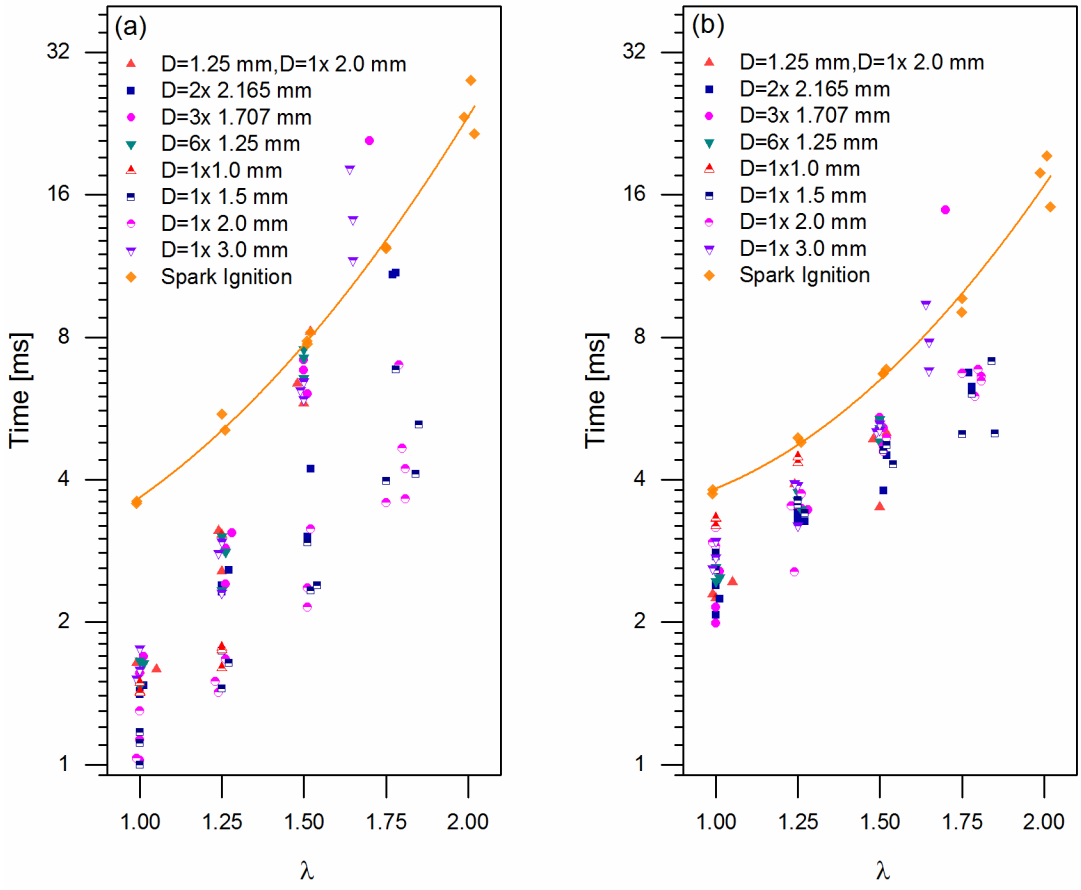

Figure 3-4. (a) Variation in 0%-10% burn durations for all nozzle geometries. (b) Variation in 10%-90% burn durations for all nozzle geometries.

The 10-90% burn duration gives an indication of the overall flame propagation speed and is shown in Figure 3-4b**.** For this performance parameter, at near stoichiometric conditions, the burn durations were shortest for the multiple orifice nozzles while the single orifice nozzles had an intermediate performance when compared to the spark plug baseline. As λ was incrementally increased, the difference in the 10-90% burn durations for each nozzle configuration was increasingly noticeable. The D=2x2.165 nozzle showed the best performance up until λ ≥1.5, at which point the two smallest diameter single orifice nozzles had slightly faster burn durations. It is important to note that not all of the nozzles were able to initiate combustion in the main chamber of the RCM as the initial charge became increasingly lean. The lean limits obtained for each configuration are shown graphically in Figure 3-5.

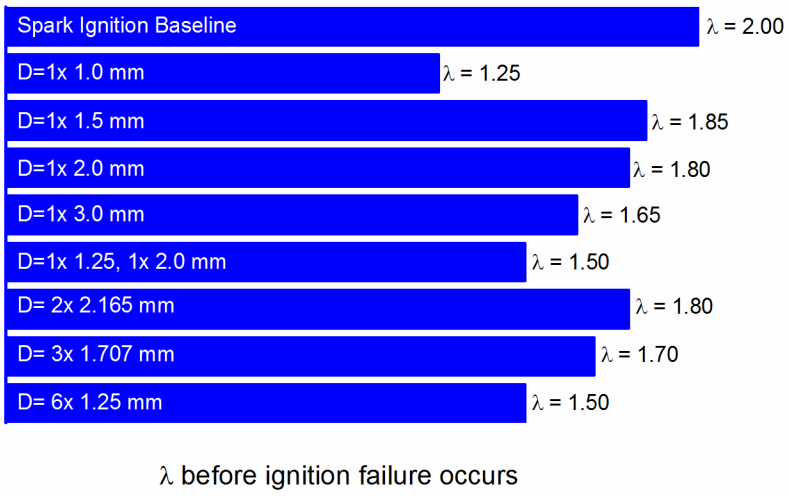

Figure 3-5. Comparison of experimental lean limit for the different nozzle geometries.

It is clear that for the experiments presented, the TJI system was not able to extend the lean limit compared to the SI baseline tests for any of the nozzle configurations. This is due to the additional heat transfer losses of the jet of hot combustion products to the orifice wall, as well as additional cooling of the jet as it mixes with the cool unburned mixture in the main chamber [6]. This result is different to auxiliary fueled pre-chamber TJI systems, which can extend the lean limit of combustion relative to SI , as their operating principle is fundamentally different due to the additional pre-chamber fuel [5, 43]. This affects the ignition characteristics in multiple ways as (1) the fuel rich pre-chamber mixture in the vicinity of the spark plug electrode is easily ignited, (2) the jet temperature is hotter, and (3) the transport of active radicals and unburned fuel from the pre-chamber participate in the combustion process.

Figure 3-6 shows a comparison of the pressure traces for a direct comparison at stoichiometric conditions between spark ignition and jet ignition a 2 m single orifice nozzle. The spark timing was set to occur at the same time after TDC for both cases. This figure provides an illustration of the enhancement in the burning rate when using TJI compared to SI.

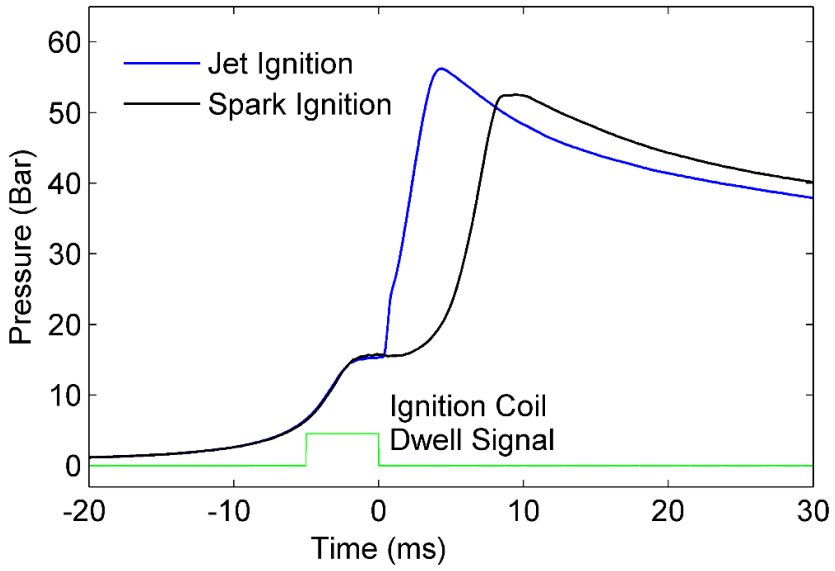

Figure 3-6. Comparison between SI and TJI at λ=1

3.4 Combustion Visualization and Analysis

The contrast and brightness of the color images were enhanced using Image J, an image processing software available for download through the National Institutes of Health [51]. A gray circular outline was superimposed onto the images to display the boundary of the optical window and to give a sense of scale since the boundary is only illuminated by reflected light and not clearly visible in all of the frames that were captured. Figure 3-7 shows the combustion from the direct spark ignition for a stoichiometric mixture, With SI, there is a highly localized ignition source with ignition occurring at a point resulting in a relatively slow deflagration (note differences in time steps with SI and TJI). With TJI, distributed ignition occurs throughout the jet volume and the burning rate is very rapid. The initial jet velocity is important because it determines the amount of turbulence the jet generates and its ability to entrain unburned mixture.

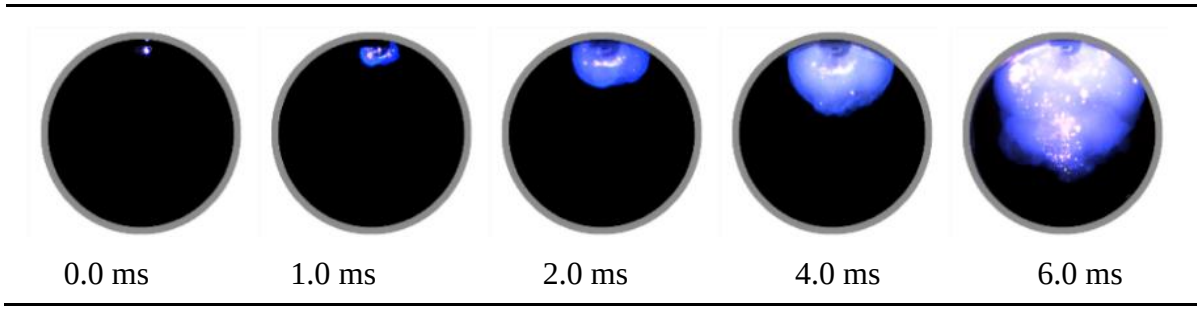

Figure 3-7. Combustion visualization of spark ignition.

However, if the jet velocity is too fast, it may be disadvantageous for ignition to occur. This is evident by considering the optical images from the single orifice TJI case, D=1.0 mm as shown in figure 3-7. In figure 3-7, the initial jet discharge is fast and ignition occurs near the jet tip. The high jet velocity underlies high strain rates, causing excessive cooling in the mixing regions affected by the shear stresses.

Figure 3-8. Combustion Visualization for TJI, single orifice nozzle D=1.0 mm.

In this case, local quenching occurs and makes ignition less likely to occur on the lateral sides of the jet, with ignition of the entrained main chamber charge occurring in the volume of the jet tip near the center of the combustion chamber. Figure 3-8 shows an enhanced image of the jet in figure 3-7 at 1.7 ms. From this enhanced image it can be seen that the core of the discharging jet is still visible, showing that quenching has not completely occurred even though it appears to be in figure 3-7 due to the contrast in brightness from ignition at the jet tip.

Figure 3-9. Enhanced image at 1.7 ms showing that there is not complete quenching of the jet as it discharges.

For the other nozzle configuration tested, Figure 3-9 and Figure 3-10 show TJI initiating combustion in the main chamber of the RCM for λ=1.0 and λ=1.25, respectively. The emission of light is proportional to the temperature and stoichiometric conditions. It can be seen that at

λ=1.0, the natural luminosity of the jet is brighter, and the discharge velocity and flame propagation is faster than the image sequences that depict the combustion process for λ=1.25.

The image sequences obtained can be used to help interpret the 0-10% and 10-90% burn duration data. When examining the TJI process due to the single orifice nozzles in Figure 3-3 and Figure 3-4, it can clearly be seen that the D=1.5 mm nozzle, which has the smallest diameter and cross sectional area of the nozzles shown, discharges into the combustion chamber the most rapidly with the furthest initial jet penetration and quickly impinges onto the bottom of the combustion chamber wall. This nozzle produced the fastest 0-10% burn durations near stoichiometric conditions. The D=2.0 mm orifice nozzle is shown to produce a jet that has a slightly slower jet velocity and slightly less jet penetration. The combustion occurs mainly in the middle of the chamber, and there is less jet/wall interaction as ignition occurs. This interaction with the wall can explain why at λ≈1.75 the 2.0 mm diameter orifice has a faster 0-10% burn duration than the 1.5 mm orifice, which initially seems counterintuitive since the smaller orifice produces a faster jet velocity. In this case the heat transfer to the walls from the hot jet is detrimental to the combustion initiation process.

The D=1x3.0 mm, D=2x2.165 mm, D=3x1.707 mm, and the D=6x1.25 mm nozzles were designed to have similar total orifice cross-sectional area in order to examine the effect of orifice diameter and number. The small differences in cross sectional area are due to choosing the closest drill size to match the desired diameter. It can be seen from Figure3-7 and Figure 3-8 that the D=2x2.165 mm dual orifice nozzle is better at initiating combustion and also has a faster overall combustion progression than the D=1x3.0 mm, D=3x1.707 mm, and D=6x1.25 mm configurations. In the case of the 3 and 6 orifice nozzles, the jets have additional heat transfer and frictional losses as they pass through the orifices relative to the two-orifice nozzle.

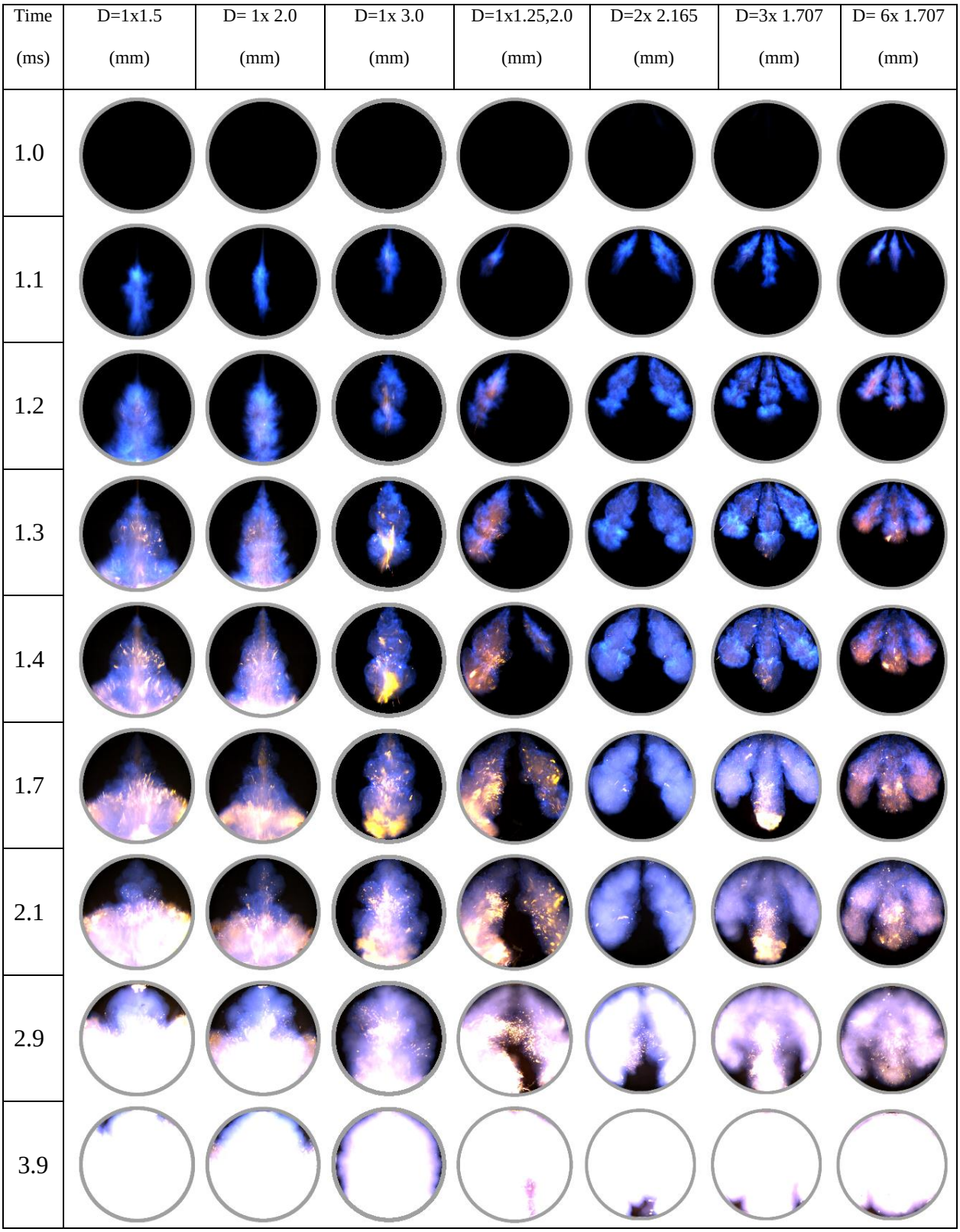

Figure 3-10. Direct Combustion Visualization of TJI for λ=1.0 (stoichiometric).

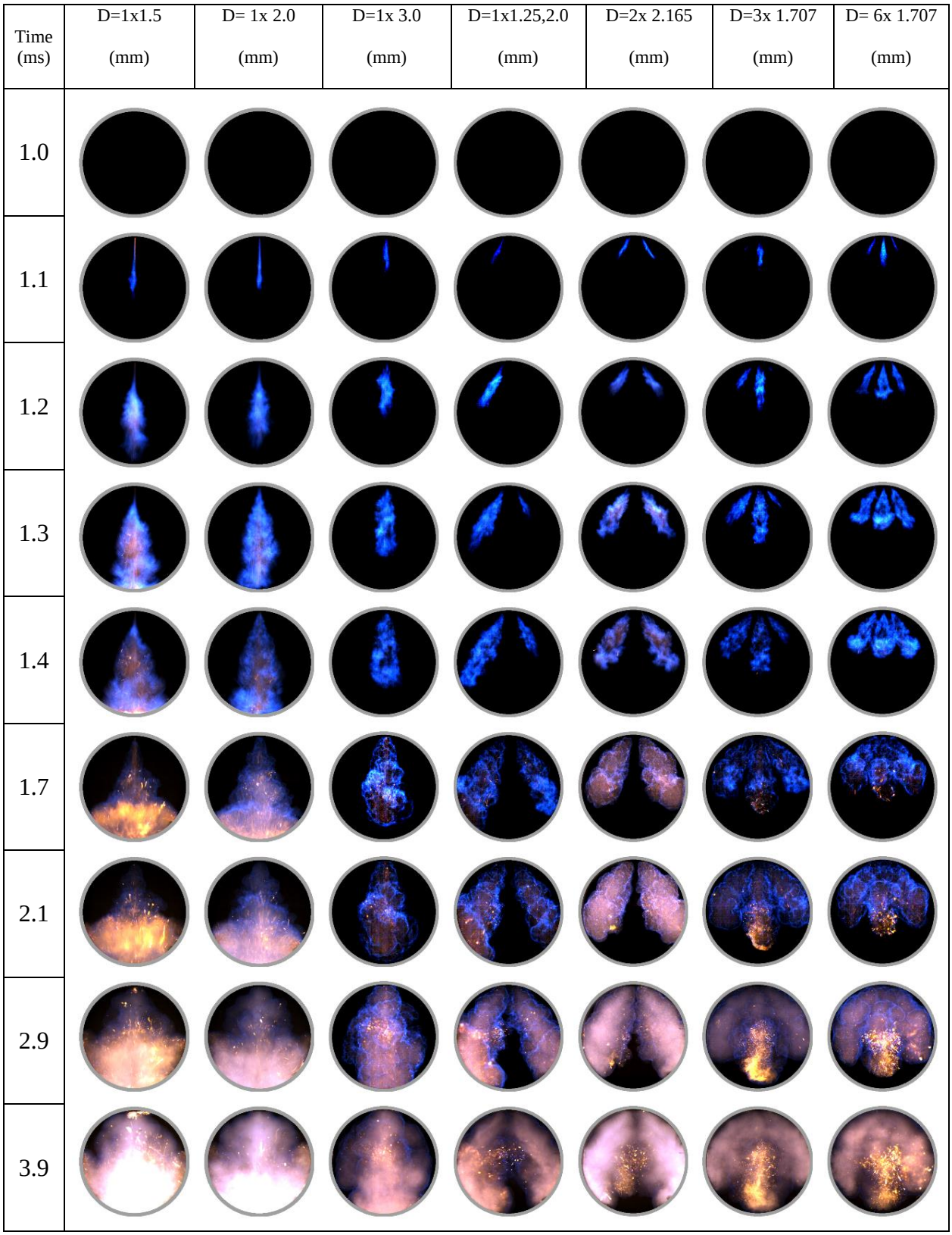

Figure 3-11. Direct Combustion Visualization of TJI for λ=1.25 (lean).

On the other hand, the dual-orifice nozzle has better combustion performance than the D=1x3.0 mm diameter due to the jets being more spatially distributed throughout the entire combustion chamber which resulted in less wall interaction and enabled combustion to occur volumetrically throughout the jet structure.

It is also interesting to note that for λ=1, the D=2x2.165 mm orifice produces turbulent jet structures that appear to ignite the most volumetrically. The images from the other nozzles have zones where intense combustion appears to occur before the rest of the jet structure. The most obvious example of this is with the D=3x1.707 mm nozzle as seen at 1.7 ms for λ=1 and 2.2 ms for λ=1.25. A region of high luminosity saturates the camera sensor at the jet tip in both cases before volumetric combustion occurs throughout the rest of the jet. This is likely due to the motion of the three jet structures compressing the unburned mixture, and increasing the temperature and pressure in the vicinity of the middle jet tip, causing the combustion to progress more rapidly in this region.

The jets that come into contact with the RCM cylinder walls also show this inhomogeneous combustion progression throughout the jet structure. As Oppenheim et al. [31] mentioned in their research, the interaction of the jet with the wall is detrimental due to the heat transfer losses to the wall boundary as well as creating a stagnation zone where the jet can no longer entrain unburned mixture. From Figure 3-7 it can be seen that the D=1x1.5mm, D=1x 2.0mm, and D=1x3.0 mm single orifice nozzles and the D=1x1.25, 2.0 mm asymmetrical nozzle, impinge onto the combustion chamber wall. Interestingly, despite the heat losses present, combustion throughout the jet seems to occur at the wall boundary, and then progresses upward consuming the remaining volume of the jet.

Short lived radical species play an important role in combustion initiation with turbulent jet ignition [5, 34]. In the literature, these radicals have been found to be correlated to certain features of the combustion process. In particular, the OH* radical has been shown to be an indicator of the heat release rate in propane flames [52-54], while the CH* Radical is an indicator of the flame front position since it is produced spatially close to the first sharp rise in temperature within the reaction zone [53, 55, 56]. Thus to further understand the TJI process it would be helpful to visualize the relative concentration and distribution of these OH* and CH* radicals. This can be accomplished by examining the chemiluminesence due to these radical species, which is the natural emission of light due to chemical reactions that occur at a characteristic wavelength of 307 nm for OH*and 430 nm for CH*, which allows for the imaging of the radicals by selectively filtering out all other wavelengths of light. The resulting images should be interpreted as the light output from a single wavelength where the intensity of the light varies spatially in proportion to the amount of radical species present.

To aid in the visualization a false-color map is applied to both sets of images to easily see the regions of high radical concentration, as well as to show a relative scale. Figure 3-11 shows the false-color visualization of the OH* radical distribution for the D=1x 2.0 mm orifice and the D=2x 1.25 mm orifice case for λ=1.0 and λ=1.25. Similarly, Figure 3-11 provides a comparison of the CH* radical species for the same two nozzles and λ values. It should be noted that these images represent a line of sight measurement and the resulting two-dimensional image is an integrated result from the chemiluminesence throughout the volume of the entire jet.

The OH^* Radicals are considered to be an indicator of the high temperature reactions that are occurring within the flame [54]. It can be seen that for the D=1x 2.0mm, λ=1 case, there appears to have a high distribution of OH* radicals across the entire jet whereas at λ=1.25 there

are more distinguishable regions of radical concentrations near the jet tip, with a vortex structure at the jet tip showing a high radical concentration. This implies that there are more of the high-

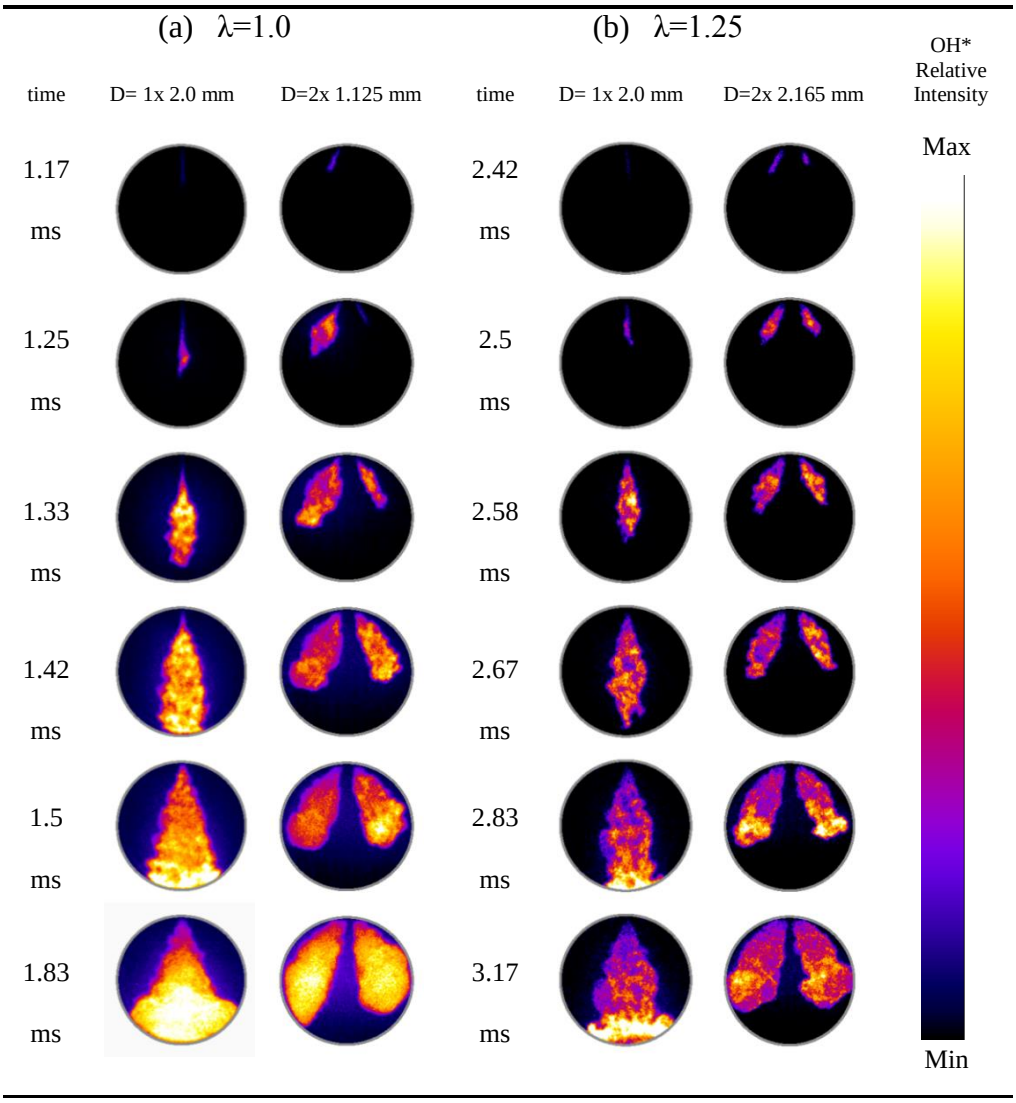

Figure 3-12. Visualization of OH*Chemiluminesence during TJI.

temperature chemical reactions occurring in the jet tip, likely due to increased mixing [6, 57, 58]. The D=2x2.165 mm orifice also shows similar behavior with the radical distribution being fairly well distributed throughout the jet structure, with high concentrations of OH* near the jet tip. It should be noted that for the case of λ=1.0, the D=2x2.165 mm orifice produces a jet that first discharges out of the left orifice while the jet discharging from the right orifice discharges later.

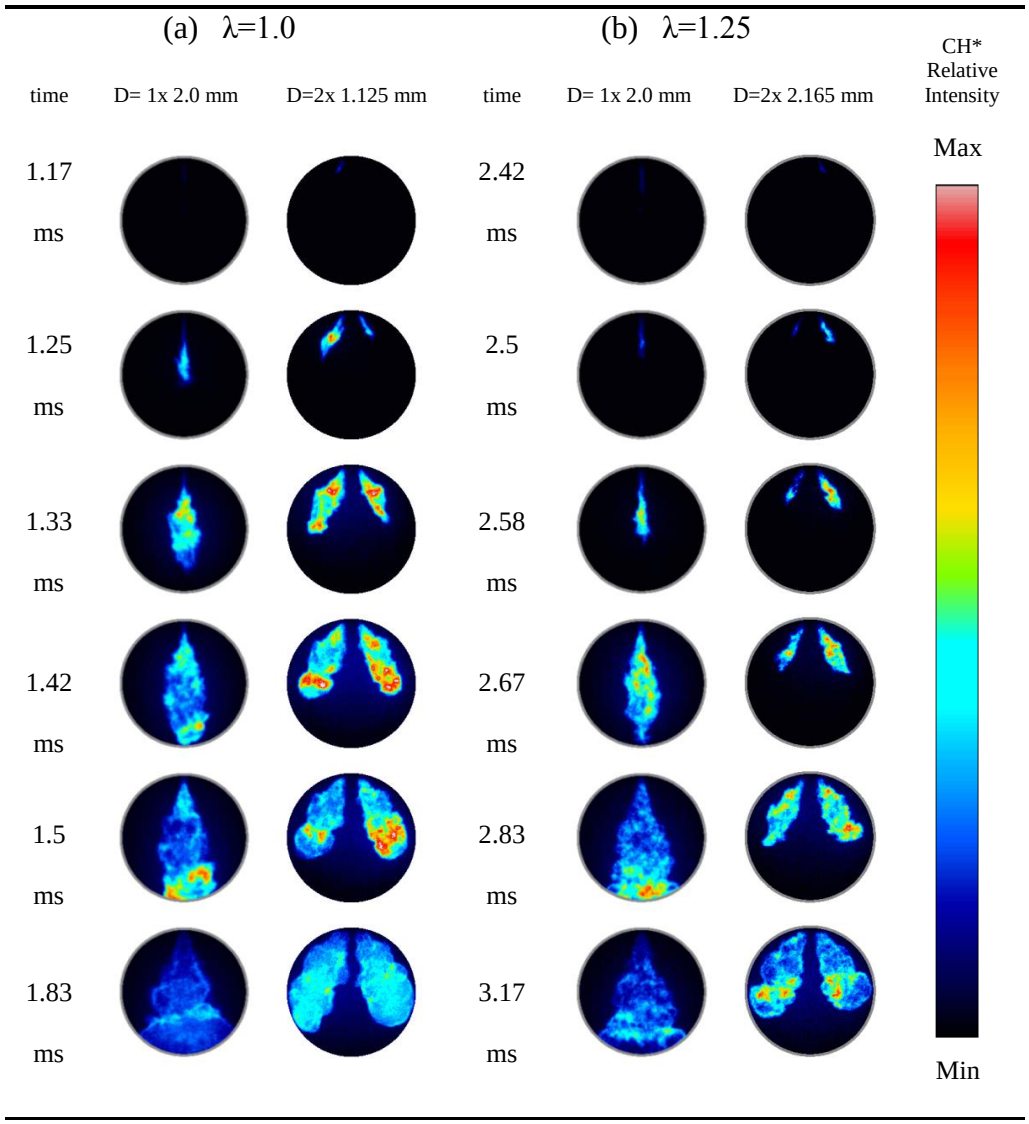

Figure 3-13. Visualization of CH* Chemiluminesence due to TJI.

This is not characteristic of this orifice geometry. In fact, the nozzle orifice geometry is symmetrical and this result is simply due to the stochastic nature of ignition, where the shape and direction of the initial spark kernel formation within the pre-chamber plays a role in which orifice discharges first, which can be seen by comparing the images presented for this nozzle at both λ=1.0, and λ=1.25. When comparing Figure 3-10 and Figure 3-11, it can be seen that the OH* and CH* radicals overlap spatially. The CH* chemiluminesence gives an indicator of the flame boundary, with high concentration occurring throughout the middle of the jet and with the

highest relative intensity not just constrained to the vicinity of the jet tip. CH* is a short-lived species, and it is observed that the relative concentration of this radical species decreases in time.

3.5 Chapter Summary

In order to better understand the effect that nozzle diameter had on the TJI ignition process, several different orifice nozzle diameters and configurations were tested in the RCM. This effort expanded on TJI experiments documented in the literature by testing a broader range of orifice nozzles. Quantitative performance parameters derived from the combustion trace that characterized different aspects of the combustion process were also introduced. By comparing the 0-10% and 10-90% burn durations the ignition behavior was examined by considering how well a mixture could be ignited as well as the speed of the overall combustion progression. Combustion visualization was performed using a high speed color camera which displayed the direct transient jet development. Image processing techniques were then applied to the images, which showed that the 0-10% burn duration performance parameter correlated with the initial flame areas of the discharging jets.

By analyzing the optical images, the relationship of the interaction of the wall boundary and combustion in the jet structure was further studied. It was not obvious from previous imaging studies that combustion in the jet actually started to progress faster in certain spatial zones of the jet structure. In general, The 0-10% and 10-90% burn duration results indicate that if ignition can be initiated reliably and without difficulty in both the pre-chamber and main chamber, such as in a stoichiometric mixture, then a nozzle that will produce jets that are volumetrically distributed throughout the combustion chamber will be more advantageous and will consume the main chamber charge more rapidly. However as the mixture becomes leaner, a faster and more vigorous jet with greater initial jet penetration is required to initiate combustion.

Visualization of the OH* radical species allowed us to obtain insight into where the exothermic chemical reactions were occurring, with a high radical intensity occurring near the jet tip. The CH* visualization was useful as an alternative method of showing the flame boundary, which is important to determine the true structure of the jets. It was found that the OH* and CH* radicals overlap spatially throughout the jet structure.

CHAPTER 4: TJI WITH AUXILIARY INJECTION OF LIQUID PROPANE

4.1 Introduction and Motivation

The purpose of this chapter is to study some of the fundamental aspects of turbulent jet ignition when using auxiliary fuel injection, and build upon the results obtained in chapter 4 for no auxiliary fuel injection. This is accomplished by performing a series of experiments in an optically accessible rapid compression machine (RCM) using gaseous propane as the main chamber fuel and liquid propane as the auxiliary fuel. The experimental lean limit without any auxiliary injection is first presented, and then when using auxiliary injection the lean limit extension is demonstrated. Combustion characterization is then performed by analyzing the pressure traces for each test. Using a pre-chamber pressure sensor, the flow interaction between the main-chamber and pre-chamber is explored for different conditions. Combustion visualization using a high-speed color camera gives additional insight into the turbulent jet ignition process, and allows for comparison between different testing configurations and further interpretation of pressure trace features.

4.2 Experimental Set-up

4.1.1 TJI Geometry Details and RCM configuration

Figure 4-1 gives a view of the TJI igniter assembly installed onto the RCM optical head with the components labeled. The pre-chamber adapter body is a two-piece design that clamps together. The top piece of the adapter body is the mounting location for the fuel injector and spark plug, while the bottom piece contains the pre-chamber cavity and an interchangeable nozzle that threads into the bottom. For the experiments performed in this paper, a single orifice nozzle with a diameter of 1.5 mm was used.

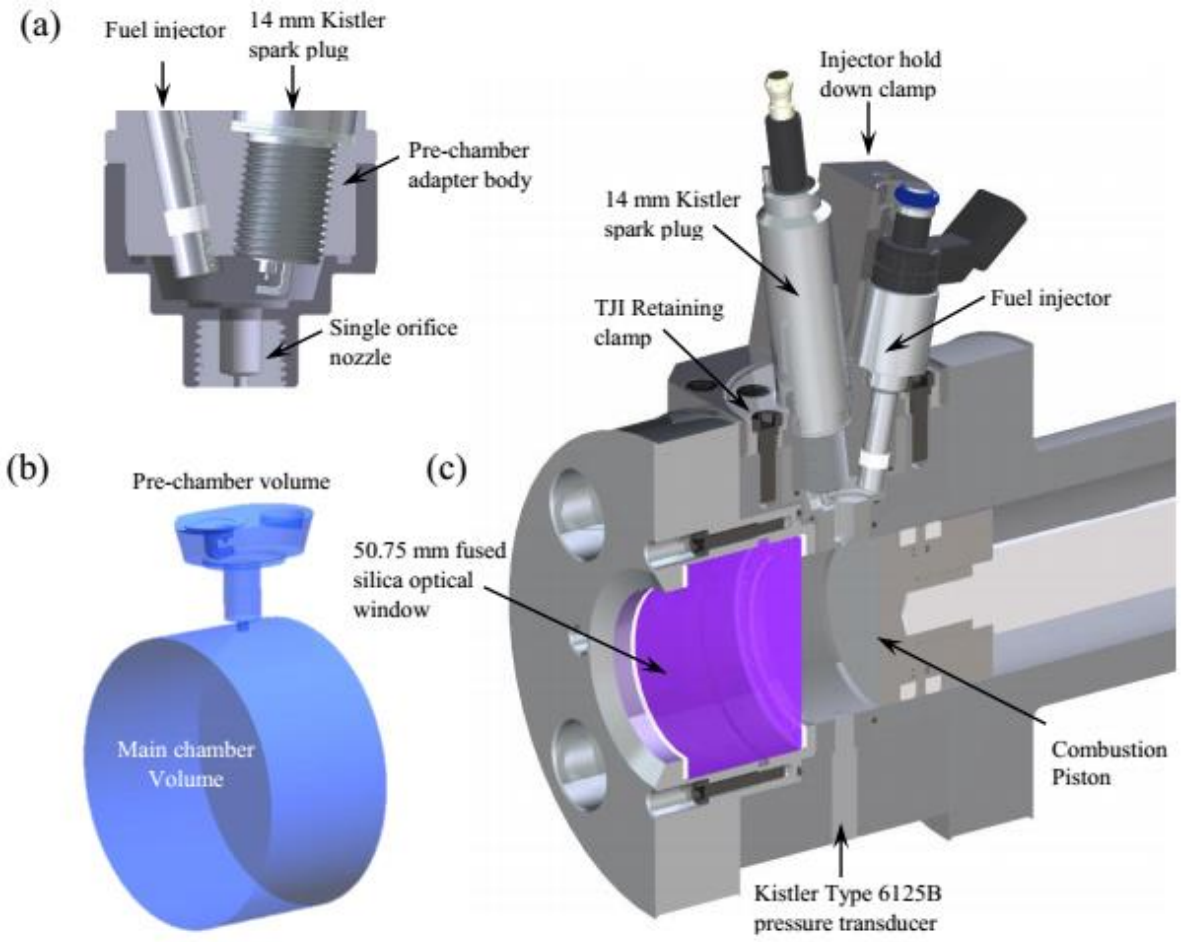

Figure 4-1. (a) Pre-chamber cavity (b) Pre-chamber and main chamber volumes (c) RCM and TJI set-up for auxiliary fuel experiments.

The fuel injector clamps onto the pre-chamber using a mounting block. The spark plug with the integrated pressure sensor threads onto the pre-chamber adapter body and seals using a crush washer. The pre-chamber volume has an elliptical shape near where the spark plug, pressure sensor, and fuel injector are located, while the geometry is cylindrical in the portion of the pre-chamber near where the nozzle is installed. The details of the RCM and TJI set-up are summarized in Table 4-1.

Table 4-1. RCM and TJI configuration

Cylinder Wall Temperature	80° C
Compression Ratio used	8.5
Cylinder Capacity	459.33 cm^3
Clearance Volume	53.91 cm^3
Piston Stroke Length	203.2 mm
Cylinder Bore	50.5 mm
Compressed pressures at TDC	1500 kPa
Main chamber fuel used	Gaseous propane (99.5% Purity)
Auxiliary fuel	Liquid propane
Auxiliary fuel injector	Audi direct injector OEM Pin: 079906036C
TJI pre-chamber volume	2.35 cm^3
Nozzle Orifice Diameters	D= 1x 3.0 mm
Orifice length	3.0 mm
Electrical Ignition System	Conventional inductive discharge
Power Supply Voltage	13.5 V
Ignition Coil Dwell Time	5 ms
Spark Plug and Pre-Chamber Pressure Sensor	Kistler Type: 6117BFD17
Main chamber pressure sensor	Kistler Type: 6125C
High Speed Camera	Photron SA4
Objective lens	Nikon 50 mm f/1.2

4.1.2 Auxiliary Fuel Injection Set-up

Liquid propane is used for the auxiliary fuel. Propane is naturally in the gaseous phase at room temperature, and has a relatively low saturation pressure compared to other fuels (951 kPa at 298K). Thus, in order to change the state from a gas to a liquid, an expandable bladder system was used to pressurize the gaseous propane past the saturation pressure to 965 kPa. To determine the injected mass, a calibration of the fuel injector was performed with the cylinder heated up to

the operating condition of 80˚C by pulsing the injector into the RCM at atmospheric pressure and using a pressure sensor to measure the incremental pressure increase due to the injection event. Pulse widths from 2 ms to 15 ms were used, and three data points at each pulse width were obtained in order to show linearity and repeatability. Since the liquid propane will evaporate as it is injected into the RCM cylinder, the injected mass can then be calculated from the ideal gas law. The calibration curve for the fuel injector is shown in Figure 4-3.

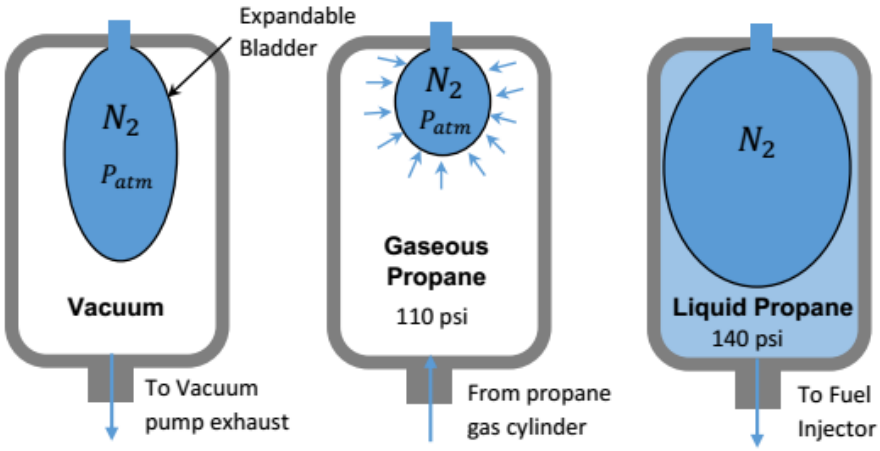

Figure 4-2. Illustration of auxiliary fuel injection set-up.

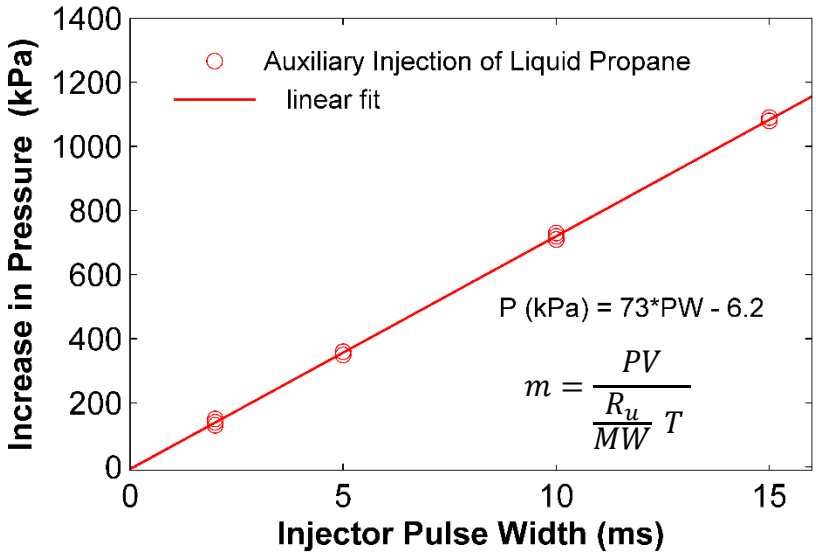

Figure 4-3. Auxiliary fuel injection calibration.

4.2 Experimental Results

4.2.1 Demonstration of Lean Limit Extension

Experiments were first performed to determine the lean limit and combustion performance of the TJI system without using any auxiliary fuel injection. Figure 4-4 shows the experimental pressure traces obtained, with combustion failing to occur after λ=2.0.

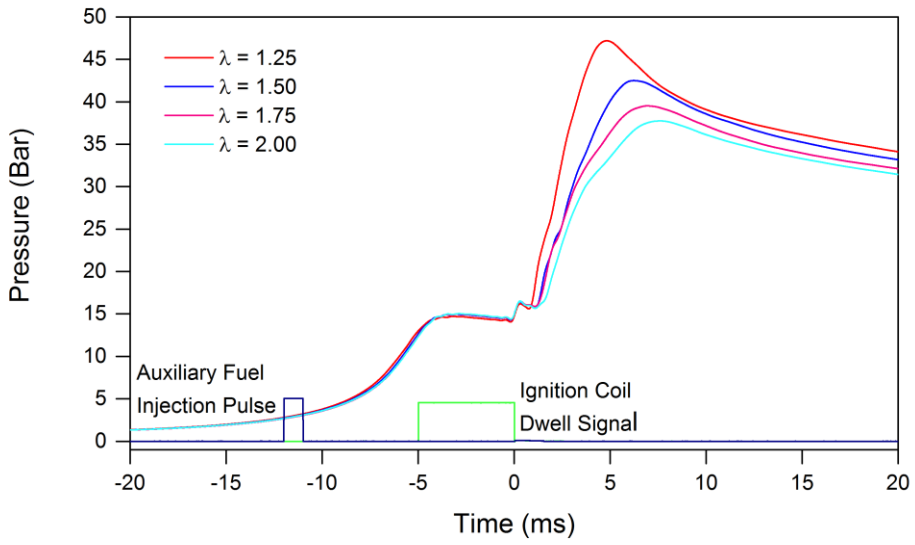

Figure 4-4. Experimental pressure traces for TJI without auxiliary injection

Next, in an attempt to extend the lean limit and improve combustion performance, TJI was operated in an auxiliary fueled pre-chamber mode, with a 1 ms auxiliary injection fuel pulse being used. Longer pulses resulted in failed combustion attempts due to too much fuel being injected, and the pre-chamber being richer than the upper flammability limit of combustion. The pressure traces obtained from the main cylinder in this case are given in annotations describing λ in the figure are global values, and include the injected fuel mass.

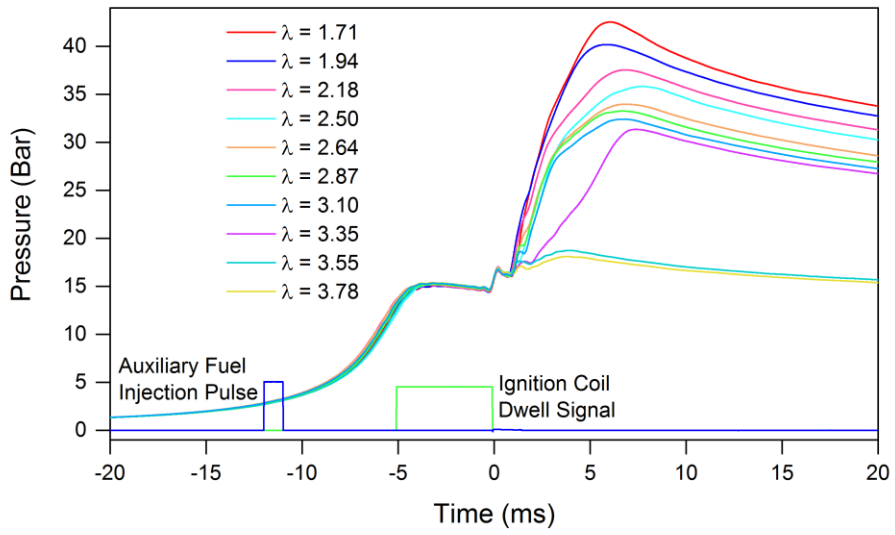

Figure 4-5. Experimental pressure traces for TJI with auxiliary injection of liquid propane, with an experimental lean limit determined to be λ=3.10.

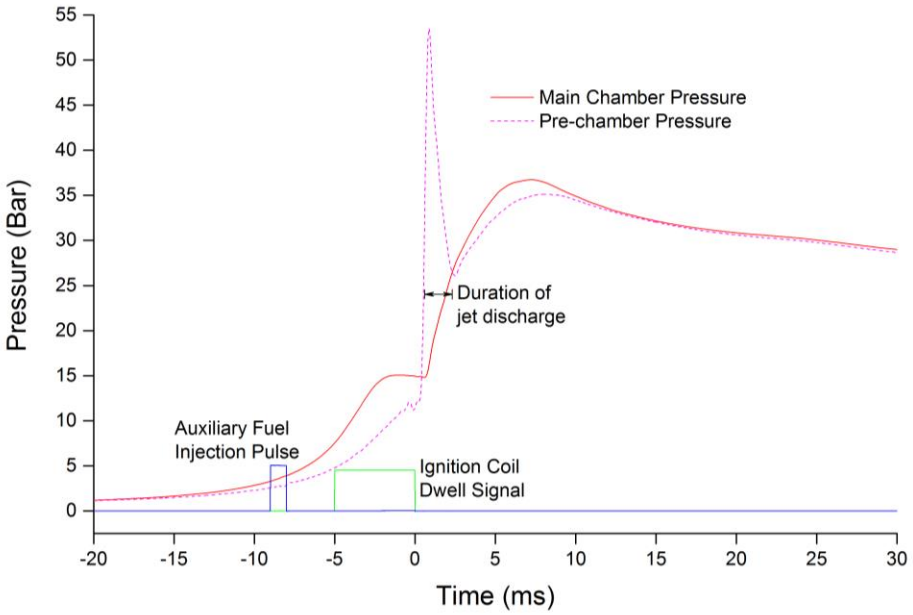

Figure 4-6. Main chamber and pre-chamber pressure traces for λ global= 1.71.

Figure 4-6 shows the main chamber and pre-chamber pressure traces, along with the timing for the auxiliary fuel injection and the ignition coil dwell signal for λ_{global} =1.71. An interesting feature of the pressure traces shown in Figures 4-4, 4-5, and 4-6 is the appearance of an inflection point in the main chamber pressure rise indicating a change in the rate of combustion. From observing the relationship between the optical images and pressure traces, this seems to be related to the end of the jet discharge event. It is well known that turbulence is both highly dissipative, and enhances the rate of combustion dramatically [3, 33, 34]. If the source of turbulence is no longer applied, then the turbulence intensity dissipates quickly, along with a decrease in the rate of combustion [33]. The mode of combustion is another likely explanation for the apparent decrease in burning rate. While the jet is discharging, the rate of combustion is enhanced by the accompanying fluid motion and jet penetration. Of course, after the jet discharge event ends the speed of combustion is no longer assisted by this bulk jet fluid motion, and the combustion mode will be more similar to traditional flame propagation in a lean mixture.

4.2.2 Combustion Visualization

Combustion visualization of the TJI process was performed using a high speed color camera. Figure 4-7. shows a comparison at λ=1.75 between TJI without auxiliary injection, and TJI with auxiliary injection of propane into the pre-chamber.

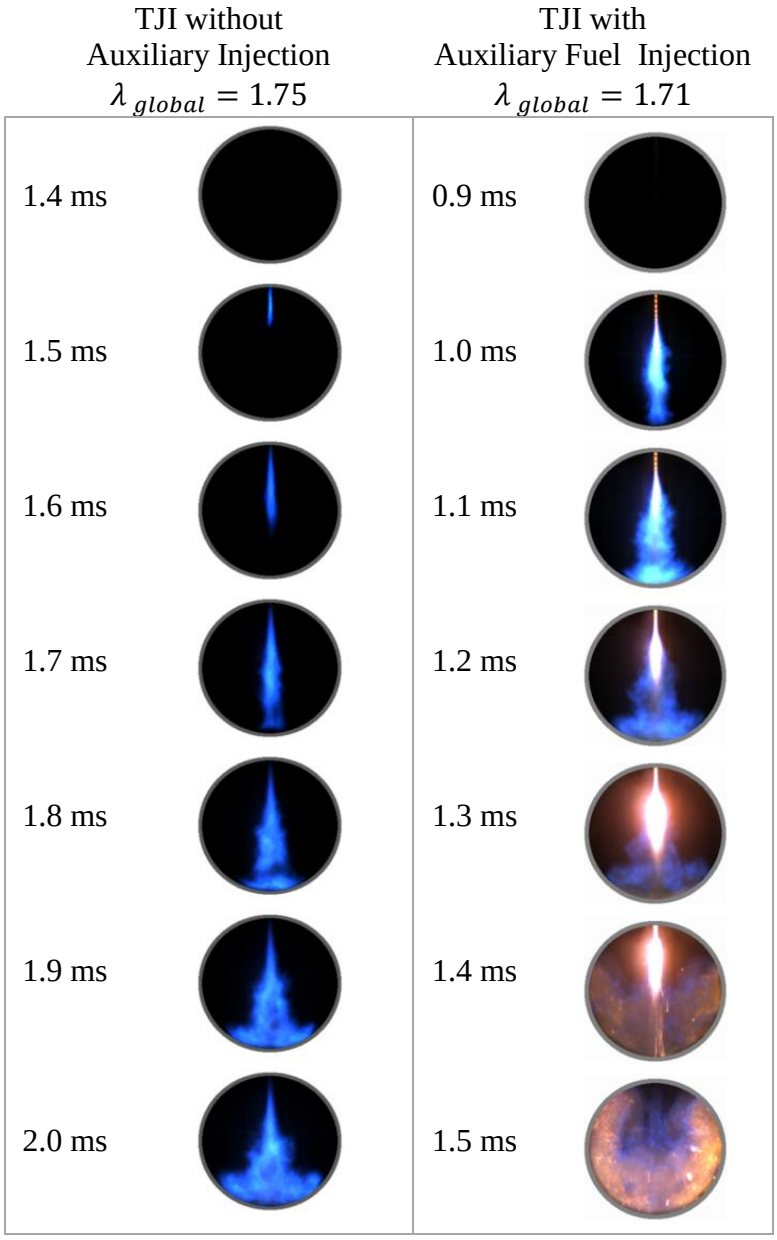

Figure 4-7. Visual comparison of TJI for no auxiliary injection (left) and auxiliary injection of liquid propane (right) at λ= 1.75 (main cylinder).

The jet ignition case without any auxiliary injection produced a lean pre-mixed flame exhibiting blue chemiluminesence. The ignition process with auxiliary injection appears to be quite different than without auxiliary injection. With Auxiliary injection, the process appears faster, with a jet emerging into the main-chamber of the RCM faster relative to the unfueled case. Noticeably, a bright luminous region in the jet also develops as the rich pre-chamber contents continue to discharge, which may indicate soot formation. Figure 4-8 gives an additional comparison of the TJI process with one case having an auxiliary fueled pre-chamber, and two cases without auxiliary fuel injection at λ=2.0.

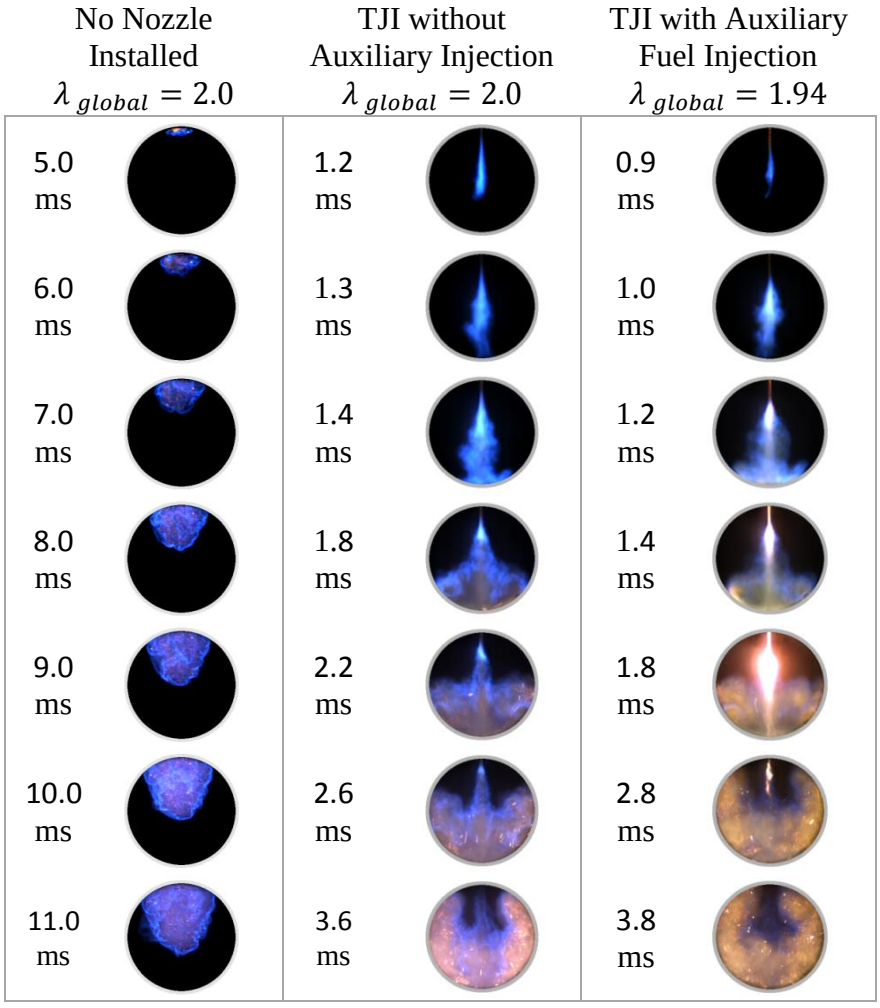

Figure 4-8. Optical comparison of TJI for different nozzle arrangements and pre-chamber fueling.

In order to show the important effect of the nozzle geometry, one case is tested with the nozzle not installed. When the nozzle is not installed, there is still a small flow restriction of 6.4 mm in the pre-chamber followed by an expansion to 12.7 mm which is the diameter of where the nozzle threads in, but the resulting combustion appears to more closely resemble spark ignition with a relatively slow deflagration that traverses the charge. In contrast, with the 1.5 mm nozzle installed the hot products of combustion penetrate into the main-chamber at a faster velocity, reach the combustion chamber walls and begin to consume the rest of the unburned mixture. The auxiliary fueled case again shows an initial jet penetration followed by a luminous region that develops near the exit of the nozzle due to the discharge of the rich pre-chamber contents.

Figure 4-9 shows the ignition process near the lean limit. Referring back to the pressure traces in Figure 4-5, λ=3.35 is shown as the experimental lean limit. However, the next test at λ=3.46 still shows a pressure rise after spark initiation has been initiated in the pre-chamber. Based on the optical images, and the low pressure amplitude it was deduced that this pressure rise is due to combustion occurring successfully in the pre-chamber, with a hot jet of products discharging into the main-chamber, but without ignition occurring in the main chamber charge due to the absence of any significant exothermic reactions. For the case when λ=3.35, the images show that after about 3.6 ms, combustion is initiated in the main-chamber as evident by the blue chemiluminesence visible near the bottom of the main chamber cylinder. As the jet hits the combustion chamber walls, the bulk jet motion is guided by the walls towards the unburned mixture and combustion is enhanced by the increased turbulence and jet velocity. However, from the optical images it also seems apparent that after this initial stage of jet discharge accompanied by bulk jet wall motion, that the jet discharge event ends and the rate of combustion decreases.

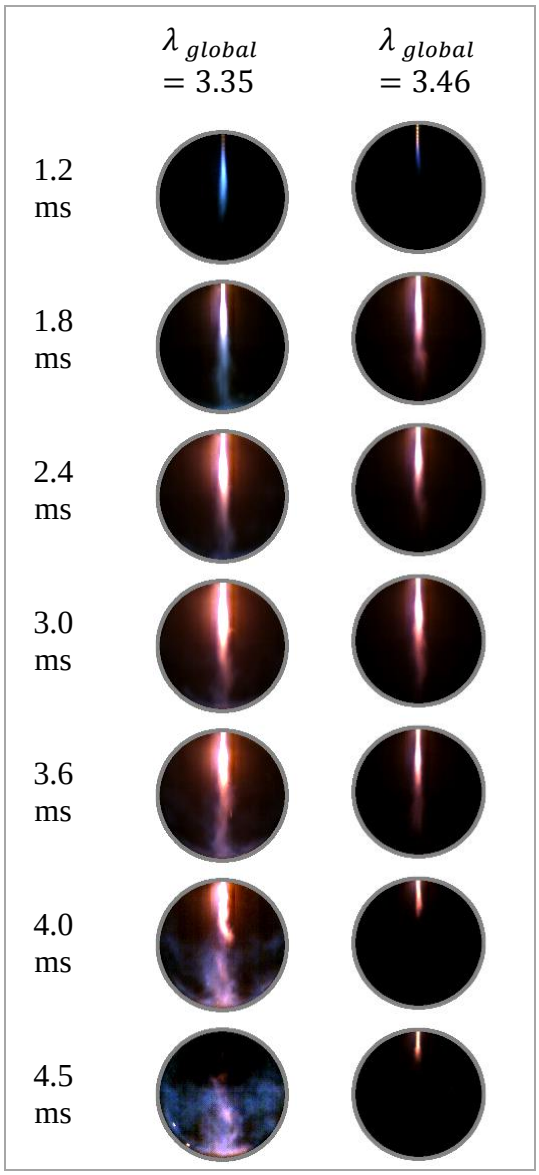

Figure 4-9. Visual comparison of TJI near the lean limit. λ=3.35 shows the discharging jet initiating combustion, while the hot jet from the λ=3.46 case fails to initiate combustion.

Figure 4-10-a shows optical images obtained that correspond directly to the pressure traces shown in figure 4-6. Figure 10-b gives images obtained using a Photron SA5 monochrome camera, with a color map applied to visualize gradients in pixel intensity. In this case, the differences in intensities are more obvious between the luminous discharging jet, and the flame that is initiated in the main chamber. Similar behavior is seen for the different conditions, and it

can be seen that there is an initial penetration of the jet which is very rapid and begins to initiate combustion in the pre-chamber quickly. From Figures 4-5, 4-6, and 4-10 it can be seen that the point of inflection in the main chamber pressure closely matches the point where the main chamber

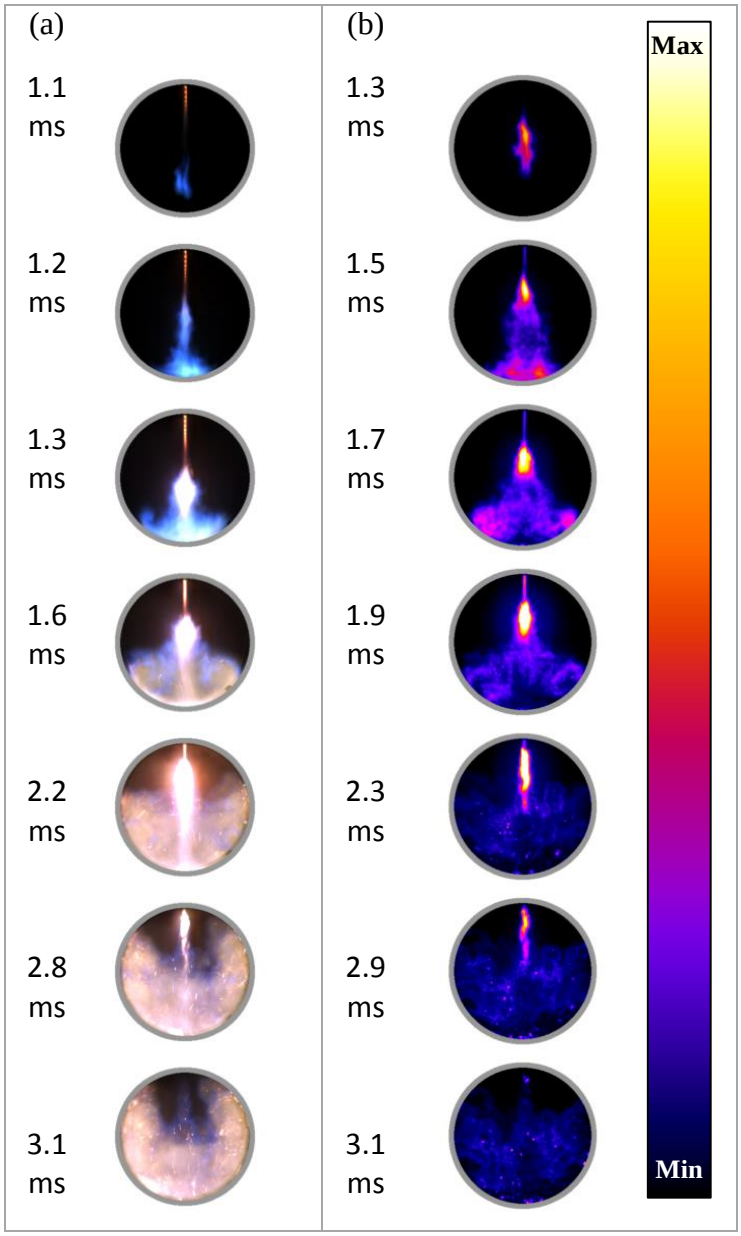

Figure 4-10. Visualization of auxiliary injection at for λ global= 1.71. (a) True color combustion visualization. These images correspond exactly to the pressure trace shown in Figure 4-6. (b) False color visualization with color map to show gradients in pixel intensity.

pressure equals pre-chamber pressure, indicating a flow reversal. This supports the theory that the change in the rate of combustion is likely associated with the end of the jet discharge and either due to turbulence no longer being generated by the discharging jet.

4.2.3 Characterizing the Flow between Pre-chamber and Main Chamber

The λ global =1.71 case is studied in more depth by considering the relationship between the main chamber and pre-chamber pressures. Figure 4-11 shows the difference between the main chamber and pre-chamber pressure, along with the timing of the auxiliary fuel injection pulse and spark timing.

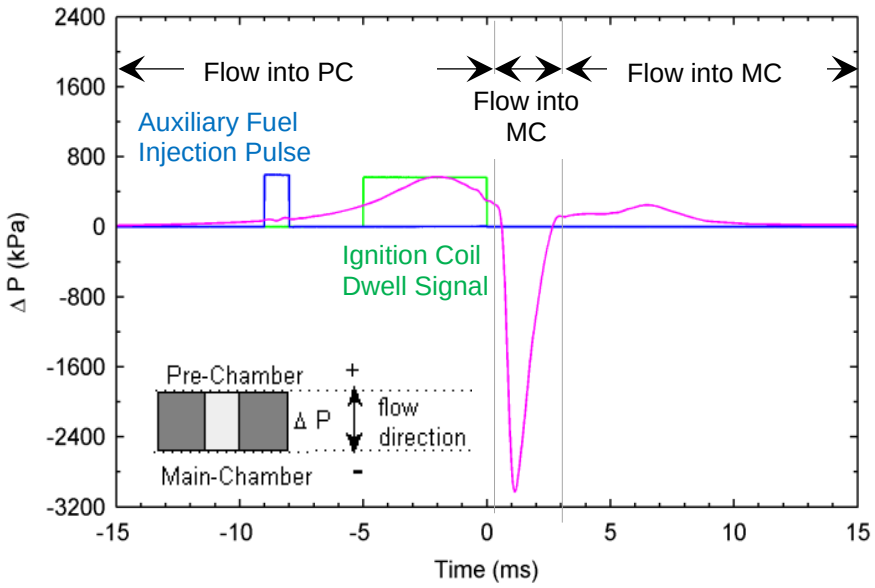

Figure 4-11. Pressure schematic showing pre-chamber pressure, main chamber pressure, spark timing (falling edge), and the pressure differential across the nozzle orifice (main –chamber pressure minus pre-chamber pressure).

The direction of the flow will be governed by the sign of the pressure difference: for positive pressure gradients the main chamber pressure exceeds the pre-chamber pressure, and the flow will be directed into the pre-chamber. This flow condition initially occurs during the compression stroke. For negative excess pressure, the pre-chamber pressure exceeds the main

chamber pressure, and the gasses will be forced out of the pre-chamber into the main-chamber. This condition occurs after spark ignition in the pre-chamber where the rapid rise of pressure in the pre-chamber due to combustion forces the hot products out into the main chamber. The jet continues to discharge into the main chamber, which is associated with a decrease in the pre-chamber pressure, until it ignites the main chamber charge of fuel and air. At this point, due to the combustion of the main chamber charge, the main chamber pressure rises until it exceeds the pre-chamber pressure, causing a flow reversal of combustion gases back into the pre-chamber. For this diagram, a schematic of the nozzle orifice is shown along with an indicator of the flow direction depending on the value of the pressure difference. Figure 4-12 gives another illustration to help the reader visualize the gas exchange process between the pre-chamber and main chamber.

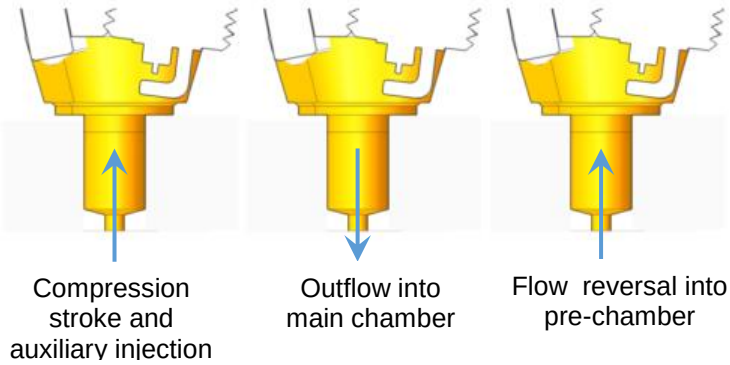

Figure 4-12. Direction of mass flow between the pre-chamber and main chamber.

The pressure difference schematic shown in Figures 4-11, can be a powerful diagnostic tool for interpreting the pressure events and the flow interaction between the pre-chamber and main chamber. Since the discharging jet is essentially the ignition source for the main chamber charge, the duration of the discharge event will be proportional to the energy supplied to the unburned mixture. Ultra-lean mixtures may require longer jet discharge times due to the higher minimum

ignition energy of the mixture [35, 36]. The magnitude of the pressure is also important, as this will also influence the jet penetration and how vigorous the mixing is as the jet discharges.

Another way to characterize the flow is by the pressure ratio across the nozzle orifice. In fact, for compressible flow, the mass flow rate is governed by the pressure ratio. Figure 4-13 gives the ratio of pressures, where the variable η is used for the pressure ratio.

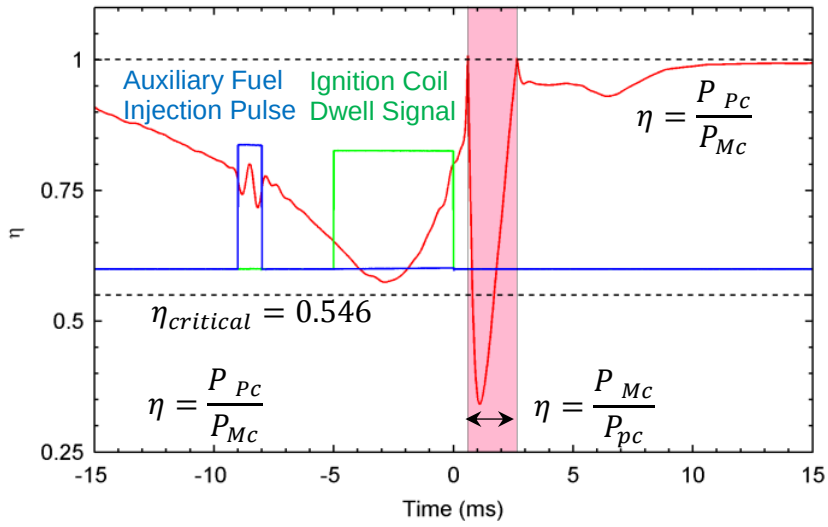

Figure 4-13. Pressure schematic showing the ratio of pressures along with the timing of the control signals. The pressure ratio is evaluated such that the higher pressure is always in the denominator.

The denominator of the ratio is always chosen to be the pressure that is greater; thus initially η is defined as the pre-chamber pressure divided by the main chamber pressure, while η is defined by the reciprocal during the jet discharge event when the pre-chamber pressure is higher. This allows for a standard baseline of η=1 when the pressure between the two chambers is equal, and also allows for a single criterion for determining if the flow becomes choked.

The flow is said to be choked or a critical flow when the velocity becomes sonic at the smallest flow restriction, which gives the maximum flow rate for the given conditions [37, 38]. The critical pressure ratio, that is the pressure ratio at which the flow becomes sonic, is 0.528 for

γ=1.4 and 0.546 for γ=1.3 [38]. Using a conservative estimate as $\eta_{critical}$ = 0.546, and considering Figure 13, it can be seen that the flow does not become choked during the compression stroke, but does for a portion of the jet discharge event. If the nozzle orifice area is decreased further, the flow can become even more choked and lead to ineffective ignition due to 68 the restricted mass flow unable to create a suitable amount of ignition sites [39]. Another issue with a restricted mass flow rate arises in an engine, due to the inability to purge the pre-chamber contents of residual gasses during the exhaust stroke [6]. Additional insight can be obtained by looking at the equations for mass flow rate based on compressible fluid flow through a restriction [38]. For subcritical flow, the mass flow rate is given by

$$\dot{m} = \frac{C_D A_T P_o}{\sqrt{RT_o}} \left(\frac{P_T}{P_o}\right)^{1/\gamma} \left(\frac{2\gamma}{\gamma - 1}\left[1 - \frac{P_T}{P_o}^{(\gamma-1)/\gamma}\right]\right)^{1/2} \quad (1)$$

While for choked flow, the mass flow rate is

$$\dot{m} = \frac{C_D A_T P_o}{\sqrt{RT_o}} (\gamma)^{1/2} \left(\frac{2}{\gamma + 1}\right)^{(\gamma+1)/2(\gamma-1)} \quad (2)$$

Where CD is the discharge coefficient of the orifice, AT is the area at the throat, or the minimum flow area, PT is the pressure at the throat, $P\ o$ is the total pressure, $\gamma$is the ratio of specific heats, To is the total temperature, and R is the universal gas constant. The discharge coefficient CD is defined as the ratio of the actual mass flow to an ideal mass flow. The discharge coefficient is introduced for flows that depart from the ideal conditions (isentropic, reversible, steady, frictionless), and is typically determined primarily through experiments [38]. For the orifice

geometry used, the discharge coefficient is estimated to be 0.8 [40]. By creating a rounded inlet, the discharge coefficient can be increased close to 0.98 [40]. However it is unclear if the increase in mass flow rate would enhance the combustion process due to the increase in surface area which would lead to heat transfer losses and radical losses due to recombination reactions at the nozzle wall [41]. Furthermore, the flow restriction may actually be an advantage as it prolongs the discharge of the hot products which act as the ignition source for the main chamber charge. This flow restriction also reduces the flow of main chamber products back into the pre-chamber, which lead to additional heat transfer losses. Nonetheless, this is interesting to consider for future studies.

4.3 Chapter Summary

In this chapter, a series of experiments were performed studying the behavior of TJI using a liquid propane auxiliary fueled pre-chamber. When operating with auxiliary injection, a substantial extension of the lean limit over the unfueled case was demonstrated. The combustion behavior was characterized, and further insights were obtained by optical observations of the jet ignition process. A pressure difference schematics is presented for λ global =1.71 and shows the flow interaction between the main-chamber and pre-chamber. To further characterize the flow, a pressure ratio schematic is also presented and the flow is determined to only be choked during portion of the jet discharge event. An apparent change in rate of combustion was also observed for the main cylinder pressure traces, and was determined to be related to the end of the jet discharge event. Furthermore, a unique flame structure with auxiliary fueled TJI was observed that has not been seen in other optical studies.

CHAPTER 5: DUAL INJECTOR TJI EXPERIMENTS

5.1 Introduction and Motivation

One reason that lean combustion has not been fully implemented in the automotive industry is that modern three-way catalysts work best near stoichiometric equivalence ratios. As the equivalence ratio becomes lean, expensive exhaust after treatments become necessary. Using TJI with air and fuel injection enables the overall equivalence ratio to remain stoichiometric, while operating with very high dilution levels that lead to increased engine efficiencies. This chapter presents dual injector experiments using methane as the pre-chamber and main chamber fuel, and various levels of charge dilution first using nitrogen and then retained exhaust gases.

5.2 Experimental Set-up

The dual injector TJI system that was used for this set of experiments is shown assembled onto the RCM optical in Figure 5-1. Figure 5-2 shows further details of the TJI pre-chamber, while Table 5-1 gives an overview of the entire experimental set-up.

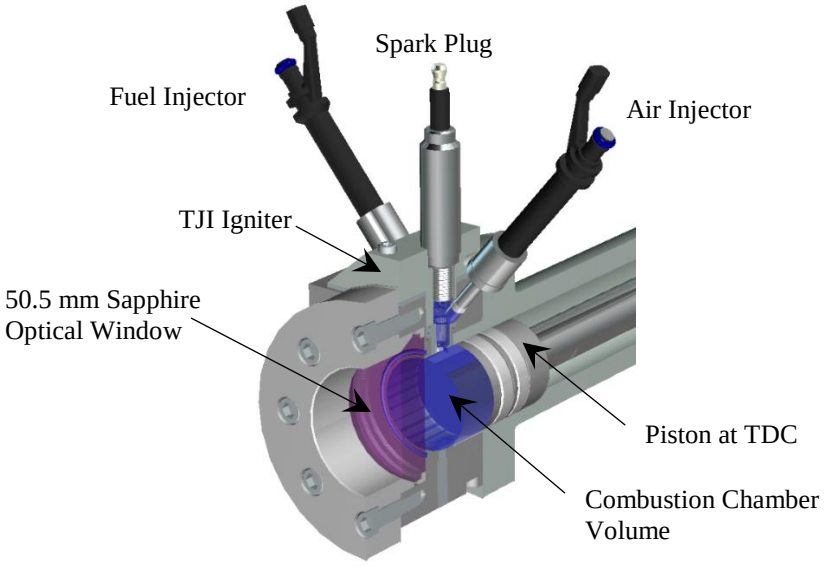

Figure 5-1. Dual Injector TJI system installed onto the RCM Optical Head.

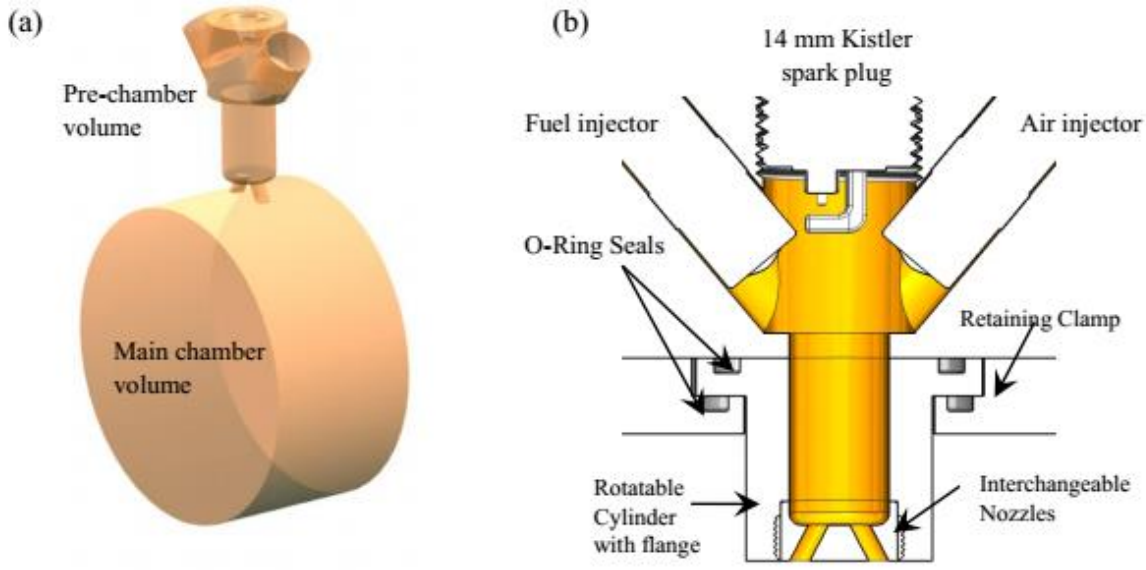

Figure 5-2. (a) Pre-chamber and main chamber geometry (b) Pre-chamber details

Table 5-1. Overview of experimental set-up

Cylinder Wall Temperature	80° C
Compression Ratio used	8.71
Cylinder Capacity	459.33 cm^3
Clearance Volume	53.91 cm^3
Piston Stroke Length	20.32 cm
Cylinder Bore	50.5 mm
Main chamber fuel used	Methane
Auxiliary fuel injector	Audi direct injector OEM Pin: 079906036C
TJI pre-chamber volume	2.35 cm^3
Nozzle Orifice Diameters	D= 2x 2.165 mm
Orifice length	3.0 mm
Electrical Ignition System	Conventional inductive discharge
Power Supply Voltage	13.5 V
Ignition Coil Dwell Time	5 ms
Spark Plug and Pre-Chamber Pressure Sensor	Kistler Type: 6117BFD17
Main chamber pressure sensor	Kistler Type: 6125C

5.3 Experimental Results

5.3.1 Lean Limit Extension

Similar to the experiments that were performed in chapter 4, a series of experiments were performed to determine the lean limit extension using gaseous methane as the fuel. It was unclear prior to performing the experiments if using gaseous methane would be an effective fuel to use. Figure 5- 3. shows the pressure traces from this series of experiments. A dual orifice D=2x 2.165 mm nozzle was chosen since in preliminary experiments it seemed to have better performance near the lean limit. The experimental lean limit was determined to be near λ=3.06. At λ=3.08 ignition occurred in the pre-chamber, but the jet failed to ignite the main-chamber mixture as it was discharging.

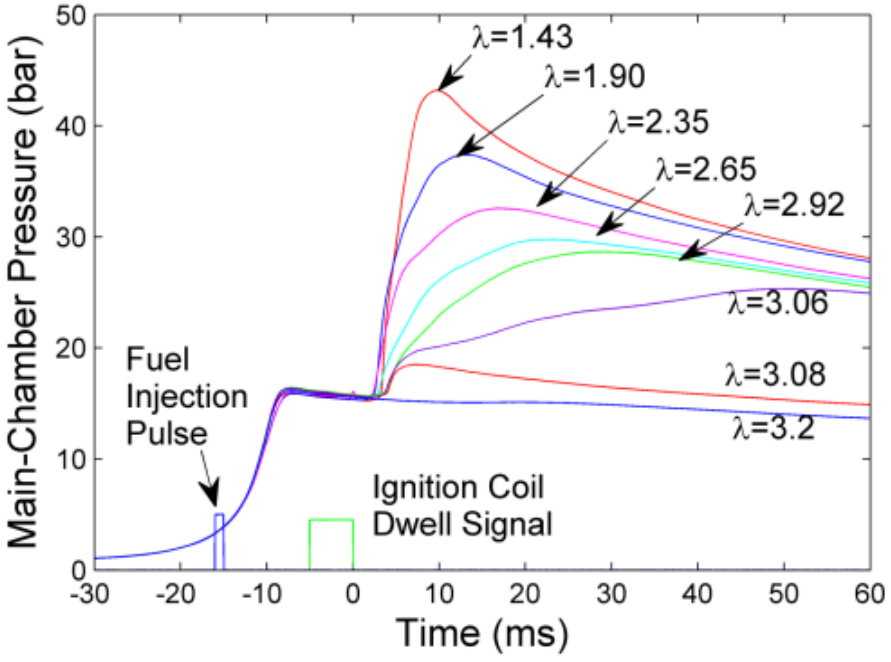

Figure 5-3. Demonstration of lean limit extension using methane

5.3.2 N_2 Dilution Studies

Nitrogen (N_2) is one diluent species that can be added to a fuel-air mixture to dilute the initial concentration of reactant species. This decreases the overall temperature of combustion, thereby reducing the formation of NOx and other pollutants formed at high combustion temperatures. If a stoichiometric ratio of fuel and air is used as the initial mixture prior to dilution, a 3-way catalyst can be used to further decrease the emissions in an engine. However, increasing the dilution level makes the mixture increasingly more difficult to ignite. With TJI, we can control the pre-chamber dilution level by the auxiliary injection of a small mass of air and fuel at a stoichiometric ratio, allowing for easy ignition in the vicinity of the spark plug electrode, but with increased global levels of dilution overall. In the RCM the initial charge of fuel and air is supplied using the method of partial pressures, with the final pressure of the mixture approximately atmospheric. When performing a test with N_2 dilution and without any auxiliary injection the total mass of the mixture is kept the same. In other words, this means that slightly less fuel and air is initially present and the mass of the diluent species increases while keeping the total mass of the system constant. This same principle is applied when using auxiliary injection of air and fuel. In this case, the injected masses of air and fuel are subtracted from the initial masses present to keep the overall mass of the system constant. Equations 5.1-5.4 give the mathematical relationships used when preparing the mixtures in the RCM.

$$\lambda = \frac{\frac{m_{air}}{m_{fuel}}}{\left(\frac{m_{air}}{m_{fuel}}\right)_{stoichiometric}} \tag{5.1}$$

$$N_2\ Dilution\ \% = \frac{m_{N_2}}{m_{air} + m_{CH_4} + m_{N_2}} \times 100\% \tag{5.2}$$

$$\text{total mass} = \left(m_{air} + m_{CH_4} + m_{N_2}\right)_{Initial} + \left(m_{air} + m_{CH_4}\right)_{Injected} \quad 5.3$$

$$\text{Injected mass fraction} = \frac{\left(m_{air}+m_{CH_4}\right)_{Injected}}{\left(m_{air}+m_{CH_4}+m_{N_2}\right)_{total}} \times 100\ \% \quad 5.4$$

First to determine a performance baseline, tests were performed with increasing levels of dilution, but without any auxiliary mixture injection. Figure 5-4 shows the experimental pressure traces from the RCM main-cylinder for tests with increasing nitrogen dilution. Three tests were performed at each condition to obtain a sense of the relative combustion stability. With 0% dilution, combustion occurs rapidly and is most stable with little variation between the tests. At 30% N_2 dilution, the pressure amplitude is smaller, and some test-to-test variation becomes apparent. Even more variation is present at 35% N_2 dilution, an indication of the onset of unstable combustion. Only one of the three tests at 40% N_2 dilution was successful, and even then, the ignition delay was very long.

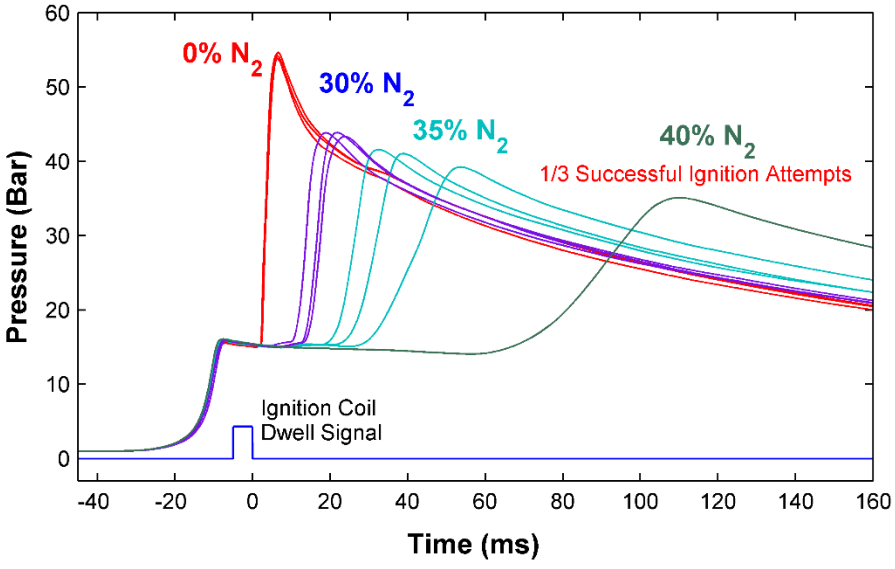

Figure 5-4. Experimental pressure traces when increasing N_2 dilution

Once the performance baseline was established for increasing dilution levels without auxiliary injection, the goal was to try to improve the performance by controlling the mixture dilution level in the pre-chamber so that the mixture could more easily ignited in the pre-chamber. In this case, the auxiliary injection of a stoichiometric mixture into the pre-chamber creates a stratified charge with the pre-chamber composition differing from the composition in the main chamber. In order to demonstrate the improved performance when operating with auxiliary injection, the 40% N_2 operating point was chosen to work with and try to improve upon. Figure 5-5 shows the results from these auxiliary injection tests.

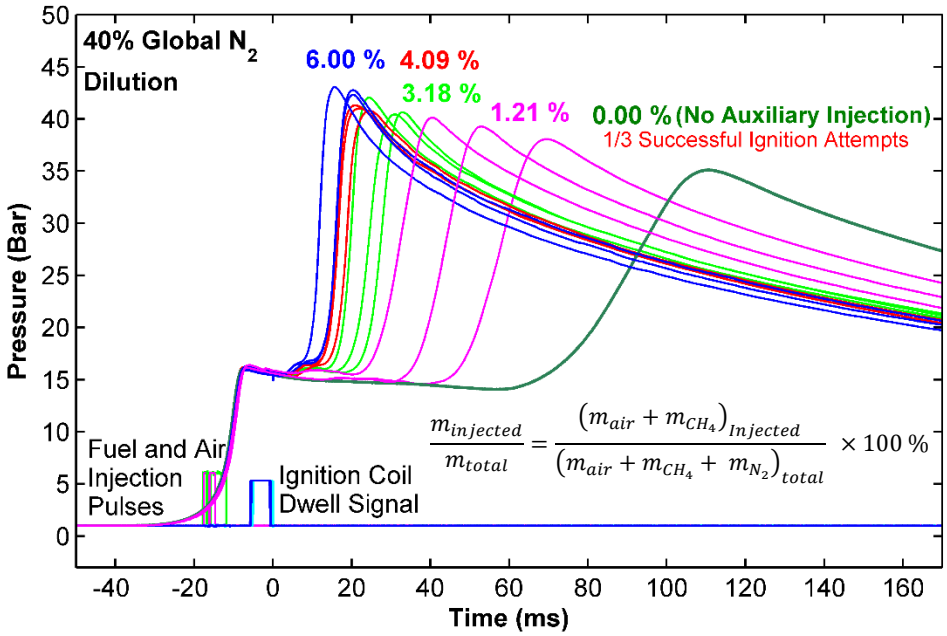

Figure 5-5. Demonstration of improved combustion stability operating with 40% N_2 dilution.

First, a small percentage of injected air and fuel mass (1.19% injected mass fraction) was chosen to see if the performance would improve with the 40% overall N_2 dilution. Indeed, when operating with the auxiliary injection mass fraction, ignition occurred for all three tests, however,

the variability between these tests was still significant implying unstable combustion at these conditions. For lean combustion in an engine, high combustion variability is unacceptable and effectively sets the lean operating limit in an engine [65]. When increasing the injected mass fraction to 3.08%, the combustion stability improved. There appears to be a limit to improving the performance by increasing the injected mass fraction with values of 3.92% and 6.0% initiating combustion fastest and having very similar pressure profiles.

Although the overall dilution level is kept constant at 40%, varying the amount of injected mass of fuel and air dramatically affects the behavior of the discharging jets. Figure 5-6 shows a close up view of the first initial pressure rises after spark initiation in the pre-chamber.

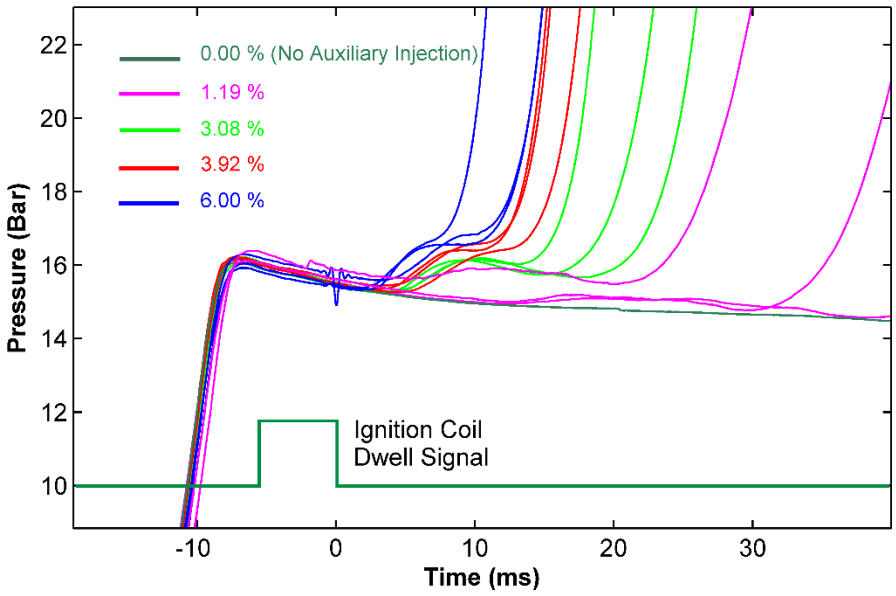

Figure 5-6. Close up view showing details of the pressure rise due to TJI.

The blue curves which correspond to the highest injected mass, exhibited the shortest ignition delay. There is a small pressure rise corresponding to ignition in the pre-chamber, followed by a pressure rise with a steep slope indicating that combustion of the main chamber charge has been

initiated. The green curves corresponding to an injected mass fraction of 3.08 % show an initial pressure rise due to ignition in the pre-chamber, and then the pressure falls as the jet discharges into the main-chamber, but does not initiate combustion as fast. The curves associated with a 1.19% injected mass fraction show a very small increase in pressure initially, and only later after a relatively long ignition delay does ignition of the main chamber occur implying some quenching of the jets.

The optical images obtained, shown in Figure 5-7 support the analysis made from the pressure traces observations. Three auxiliary injection mass fraction cases are shown with 1.19%, 3.0%, and 6.0%.At the smallest auxiliary injected mass of 1.19% some luminous jets are visible initially, but then the flame appears to quench with no luminosity present until about 35 ms into the process where a small region begins to ignite, resulting in a relatively slow

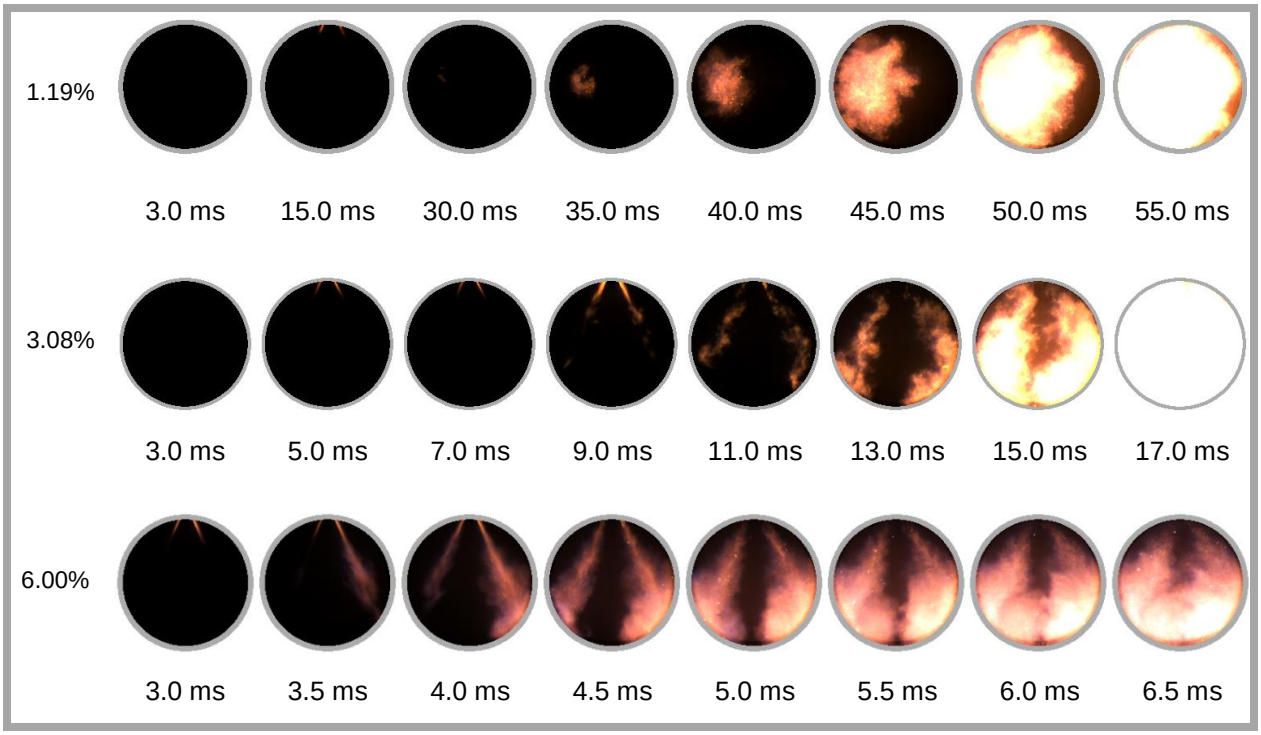

Figure 5-7. Optical Images for 40% N_2 dilution, with varying auxiliary injected mass fractions.

deflagration that traverses the chamber. Increasing the amount of auxiliary injected mass to 3.08% seems to enhance the combustion process, with only partial quenching of the jet, and ignition in the main chamber clearly occurring within the jet structure. Further increasing the amount of auxiliary mixture results in the fastest combustion progression, and with little apparent quenching of the jet as it is discharging. The increase in injected mass fraction clearly showed an increase in combustion stability. This performance enhancement is due to the auxiliary mixture contents being easily ignitable in the vicinity of the spark plug electrode. Another factor that needs to be investigated further is if during the auxiliary injection process, a large proportion of the fuel and air are displaced into the main chamber instead of remaining in the pre-chamber. In this case, the TJI process is no longer strictly a divided chamber, stratified charge ignition concept with two distinct stratified mixtures since the overflowing air and fuel from the pre-chamber will also create a stratified plume in the main-chamber. The effects of stratification are even more complicated when trying to consider the unburned air and fuel that get pushed out of the pre-chamber by the flame front in the pre-chamber during the combustion process

5.3.3 Demonstration of 50% N_2 Mixture Dilution

Many variables can be optimized to increase the allowable dilution level of the mixture. One of the easiest to test is to increase the initial pressure such that the compressed pressure is higher, and thus has a higher temperature to promote ignition. To demonstrate this, a test was successfully performed with a 50% dilution by exhaust gasses and an initial pressure of 2 bar, allowing for the compressed conditions to reach 30 bar. Figure 5-8 shows the pressure traces and control signals used for this experiment and Figure 5-9 presents images captured from the combustion process

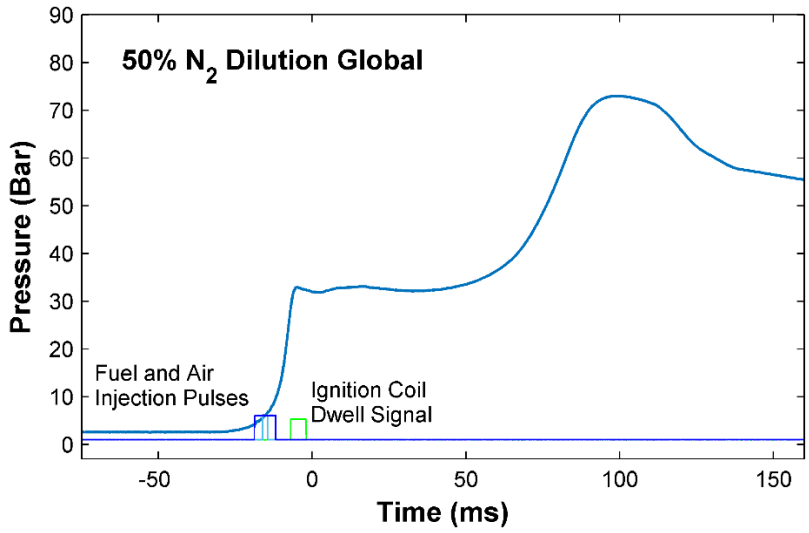

Figure 5-8. Experimental pressure trace demonstrating a test at 50% N_2 dilution level.

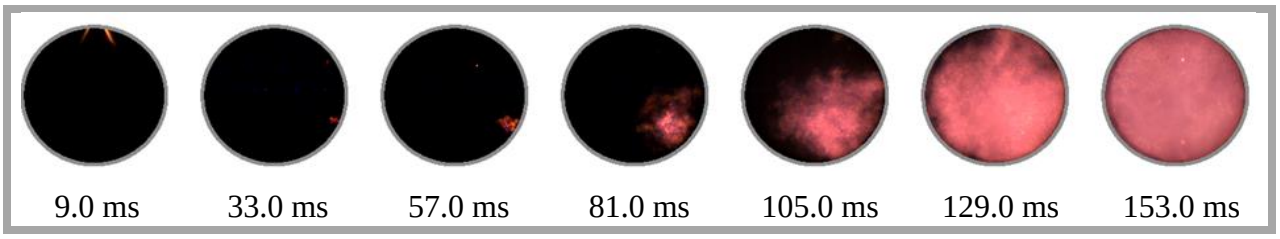

Figure 5-9. Combustion Visualization of TJI at 50% N_2 dilution level.

For the case with 50% N_2 dilution, overall the combustion process was slower than all of the other dilution experiments. Even so, this case is significant since it is a performance benchmark that shows that 50% dilution is possible.

5.3.4 Exhaust Gas Recirculation studies

Similar to the nitrogen dilution studies performed earlier, exhaust gas dilution studies were also performed in the RCM. These studies are perhaps more relevant to engine applications, as many engines currently use Exhaust Gas Recirculation (EGR) as a means to lower the temperature of combustion and reduce the formation of pollutants. For tests with EGR dilution, the dilution level was calculated by percent mass, which is given mathematically as equation 5.5

$$EGR\ Dilution\ \% = \frac{m_{egr}}{m_{air} + m_{CH_4} + m_{egr}} \times 100\% \qquad 5.5$$

To produce the exhaust gas, an initial test was performed in the RCM with a stoichiometric mixture without any dilution. The RCM piston was brought back to BDC and the desired mass of exhaust gasses was left in the cylinder, while the excess exhaust was vacuumed out of the chamber using a vacuum pump. Next, the desired amount of fuel and air was added to the mixture. Auxiliary injection of a stoichiometric mixture was performed in these cases, with the injected mass fraction chosen to be 4.0% since this was determined to be the optimal value from the nitrogen dilution studies. Figure 5-10 shows the effect of increasing the EGR dilution percentages, with good combustion stability occurring at 30% EGR, but with unstable combustion occurring at 40% EGR even with the optimal injected mass fraction of 6.0%. This can be explained by considering that the mixture composition is different with EGR with the ratio of specific heats causing the compressed temperature of the mixture to be lower. Figure 5-11 shows the TJI process with 30% EGR. From the images, it can be seen that the jets do not fully quench before initiating combustion in the main chamber.

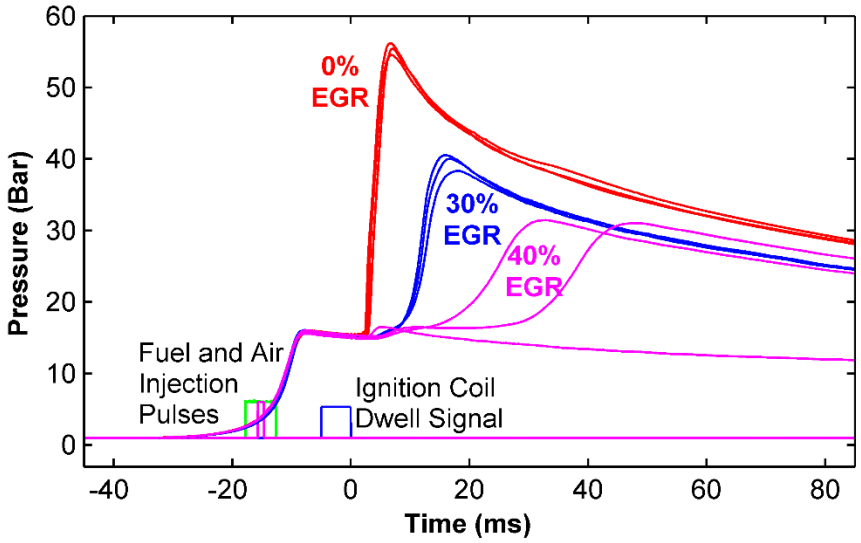

Figure 5-10. Pressure traces showing the effect of increasing EGR.

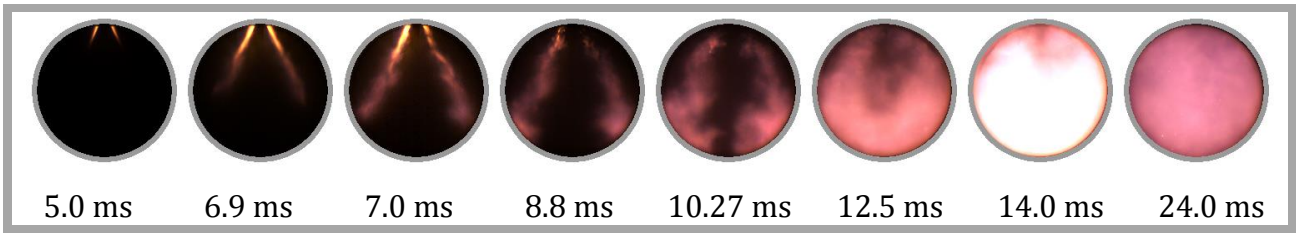

Figure 5-11. Combustion visualization of TJI with 30% dilution by exhaust gases.

5.4 Chapter Summary

In this chapter, an extension of the lean limit to near λ=3 was first demonstrated using gaseous methane as the auxiliary injected fuel. The ability to ignite heavily diluted mixtures with TJI was also demonstrated for both N_2 and EGR as the diluent species. Control of the pre-chamber stoichiometry and injected mass was shown to be critical to the TJI process; for the same global dilution level, different jet ignition behavior was observed from the pressure traces and optical images. For the 40% nitrogen dilution case, combustion was unstable without auxiliary injection. Keeping the global dilution level constant at 40%, but increasing the auxiliary injected mass

fraction by 1.2% combustion stability improved significantly. At this condition, it was seen from the optical images that the jet would discharge from the pre-chamber, mix with the cold unburned gases, quench and reignite the mixture after a delay. Increasing the auxiliary injected mass fraction (fuel and air at a stoichiometric ratio) further to 3.08% and 3.92% showed improvements in the combustion traces as evident by the pressure traces. For these conditions, the optical images only showed partial quenching of the jet during the jet discharge event. By increasing the injected mass fraction to 6.0%, the best combustion stability was achieved, with the least amount of quenching of the hot jet occurring. Another result presented in this chapter was the demonstration of 50% nitrogen dilution, achieved by boosting the initial pressure to two bar instead of atmospheric. This was performed as a benchmark, with room for further studies optimizing all variables. Finally, TJI with EGR dilution was also demonstrated up to a 40% EGR dilution level.

CHAPTER 6: TJI AND HCCI-LIKE COMBUSTION USING ISO-OCTANE

6.1 Introduction

Extensive research on advanced ignition engines that operate lean or highly diluted through low temperature combustion is currently underway as this provides a means to reduce NOx emissions while maintaining fuel efficiency. The combustion of lean and highly dilute mixtures is challenging to implement since as the mixture becomes increasing lean, the burning speed becomes much slower and combustion starts to become unstable. In this case, ignition enhancement allows for faster burning rates and increased stability by either increasing the ignition energy supplied, and/or distributing the ignition source over many ignition sites. Turbulent Jet Ignition is an advanced pre-chamber ignition enhancement technique for spark ignition engines that uses a discharging jet of hot combusting gases to initiate main chamber combustion. The jet acts as a distributed ignition source, leading to fast burn rates and increased combustion stability.

This chapter studies jet ignition and induced autoignition using iso-octane in a rapid compression machine. Several aspects of this chapter are novel. Namely, a custom low-flow fuel injector is used to overcome previous injector hardware limitations of using a liquid fuel spray in the pre-chamber. In the literature, most fueled TJI pre-chamber studies use gaseous fuels such as propane and methane, or vaporized fuels such as gasoline due to the relatively large flow rates and poor mixture preparation of off-the-shelf injectors that are available. In addition, this paper studies the effect of auxiliary fuel variation and ignition distribution due to nozzle orifice geometry. These effects are not fully characterized in the literature. Induced autoignition is another phenomenon studied in this paper, but is not widely studied in the literature with respect to jet ignition.

6.2 Experimental Set-up

Figure 6-1 shows details of the pre-chamber adapter body, which is installed in the top of the RCM optical head. A Kistler spark plug with incorporated pressure sensor threads into the pre-chamber adapter, and there are two ports in the pre-chamber adapter body for fuel injectors to be installed. To complete the pre-chamber assembly, a nozzle with the desired geometry (with one or more orifices) is threaded into the bottom of the pre-chamber. When these components are assembled together, the pre-chamber geometry is defined, with the main chamber connected to the pre-chamber via the nozzle orifices.

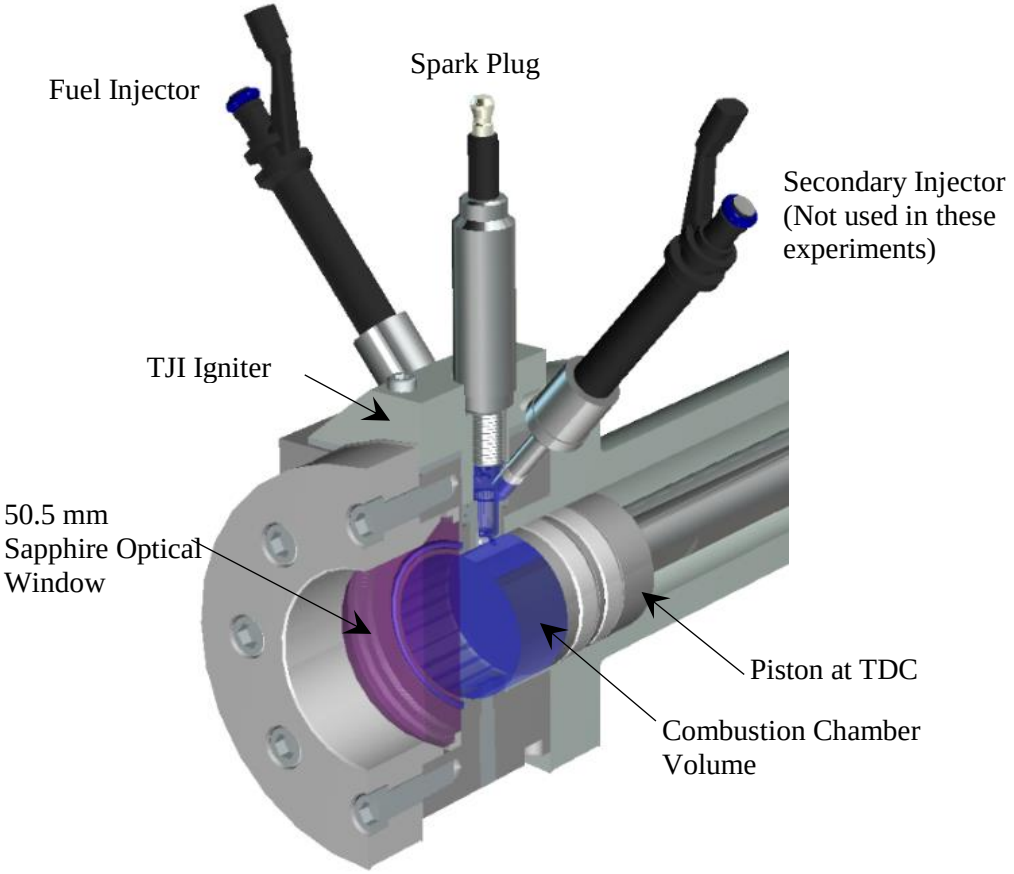

Figure 6-1. Dual Injector TJI system installed onto the RCM Optical Head.

The RCM optical head and cylinder are pre-heated using band heaters, which are controlled by a LabVIEW program. LabVIEW is also used for signal generation (ignition coil dwell signal, fuel and air injection pulses) and data acquisition (control signals, pre-chamber pressure, and main chamber pressure).

Prior to performing a test the combustion chamber is evacuated of all gasses using a vacuum pump through a small port at the bottom of the combustion cylinder. To prepare the initial charge of fuel and air, gasoline is pulsed through the pre-chamber fuel injector into the evacuated cylinder. Since the cylinder pressure is below the vapor pressure of the fuel, the fuel is vaporized and occupies the entire combustion chamber volume (main chamber and pre-chamber).

An absolute pressure transducer is installed onto a small manifold that is connected to the inlet port that allows the cylinder pressure to be measured, thus providing the partial pressure of the gasoline. For the chosen stoichiometry, the partial pressure of air can then be calculated and introduced to the cylinder via the inlet port by using a metering valve connected to a compressed gas cylinder. After the addition of air, the inlet valve is closed and the hydraulic reservoir is pressurized, followed by pressurization of the pneumatic piston. Upon triggering, a solenoid valve is actuated and the high pressure in the hydraulic reservoir vents, which allows the pneumatic piston to drive the coupled piston assembly forward, starting the piston motion. For auxiliary fueled cases, fuel is injected into the pre-chamber early in the compression stroke. The global (initial charge + auxiliary fuel) air-fuel equivalence ratio for the experiments here was held constant at 3.0. The typical mixture preparation time was approximately 3 minutes, which was determined to be an adequate time for pre-mixing. Experiments were performed for 3, 5, 10,

and 20 minutes of pre-mixing time, with no discernable difference in the pressure traces or optical images.

Table 1 provides the different injector pulse widths used and the corresponding stoichiometric conditions. The pre-chamber λ is estimated by assuming that no fuel or air is displaced into the main chamber during the fuel injection event, since injection occurs during the compression stroke and fluid motion should be into the pre-chamber. The mass fraction m_i is also given, which is the ratio of the injected fuel mass to the total mass. Table 2 provides an overview of the entire experimental set-up.

Table 6-1. Testing conditions for different auxiliary fuel injection pulse widths.

PW (ms)	λ_{global}	$\lambda_{main\ chamber}$	$\lambda_{pre\text{-}chamber}$	m_i
0.00	3.0	3.0	3.0	0.0 %
0.50	3.0	3.02	2.60	0.7 %
0.75	3.0	3.15	1.25	6.6 %
1.00	3.0	3.30	1.06	8.6 %
1.25	3.0	3.35	0.93	10.7 %

Table 6-2. Overview of RCM experimental set-up

Cylinder Wall Temperature	120° C
Compression Ratio used	11.2
Cylinder Capacity	564.4 cm^3
Clearance Volume	50.63 cm^3
Piston Stroke Length	254 mm
Cylinder Bore	50.5 mm
Compressed pressures at TDC	2000 kPa
Main chamber fuel used	Iso-octane
Auxiliary fuel	Iso-octane
Auxiliary fuel injector	Bosch Direct Injector (proprietary "low flow" design)
TJI pre-chamber volume	2.51 cm^3
Nozzle Orifice Diameters	D= 2x 2.26 mm, D=1x 3.16 mm
Orifice length	3.0 mm
Electrical Ignition System	Conventional inductive discharge
Power Supply Voltage	13.5 V
Ignition Coil Dwell Time	5 ms
Spark Plug and Pre-Chamber Pressure Sensor	Kistler Type: 6117BFD17
Main chamber pressure sensor	Kistler Type: 6125C
High Speed Camera	Photron SA4
Objective lens	Nikon 50 mm f/1.2

6.3 Results and Discussion

Experiments were performed to determine the effect of varying the amount of auxiliary fuel mass and nozzle geometry. The single orifice and dual orifice nozzle were designed to have nearly equivalent cross sectional area, with dimensions of D=1x 3.16 mm and D=2x 2.26 mm, respectively, with slight differences in the area due to selecting the nearest drill size during machining. As a baseline, tests were first performed with no auxiliary fueling. For the auxiliary fueled cases injector pulse widths 0.5 ms, 0.75 ms, 1.0 ms, and 1.25 ms were used, corresponding to increasing quantities of injected mass.

The global air-fuel equivalence ratio is kept constant at $\lambda=3$, thus for increasing amounts of auxiliary fuel mass, less fuel is present in the initial mixture in order to keep the total amount constant. Each experiment was performed five times to obtain some idea of the combustion stability and variability of the data. The experimental pressure traces for both nozzle geometries are shown in figure 6-2, with the dual orifice results presented in figure 6-2a, and the single orifice results in figure 6-2b. The timing of the auxiliary fuel injection event was set to be early in the compression stroke, about 10 ms before the end of compression and was held constant for each test. Likewise, the spark timing was also constant for each test and occurred 7 ms after TDC (the spark occurs on the falling edge of the ignition coil dwell signal). In the figures, the time datum is chosen so that the time equals zero at the spark event. From the pressure traces, it can be seen that for increasing pulse widths, i.e. higher ratios of injected fuel mass, the combustion stability improves and the overall ignition delay is shortened. Another interesting feature that is apparent is that the two nozzles appear to produce different pressure profiles at the various pulse width conditions. Differences include the amount of variation in the curves, as

well as differences in the general shape of the curves with inflection points occurring at different locations.

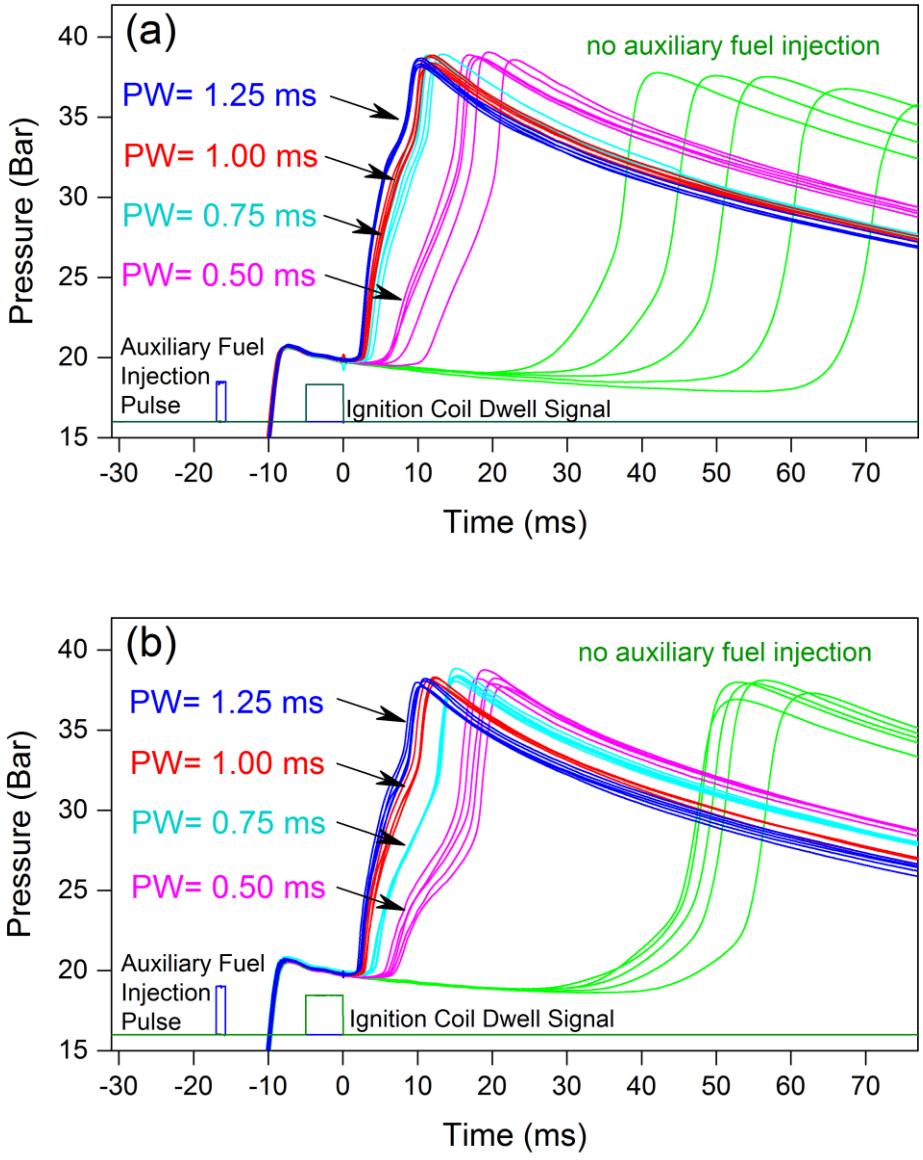

Figure 6-2. Experimental pressure traces for (a) dual orifice and (b) single orifice nozzle geometries

To compare between the two different orifice geometries used, the average of the five experimental curves for each auxiliary fueled condition and nozzle are plotted together in Figure 6-3.

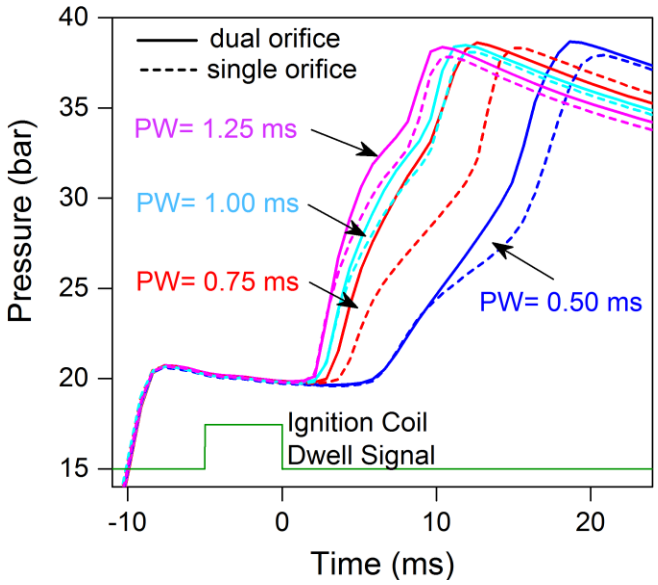

Figure 6-3. Average experimental pressure traces for dual orifice and single orifice nozzle geometries

In general, the pressure traces for the dual orifice tests precede the single orifice cases. With the exception of the 0.75 ms case, the pressure curves for both nozzles appear to match during the initial pressure rise, and then begin to deviate from each other. This implies that for the higher auxiliary injected mass, the conditions for ignition are stable and nearly the same, and that the differences in combustion are due to factors that occur later in the combustion process. However, this may be a somewhat misleading result in the case of PW= 0.5 ms, as there is considerable variation in the pressure traces, and just by chance the average pressure traces match initially (see Figure 3).

The ignition quality and speed of combustion can be determined quantitatively from the pressure traces by considering the duration of combustion. In previous RCM studies, the duration of 0%-10% of the pressure rise due to the combustion has been used to characterize the ignition stage, while the duration of 10%-90% of the pressure rise gives an indicator of how quickly the combustion of the overall charge occurs once ignition has been initiated [47]. Figure 6-4 shows a pressure diagram of a typical pressure trace, with annotations detailing the definition of these burn durations. Initially there is a pressure rise due to the piston motion. For auxiliary fueled cases, fuel is injected towards the beginning of the compression stroke. At the end of compression the piston has reached TDC and remains in that position until after the test is complete, creating a constant volume condition in the combustion chamber for the entire test. The spark in the pre-chamber is initiated shortly after TDC, with the time datum zero corresponding to the moment of the spark discharge event.

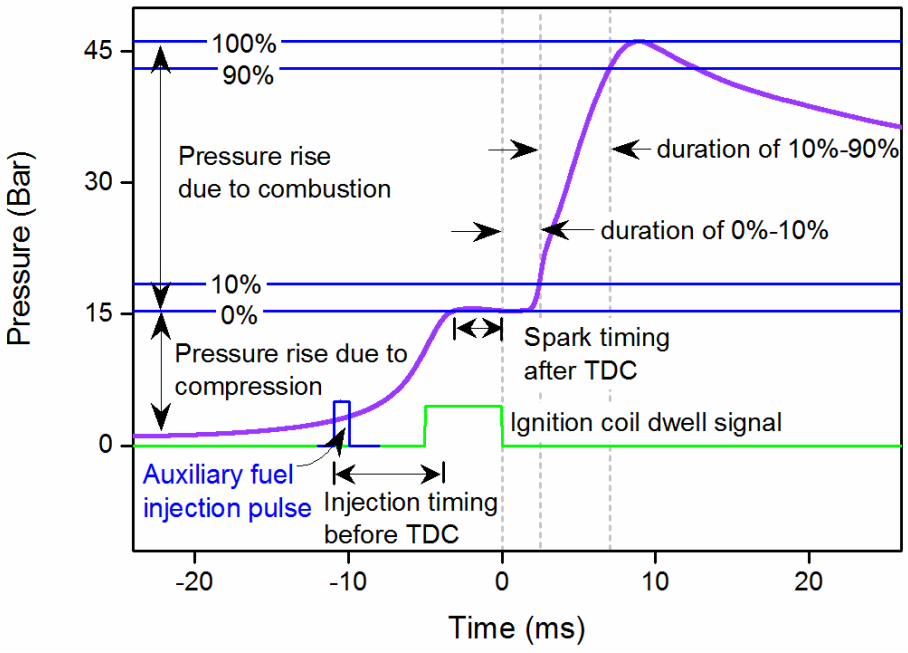

Figure 6-4. Typical pressure trace showing definition of burn durations

This produces a pressure rise strictly due to combustion, since the piston is stationary and the combustion chamber is at constant volume. The pressure reaches a maximum, and subsequently falls due to heat transfer to the surroundings. The pressure is then scaled so that 0% corresponds to the pressure at the time that the spark plug fires, and 100% corresponds to the maximum pressure achieved.

The mean 0%-10% and 10%-90% burn durations for the auxiliary fuel variation experiments are shown in Figure 6-5 for both nozzles, with the error bars representing the standard error of the mean.

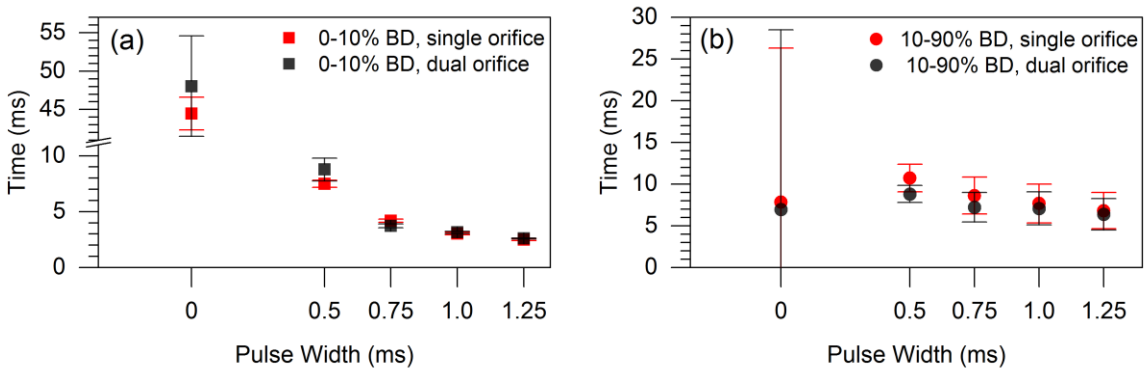

Figure 6-5. (a) 0%-10% burn durations (b) 10%-90% burn durations

It can be seen that the 0%-10% burn duration for the non-auxiliary fueled case is much longer compared to the auxiliary fueled cases. The relatively large error bars also demonstrate the variability in the pressure traces as seen in Figure 6-2. These results indicate poor ignition quality due to the very lean mixture in the vicinity of the spark plug. For the non-auxiliary fueled case and for a pulse width of 0.5 ms, the single orifice has a faster 0%-10% burn duration than the dual orifice nozzle, while for pulse widths of 0.75 ms, the dual orifice nozzle has a faster 0%-10% burn duration. For pulse widths of 1.0 ms and 1.25 ms, the burn durations are the shortest and nearly identical for the two different orifices.

These results can be further interpreted by considering the physics that are occurring. The jet acts as a distributed ignition source, with the combusting jet either being channeled through a single orifice or being channeled through two orifices with an equivalent cross-sectional flow area. The dual jets will have a greater surface area, increasing the volume of colder unburned mixture that can be entrained, which decreases the bulk temperature of the jet in addition to the convective and radiative heat transfer losses that are also associated with an increased surface area. In addition, for the leaner cases, the adiabatic flame temperature is lower and the minimum ignition energy is higher. For these reasons, the jet that issues from the single orifice nozzle produces an ignition source that is more concentrated and able to reach the minimum ignition energy threshold more easily. Once the auxiliary fuel loading is increased, the mixture stoichiometry in the pre-chamber is closer to stoichiometric and is easily ignitable. With a lower minimum ignition energy threshold for these cases, both the single orifice and dual orifice jets produce ignition sources that reliably and rapidly initiate combustion in the main chamber.

From figure 6-5 it can be seen that the 10%-90% burn durations for the non-auxiliary fueled cases are comparable to the auxiliary fueled cases, but with much greater variability. Initially, the relatively fast burn duration for these cases was surprising since the ignition quality was poor as determined by the 0%-10% burn duration. Upon closer inspection of the pressure traces (Figure 6-2) and the optical images (Figure 6-6), it was determined that the jet discharge was inducing autoignition of the unburned charge in the main chamber. This enhances the overall rate of combustion, though causes high variability of when the onset of autoignition would occur, particularly for the non-auxiliary fueled case. It is important to note that when examining the raw pressure traces, there is no evidence of the high-frequency pressure

oscillations that are associated with knocking combustion. This is likely because the pressure rise rates are not excessively high, the end-gas volume is small, and the overall lean conditions lead to lower temperatures and pressures than what would occur during stoichiometric combustion.

At a pulse-width of 0.5 ms the 10%-90% burn duration is a few milliseconds slower than the case without auxiliary fuel loading, but with dramatically improved stability apparent from the relatively small size of the error bars. As the injector pulse width is further increased, the 10%-90% burn duration becomes shorter indicating faster combustion overall. For all cases, the dual orifice jet results in a shorter 10%-90% burn duration due to the increase in surface area and the volume of entrained reactants.

Figure 6-6 shows the optical images obtained for the two different nozzle geometries for an auxiliary fueled condition using a 1 ms pulse width, and a non-auxiliary fueled condition for comparison. Images were selected so that similar features are shown in each frame i.e. the first set of images show the development of the jet, while the later frames show autoignition events. Due to these events occurring at different times, the time steps are indicated for each image sequence presented. The brightness and contrast for each image is enhanced using ImageJ, an image processing software available for download by the National Institutes of Health [51]. In addition, the auxiliary fueled cases and non-auxiliary fueled cases were captured at different frame rates. Although the luminosity intensity appears comparable for the images shown in Figure 6-6, the emission of light is orders of magnitude higher for the auxiliary injected cases taken at the faster frame rate than for the case without auxiliary fuel injection, which was taken at the slower frame rate.

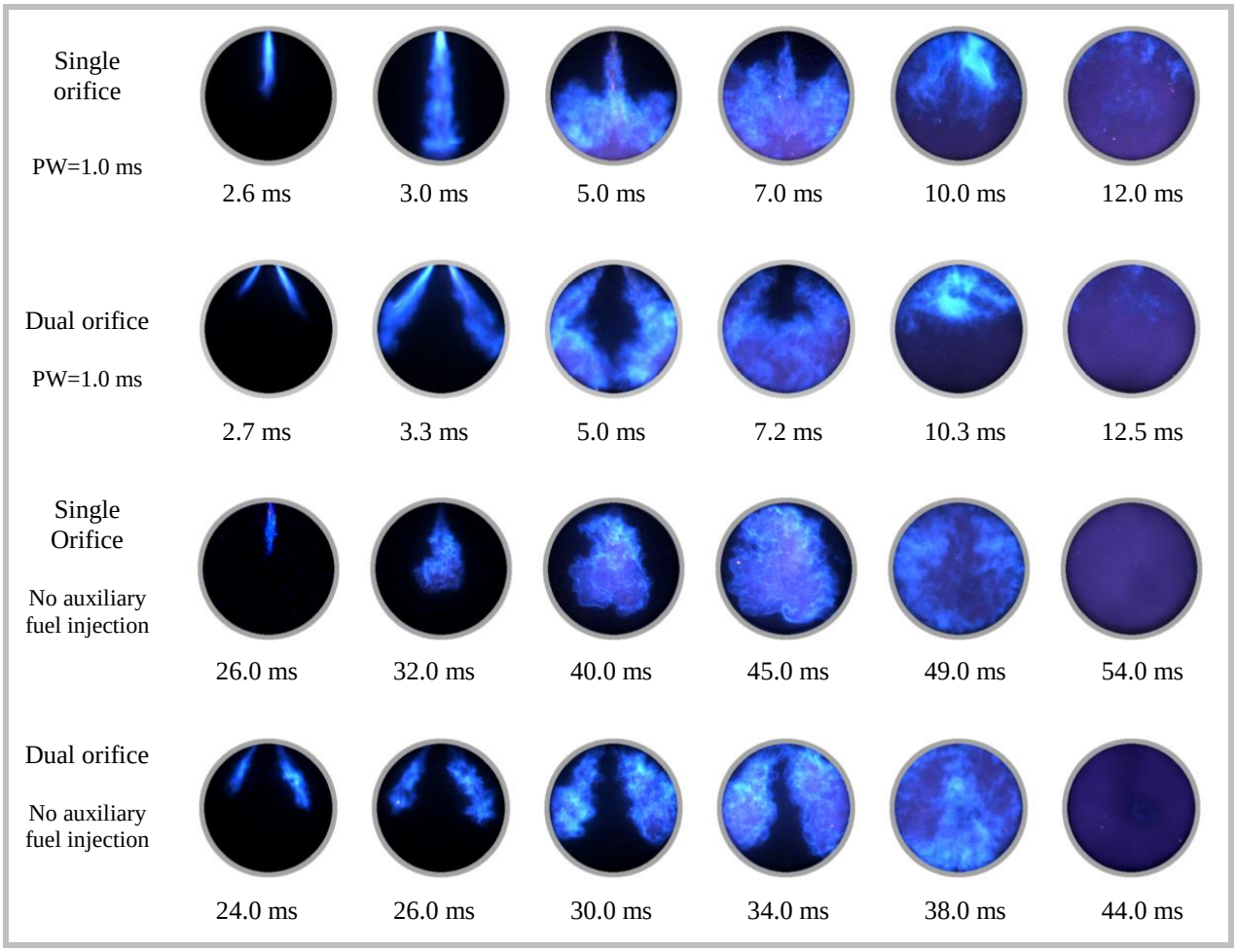

Figure 6-6. Combustion visualization of dual and single orifice TJI for non-auxiliary fueled jet ignition and jet ignition with auxiliary fuel injection (PW=1.0 ms).

For the auxiliary fueled jet ignition cases that are presented, there is stratification of the charge, with the pre-chamber becoming enriched and a leaner main chamber. The reacting jet discharges quickly, with a high momentum resulting in a narrow column of fluid that penetrates the chamber and reaches the end wall. For the jet issuing from the single orifice nozzle, a stagnation zone is created at the bottom of the cylinder and a wall jet is formed, where the fluid flow is bounded by the cylinder wall and directed upwards towards the unburned mixture. Combustion is enhanced by this fluid motion, and shortly thereafter the jet discharge event ends

followed by a slower deflagration that continues to propagate. The end gas, which is defined as the remaining fuel and air mixture that has not been consumed, is being compressed by the flame front. Autoignition of the end gas then occurs, where the remaining fuel-air mixture is rapidly consumed. This is evident by the much brighter chemiluminesence of the reacting mixture compared to the region of burned gases, where the fuel and air has already been consumed by the jet. Furthermore, the duration of the autoignition event is very short and corresponds to the rapid rise in pressure as seen in the pressure traces in Figure 6-2.

For the auxiliary fueled dual orifice jet, the shape is also narrow initially, but with this nozzle the two jets impinge on the side of the cylinder creating a fluid motion that directs the hot jets toward the unburned mixture at the bottom of the cylinder. When the two jets meet, they create an opposed jet flow, enhancing mixing and entrainment of the unburned mixture. Combustion occurs within this flow field, and a flame front propagates upward towards the unburned charge, compressing the end gas in the process. Similar to the single orifice case, the unburned mixture experiences autoignition with the fuel and air being consumed rapidly. However, the location and proportion of unburned mixture that is available for autoignition is quite different. The dual jets are able to consume more of the mixture before autoignition occurs, with a smaller volume experiencing autoignition. This is evident in the optical images by a clear contrast between the reacting volumes of gases exhibiting chemiluminesence, versus the burned gasses that are not emitting as much visible light. This autoignition behavior can also be observed in the pressure traces in Figure 6-2 where the slope of the pressure traces increases after the initial ignition event.

The ignition behavior is quite different for the non-auxiliary fueled case when there is no stratification of the fuel-air mixture between the pre-chamber and main chamber (λ=3). For the

single orifice case, a colder, slower jet of gases discharge into the main chamber, entraining unburned fuel and air, and initiating combustion near the center of the combustion chamber for the single orifice nozzle. Combustion occurs throughout the jet structure, and the flame starts to propagate outward almost in a spherical manner towards the cylinder walls. The end gas near the cylinder periphery then begins to autoignite, with most of the gases in the core of the jet structure already converted to combustion products.

For the dual orifice non-auxiliary fueled case, the two jets that issue from the dual orifice are also slower, and grow into two jet plumes that compress the unburned gas and induce autoignition faster than the single orifice case. Another result seen for both non-auxiliary fueled cases is that the jets do not penetrate into the chamber as far and do not interact with the chamber walls before autoignition occurs due to the lower initial jet momentum.

The burn duration analysis gives a quantitative interpretation of the overall ignition and combustion, but does not enable the timing of the actual physics that occur to be resolved. For example, the 0-10% burn duration includes the spark discharge event, low-temperature chemical reactions that occur but do not increase the overall pressure, flame kernel propagation and convection within the pre-chamber, mass transfer from the pre-chamber contents being displaced into the main-chamber, and initial jet penetration and ignition of the main chamber charge. In the definition of the 0%-10% burn duration, the percent of the pressure rise is chosen in order to capture the ignition processes that are occurring, with the selection being somewhat arbitrary and not necessarily corresponding to any physics that are actually occurring. Ten percent is typical of this type of analysis, although in the literature one and five percent of the pressure rise are also used [59]. Similarly, the physics that occur during the 10%-90% burn duration are not able to be temporally resolved. These physics include flame propagation, jet impingement, and autoignition

of the unburned mixture. Thus, a more fundamental analysis is needed to study the jet ignition process in more depth and to identify when the physics are occurring.

From Figures 6-2 and 6-3, it can be seen that there are inflection points and changes of curvature in the pressure curves. The first, second, and third derivatives of the pressure data were then taken to identify these points of interest. From the first derivative, it can determined if the pressure is rising or falling by considering if the sign is positive or negative. The change in sign of the first derivative is useful for determining when the end of compression occurs by considering the transition from a positive dP/dt to a negative value, where the pressure is no longer rising and is starting to fall. The same technique can be used to determine the end of combustion when there is no longer any significant generation of pressure due to combustion and heat transfer to the surroundings causes the pressure to decrease. Local maximums of the first derivative are also of interest as these points indicate the maximum rate of change in pressure. The second derivative is closely related to the curvature of the pressure trace. Finding the local maximum of the third derivative then gives the point where the curvature is changing the fastest. When the correct amplitude of the third derivative is chosen, it represents ignition events where the rate of pressure rise is relatively fast such as in jet ignition and autoignition. Thus, characteristic points such as the start of jet ignition in the main chamber, and onset of autoignition can be identified using the derivative curves and the times that they occur can be measured. These characteristic times with their definition and method of identification are given in Table 6-3.

Table 6-3. Definition of characteristic times and method of identification

Characteristic Time		Method of Identification
$\boldsymbol{\tau_0}$:	End of compression	Transition of dP/dt from positive to negative (first occurrence)
$\boldsymbol{\tau_1}$:	Beginning of jet ignition	Auxiliary Fueled: local maximum amplitude of the third derivative Non-Auxiliary Fueled: Transition of dP/dt from negative to positive
$\boldsymbol{\tau_2}$:	Max rate of pressure rise due to jet ignition	Local maximum of dP/dt
$\boldsymbol{\tau_3}$:	Onset of autoigntion	Local maximum amplitude of the third derivative
$\boldsymbol{\tau_4}$:	Maximum rate of pressure due to autoignition	Local maximum amplitude of the first derivative
$\boldsymbol{\tau_5}$:	End of combustion	Transition of dP/dt from positive to negative (second occurrence)

Figure 6-7 shows a pressure trace and 1st, 2nd, and 3rd derivative data for an auxiliary fueled case using PW=1.0 ms, and the dual orifice nozzle geometry. The characteristic points are superimposed onto the original pressure curve. The start of jet ignition and autoignition are identified by finding the local maximum amplitude of the third derivative. Local maximums of the first derivative are also identified, which are the inflection points in the original curve. By studying the optical images, it was determined that these points define intervals in which specific combustion events are occurring. For example, the beginning of jet ignition in the main chamber occurs between the intervals defined by the start of spark discharge at 0 ms, until τ_2, which is a local maximum in the first derivative. During this interval, ignition occurs in the pre-chamber, and there is jet penetration into the main chamber. A second interval associated with jet ignition can be defined from τ_2 until τ_3, where τ_3 identifies the onset of autoignition. This jet ignition interval is characterized by wall impingement, fluid motion, and flame propagation. An autoignition interval is then defined from the onset of autoignition until the end of combustion, i.e. from τ_3 to τ_5. The optical images corresponding to these intervals for figure 6-7 are shown in Figure 6-8.

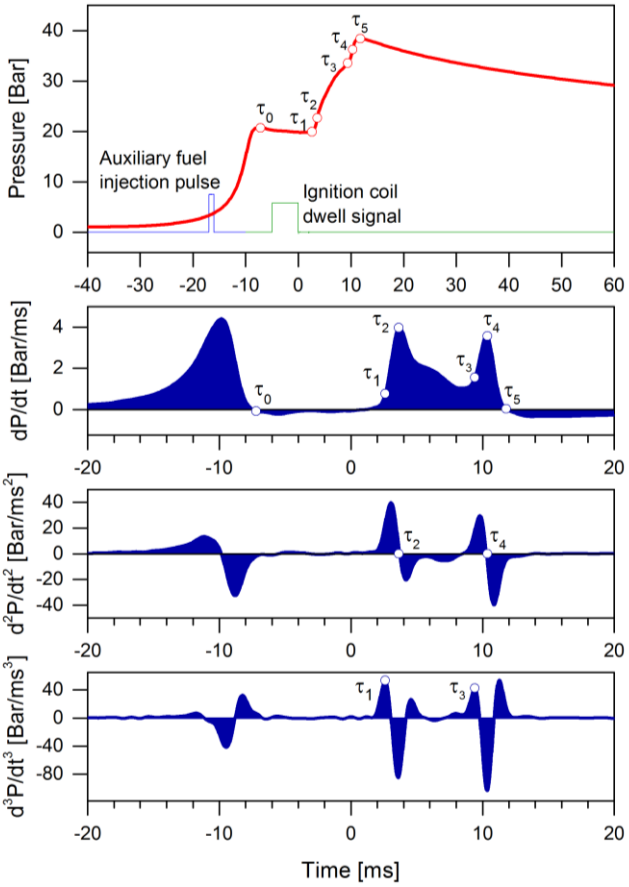

Figure 6-7. Pressure trace and derivative data for the dual-orifice PW=1.0 ms auxiliary fuel case.

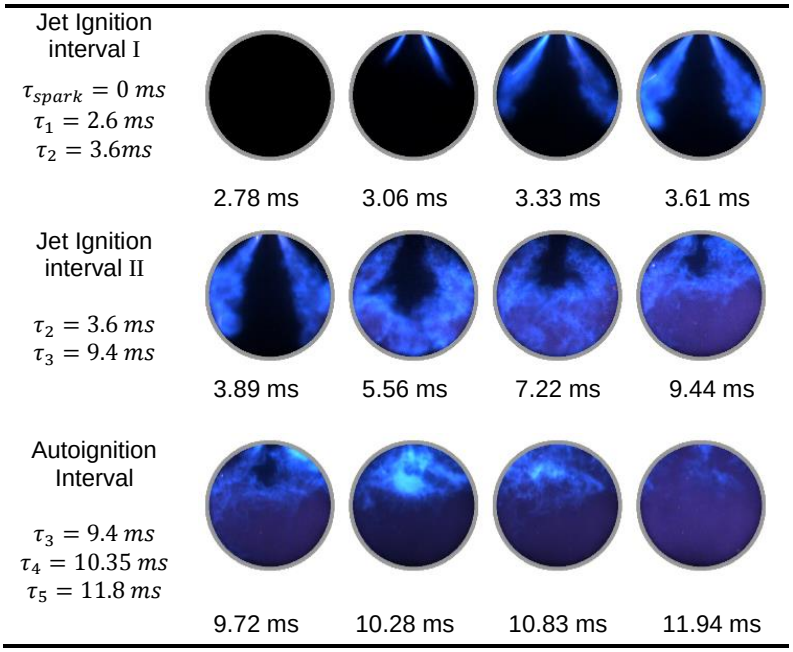

Figure 6-8. Optical images corresponding to characteristic time intervals for auxiliary fuel injection (dual orifice nozzle geometry, PW= 1.0 ms)

For the non-auxiliary fueled cases, the fundamental shape of the curve is different. Figure 6-9 gives the pressure trace and derivative data for the dual orifice, non-auxiliary fueled case. Jet ignition does not happen very quickly, and the second and third derivatives are nearly zero during the jet discharge. For this reason, the first derivative was used to determine the beginning of jet ignition. The transition from a negative dP/dt to a positive value after the spark discharge was found to identify the start of jet ignition in the main chamber.

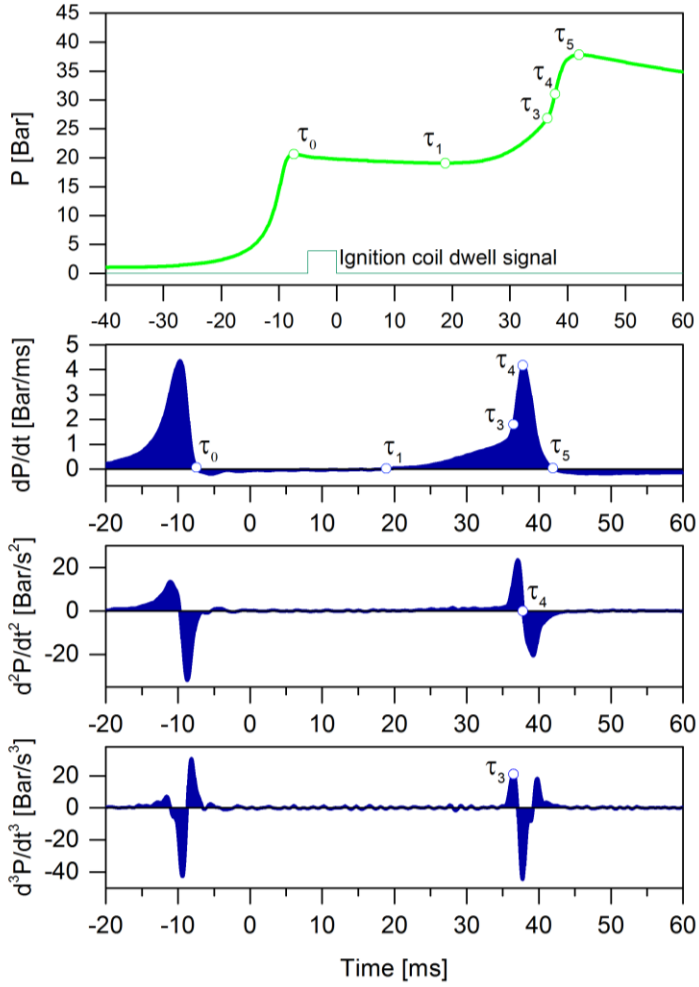

Figure 6-9. Pressure trace and derivative data for the dual orifice, non-auxiliary fueled case.

One interesting feature of the first derivative curve for this case is that the pressure rise due to jet ignition does not reach a local maximum before the onset of autoignition. The pressure rise

due to jet ignition continues to increase until the end-gas autoignition event. Thus, only two distinct intervals occur, one due to jet ignition and another due to autoignition. Figure 6-10 shows the optical images corresponding to these two intervals based on the pressure trace shown in Figure 6-9. It can be seen that the jet development and propagation is relatively slow, without much impingement onto the cylinder walls. A larger proportion of end gas is available to auto-ignite in this case.

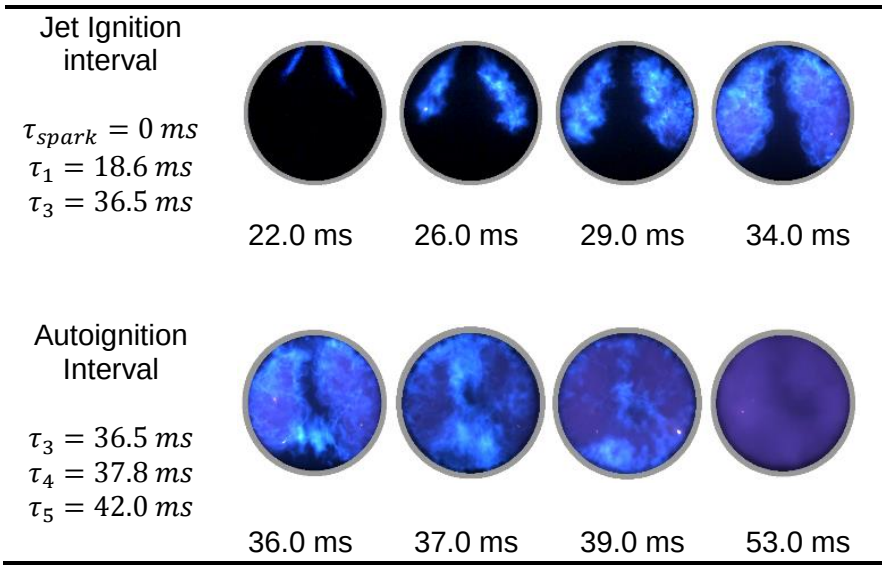

Figure 6-10. Optical images corresponding to characteristic time intervals for auxiliary fuel injection (dual orifice nozzle geometry, PW= 1.0 ms)

For different auxiliary fueling conditions and nozzle geometry, the pressure curves have different profiles and the characteristic points occur at different times. To compare these differences, the times were measured and plotted versus injector pulse width for both nozzles in Figure 6-11. The characteristic times are plotted using a logarithmic scale due to the large difference in scale between non-auxiliary fueled and fueled conditions. The mean data points are plotted and connected using a shape preserving spline, with error bands representing the standard error of the mean.

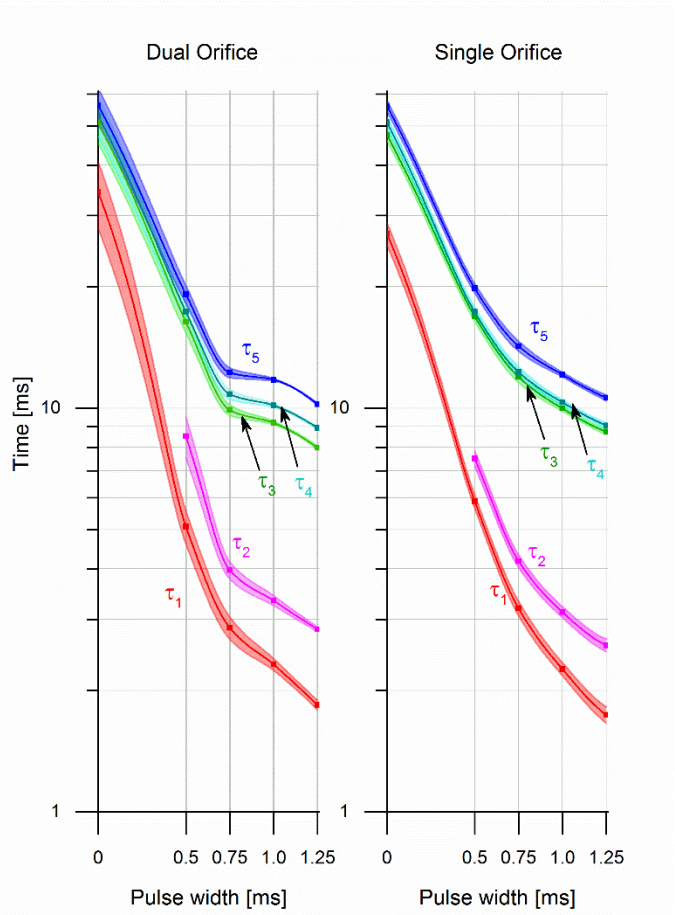

Figure 6-11. Characteristic time measurements as function of injector pulse width. Error bands correspond to the standard error of the mean.

The curves for the two different nozzles have similar time scales for the non-auxiliary fueled case, with wider error bands for the dual orifice nozzle implying increased combustion instability. Similar time scales for both nozzles also occur for the 1.25 ms pulse width conditions, with small error bars implying consistent and stable combustion. This behavior agrees with the burn duration analysis previously discussed. Additional insight can be obtained by comparing the 0.75 ms pulse width case for the two nozzles. At this fuel loading condition, the dual orifice has a faster autoignition onset than the single orifice. Increasing the injector pulse width to 1.0 ms decreases the time for the onset of jet ignition for the single orifice, but does not change the onset of autoignition very much for the dual orifice. This implies that for this condition the dual jets

have consumed most of the end gas in the path of the jet and increasing the fuel loading has less of an effect on the jets consuming the remaining portion of unburned fuel and air. Another feature that is distinct between the two nozzle geometries is that the separation between the τ_3 and τ_4 curves are different. τ_3 represents the onset of autoignition, while τ_4 represents the maximum rate of pressure rise due to autoignition. The fact that the τ_3 and τ_4 curves occur closer together implies that the maximum pressure rise rate due to autoignition for the single orifice occurs much closer to the onset of autoignition, whereas the pressure rise rate reaches a maximum later on for the dual orifice geometry.

6.4 Summary and Conclusions

Experiments of TJI were performed in an optically accessible rapid compression machine using liquid iso-octane and a custom low-flow fuel injector to overcome previous limitations of using liquid fuel in the pre-chamber. The effect of nozzle geometry and auxiliary fuel injection were investigated. Jet induced autoignition behavior was also studied in depth by considering high-speed images, and pressure derivative data.

It was found that the auxiliary fuel injection was critical for combustion stability. In addition, ignition distribution via the jet being channeled through one orifice or two was important for low-auxiliary fuel loading conditions. For non-auxiliary fueling conditions, the single orifice, D=1x 3.16 mm nozzle had better ignition performance than the dual orifice D=2x 2.26 mm nozzle as evident by the pressure traces and 0%-10% burn durations. However, when the mixture stoichiometry was such that it was easily ignitable in the pre-chamber, the minimum ignition energy was reached easily and both nozzles ignited the mixture reliably. This occurred at an injector pulse width of 0.75 ms, with best performance as the injector pulse width approached 1.25 ms. Varying the orifice geometry and stoichiometry also had an effect of the jet structure and fluid

mechanics. In particular, the volume of end-gas was different for the two nozzles and induced different autoignition behavior in the unburned mixture. The jet ignition and autoignition behavior was then characterized by using the pressure derivative data. Characteristic points and time intervals were identified, which corresponded to the physics that occurred as could be seen in the optical images. A time interval corresponding to jet penetration, jet impingement, and autoignition could be defined for the auxiliary fueled cases. However, only two intervals could be identified for the non-auxiliary fueled cases, one due to jet ignition and another due to autoignition of the unburned mixture. Increasing the injector pulse width was found to initiate jet ignition and autoignition faster, with little variation at injector pulse widths of 0.75, 1.00, and 1.25 ms.

CHAPTER 7: SUMMARY AND CONCLUDING REMARKS

This dissertation presents several experiments studying TJI using an optically accessible RCM. Chapter 1 gave a review of the literature and an introduction to TJI. Chapter 2 then described the experimental methods used, providing an overview of the RCM and a general testing procedure that was followed. However, each series of experiments used different TJI igniters and optical head geometries. Therefore, in each of the following chapters, the specific RCM and TJI configurations were introduced first, and then the experimental results were presented. The results from each set of TJI experiments form the basis of Chapters 3-6 in this body of work.

Chapter 3 presents experimental results on TJI without any auxiliary fuel injection, using gaseous propane as the fuel. In this chapter, several different orifice nozzle diameters and configurations were tested in the RCM. This effort expanded on TJI experiments documented in the literature by testing a broader range of orifice nozzles, and analyzing the pressure traces along with the high-speed images. Combustion visualization of the visible spectrum, as well as OH* and CH* radicals were performed. The pressure traces were analyzed by defining the 0-10% and 10-90% burn durations, similar to a mass fraction burned analysis. The 0-10% and 10-90% burn duration results indicate that if ignition can be initiated reliably in both the pre-chamber and main chamber, such as in a stoichiometric mixture, then a nozzle that will produce jets that are volumetrically distributed throughout the combustion chamber will be more advantageous and will consume the main chamber charge more rapidly. However as the mixture becomes leaner, a smaller orifice nozzle is desirable in order to reach the minimum ignition temperature. Visualization of the OH* radical species allowed us to obtain insight into where the

exothermic chemical reactions were occurring, with a high radical intensity occurring near the jet tip. The CH* visualization was useful as an alternative method of showing the flame boundary, which is important to determine the true structure of the jets. It was found that the OH* and CH* radicals overlap spatially throughout the jet structure.

In Chapter 4, a series of experiments were presented showing the behavior of TJI using a liquid propane auxiliary fueled pre-chamber. When operating with auxiliary injection, a substantial extension of the lean limit over the unfueled case was demonstrated. The combustion behavior was characterized, and further insights were obtained by optical observations of the jet ignition process. A pressure difference schematics was presented for λ global =1.71 and shows the flow interaction between the main-chamber and pre-chamber. A pressure ratio schematic was presented further characterizing the flow, and the flow was determined to only be choked during a portion of the jet discharge event. By observing the pressure traces, an apparent change in rate of combustion was seen in the main cylinder pressure, which was linked to the end of the jet discharge event. Combustion enhancement occurs as the jet is discharging, but the rate of combustion decreases when the jet discharge event ends. This was characterized by the excess pressure diagram where the main chamber pressure exceeds the pre-chamber pressure, causing a reversal of the flow direction into the pre-chamber in order for the gases to equilibrate. Furthermore, a unique flame structure with the auxiliary fueled TJI was observed that has not been seen in other optical studies, possibly indicating soot formation.

Chapter 5 presents dual injector TJI experiments performed using methane as the main chamber and pre-chamber fuel. This chapter also investigates the effect of charge dilution using both nitrogen and exhaust gases. In this chapter, the ability to ignite heavily diluted mixtures with TJI was demonstrated for both N_2 and EGR as the diluent. Control of the pre-chamber

stoichiometry and injected mass was shown to be critical to the TJI process; for the same global dilution level, different jet ignition behavior was observed from the pressure traces and optical images.

Chapter 6 utilizes an auxiliary fueled TJI system using liquid iso-octane as the auxiliary fuel. This chapter studies the effects of auxiliary fuel injection and ignition distribution due to single orifice and dual orifice nozzle geometry. Jet induced autoignition behavior was also studied in depth by considering high-speed images, and pressure derivative data. It was found that the auxiliary fuel injection was critical for combustion stability. In addition, ignition distribution via the jet being channeled through one orifice or two was important for low-auxiliary fuel loading conditions. For non-auxiliary fueling conditions, the single orifice, D=1x 3.16 mm nozzle had better ignition performance than the dual orifice D=2x 2.26 mm nozzle as evident by the pressure traces and 0%-10% burn durations. However, when the mixture stoichiometry was such that it was easily ignitable in the pre-chamber, the minimum ignition energy was reached easily and both nozzles ignited the mixture reliably. This occurred at an injector pulse width of 0.75 ms, with best performance as the injector pulse width approached 1.25 ms. Varying the orifice geometry and stoichiometry also had an effect of the jet structure and fluid mechanics. In particular, the volume of end-gas was different for the two nozzles and induced different autoignition behavior in the unburned mixture. The jet ignition and autoignition behavior was then characterized by using the pressure derivative data. Characteristic points and time intervals were identified, which corresponded to the physics that occurred as could be seen in the optical images. A time interval corresponding to jet penetration, jet impingement, and autoignition could be defined for the auxiliary fueled cases. However, only two intervals could be identified for the non-auxiliary fueled cases, one due to jet ignition and

another due to autoignition of the unburned mixture. Increasing the injector pulse width was found to initiate jet ignition and autoignition faster, with little variation at injector pulse widths of 0.75, 1.00, and 1.25 ms.

As a summary to this work, several novel aspects of TJI were studied and new insights were obtained. Nonetheless, TJI remains a challenging technical problem due to interacting physics of fluid mechanics, chemistry, and heat transfer. Due to the advantages of low temperature combustion, TJI will likely continue to be a topic of future research in industry as well as at MSU. Some recommendations for future work include Schlieren imaging to study the effect of the pre-chamber contents being displaced into the main chamber before hot ignition, and measuring hydrocarbon, NOx, and soot emissions for the conditions tested as this may limit the practical application of TJI in an engine.

APPENDICES

APPENDIX A: STOICHIOMETRY AND DILUTION CALCULATIONS

To demonstrate some of the stoichiometry calculations, properties for methane are used. When performing calculations for other fuels such as propane, the stoichiometric coefficients and molecular weights will change and care should be taken to keep track of these variables. The equation for stoichiometric combustion of methane in air, assuming complete combustion is

$$1\,CH_4 + 2\,(O_2 + 3.76N_2) \rightarrow 2\,H_2O + 1CO_2 + 7.52N_2 \qquad \text{A.1}$$

The air/fuel equivalence ratio, which is a non-dimensional air-fuel ratio, is defined as

$$\lambda = \frac{\frac{m_{air}}{m_{fuel}}}{\left(\frac{m_{air}}{m_{fuel}}\right)_{stoichiometric}} \qquad \text{A.2}$$

From equation A.1 the stoichiometric air-fuel ratio can then be calculated as

$$\left(\frac{m_{air}}{m_{fuel}}\right)_{stoichiometric} = \frac{9.52\ moles\ air \times 28.97\ \frac{kg}{mole}}{1\ mole\ methane\ \times 16.04\ \frac{kg}{mole}} = 17.19 \qquad \text{A.3}$$

For air fuel ratios other than λ=1, the ideal gas equation of state is used to calculate the masses based on the pressures read from a pressure sensor

$$m = \frac{P\,V}{\frac{R_u}{MW}\,T} \qquad \text{A.4}$$

Substituting equation X into equation X for the mass of air and fuel, we obtain the following relations

$$\lambda = \frac{\frac{m_{air}}{m_{fuel}}}{\left(\frac{m_{air}}{m_{fuel}}\right)_{stoichiometric}} = \frac{\left(\frac{P_{air}}{P_{fuel}}\right)\cdot\left(\frac{MW_{fuel}}{MW_{air}}\right)}{\left(\frac{m_{air}}{m_{fuel}}\right)_{stoichiometric}} \qquad \text{A.5}$$

$$\left(\frac{m_{air}}{m_{fuel}}\right) = \lambda \times \left(\frac{m_{air}}{m_{fuel}}\right)_{stoichiometric} \quad \text{A.6}$$

Due to conservation of mass, the mass of fuel and air with the piston at bottom dead center (BDC) will be the same as when the piston has reached the end of its stroke at top dead center (TDC), although the masses will occupy a smaller volume. Figure A-1 gives an illustration of the two control volumes used, the first with the piston at BDC and the second when the piston has reached TDC.

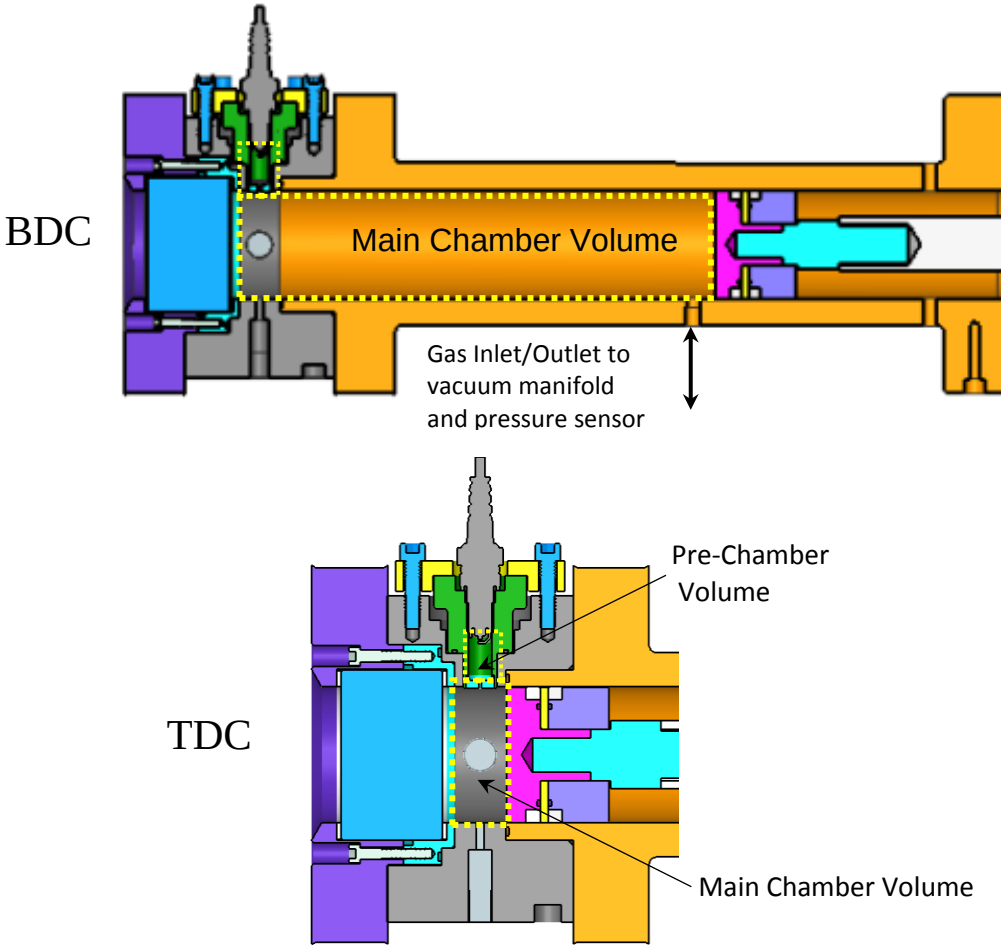

Figure A-1. Control Volumes used for stoichiometry calculations

Since we know the total mass of fuel and air that occupies the control volume that encompasses both the main-chamber volume and pre-chamber volume, we can determine the mass that is present in the pre-chamber only. If we assume that the mass is equally distributed in the main chamber and pre-chamber then the pre-chamber mass is given simply as the total mass times the ratio of pre-chamber volume to total volume. The mass of fuel and air in the pre-chamber before auxiliary injection can then be calculated from the following equations

$$m_{fuel,prechamber} = m_{fuel,total} \times \left(\frac{V_{prechamber}}{V_{total}}\right) \quad \text{A.7}$$

$$m_{air,prechamber} = m_{air,total} \times \left(\frac{V_{prechamber}}{V_{total}}\right) \quad \text{A.8}$$

In the case of no auxiliary injection, the air-fuel ratio will be the same in the pre-chamber as in the main chamber and no further calculations need to be made. If operating with auxiliary fuel addition in the pre-chamber, as illustrated in figure A-2a, or auxiliary air and fuel addition as shown in figure A-2b, the injected mass needs to be accounted for. There are a few different ways to estimate the pre-chamber stoichiometry depending on the assumptions that are made about the displacement of the gases in the pre-chamber.

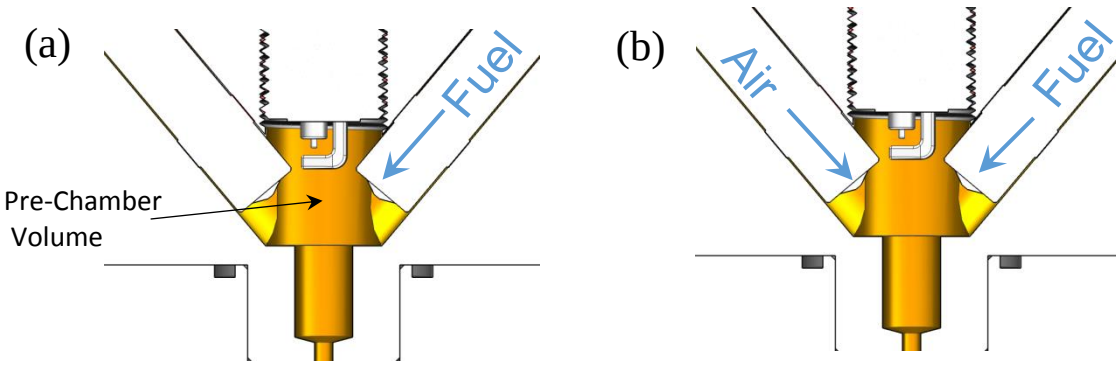

Figure A-2. (a) Auxiliary fuel injection only (second injector is not used),
(b) Auxiliary air and fuel injection into the pre-chamber volume

When operating with auxiliary fuel injection, the fuel is injected during the compression stroke. In this case, it can be theorized that none of the pre-chamber contents are displaced during the auxiliary fuel injection event, and that none of the auxiliary fuel leaves the pre-chamber since the main-chamber mixture is simultaneously being compressed into the pre-chamber. The total fuel mass in the pre-chamber is then given as

$$m_{fuel,prechamber} = \quad m_{fuel,prechamber(initial)} + m_{fuel,injected} \qquad \text{A.9}$$

For auxiliary fuel addition only, the mass of air in the pre-chamber remains the same, and the pre-chamber λ can then be estimated. If auxiliary air injection is used, then the same principles apply, except that the mass of air is now taken into account.

In order to compare between tests without auxiliary injection, and tests where there is additional mass injected it is important to keep the total mass of the system constant. Equation A.4 gives this relationship. Basically, this means that for a test with auxiliary injection there is slightly less mass present in the initial charge since this additional mass will be injected later on so that the total mass remains approximately constant.

$$\text{Total mass} = \left(m_{air} + m_{CH_4}\right)_{Initial} + \left(m_{air} + m_{CH_4}\right)_{Injected} \qquad \text{A.10}$$

Another method to calculate the pre-chamber stoichiometry is to assume that all of the pre-chamber contents are displaced. In this case, the pre-chamber mixture has the exact stoichiometry as the mixture that is being injected.

For some experimental tests, it may be interesting to see the effect of increasing dilution levels. The dilution level is given as the ratio of the mass of the diluent species to the total mass of the mixture. A.11 gives the dilution percentage for nitrogen as the diluent species, while A.12 gives the relationship for exhaust gases

$$N_2\ Dilution\ \% = \frac{m_{N_2}}{m_{air} + m_{CH_4} + m_{N_2}} \times 100\% \quad \text{A.11}$$

$$EGR\ Dilution\ \% = \frac{m_{egr}}{m_{air} + m_{CH_4} + m_{egr}} \times 100\% \quad \text{A.12}$$

Again, for these tests we will likely want to keep the total mass constant for the initial charge present. For example, if the first test is performed without any auxiliary injection, the initial charge will have a certain value for the total mass present. If the next test includes auxiliary injection of fuel, or fuel and air, the initial mass will be slightly less to compensate for the additional mass that is being injected. This allows for the compressed pressure to be approximately the same for both tests. Equations A.12 and A.14 give the mathematical relationships for the total mass for N2 dilution studies and for EGR studies, respectively.

$$\text{Total mass} = \left(m_{air} + m_{CH_4} + m_{N_2}\right)_{Initial} + \left(m_{air} + m_{CH_4}\right)_{Injected} \quad \text{A.13}$$

$$\text{Total mass} = \left(m_{air} + m_{CH_4} + m_{egr}\right)_{Initial} + \left(m_{air} + m_{CH_4}\right)_{Injected} \quad \text{A.14}$$

When using Auxiliary injection one last relationship is needed to fully constrain the system of equations. If the total mass is held constant, we need to specify what percent of the mixture mass will be initially present, and what percent of the mass will be delivered via auxiliary injection.

Here, the injected mass fraction is defined as the ratio of the injected mass to the total mass present and is given by equation A.15

$$\frac{m_{injected}}{m_{total}} = \frac{\left(m_{air} + m_{CH_4}\right)_{Injected}}{\left(m_{air} + m_{CH_4} + m_{N_2} + m_{egr}\right)_{total}} \times 100\ \% \qquad \text{A.15}$$

This equation is written in the most general way possible and includes terms for auxiliary air and fuel addition, nitrogen dilution, and exhaust gas dilution. For a simpler testing configuration, some of these terms will be zero and the equation will have a different form. For example, for auxiliary fuel only, and without N2 or EGR dilution, the injected mass fraction takes the following form

$$\frac{m_{injected}}{m_{total}} = \frac{\left(m_{CH_4}\right)_{Injected}}{\left(m_{air} + m_{CH_4}\right)_{total}} \times 100\ \% \qquad \text{A.15}$$

APPENDIX B: HEAT TRANSFER ANALYSIS

During TJI a hot jet travels through one or more nozzle orifices, and these hot jets will lose some enthalpy as they exchange heat with the cooler nozzle walls. The magnitude of this heat exchange depends on several factors including the nozzle wall temperature, flow velocity and residence time, thermal conductivity, among others. The actual flow and heat transfer processes are quite complex, and difficult to analyze mathematically without making some simplifying assumptions about the flow. The first assumption to be made is that combustion occurs in the pre-chamber instantaneously, with no heat-transfer losses to the pre-chamber walls. In this model, the pre-chamber can be thought of as a thermal reservoir that supplies a non-reacting, hot mixture of combustion products through the orifice at the adiabatic flame temperature. Another assumption made is that of a "slug flow" velocity profile and that the hydrodynamic boundary layer will be very thin.

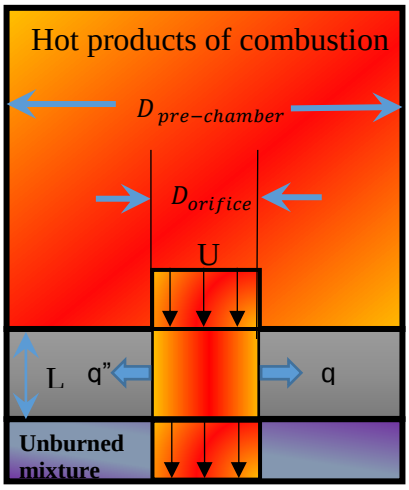

Figure B-1. Heat transfer schematic of pre-chamber and nozzle orifice, assuming a "slug flow" velocity profile.

Figure B-1 gives an illustration of the pre-chamber and nozzle assembly that conveys the concept of the pre-chamber acting as a thermal reservoir and shows the "slug flow" velocity profile that is assumed. The important dimensions are also labeled including the pre-chamber diameter, orifice diameter, and orifice length. In order to simplify the mathematics, for this problem a two-dimensional slot geometry will be used for the orifice with a Cartesian coordinate system centered at the orifice inlet as shown in Figure B-2.

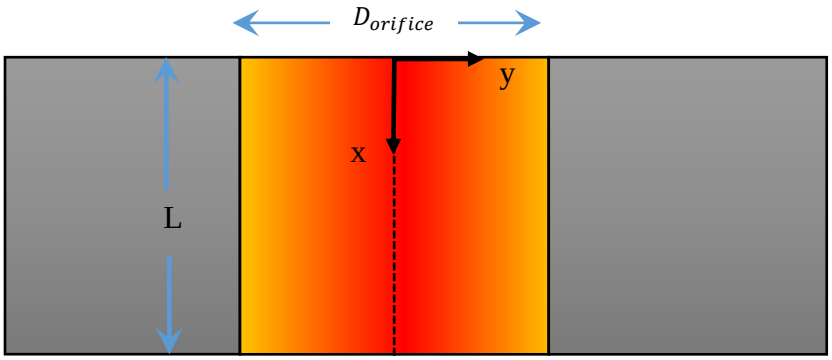

Figure B-2. Coordinate system and dimension of nozzle orifice.

The heat diffusion equation which governs the spatial and temporal distribution of heat in a media is given by the following partial differential equation (assuming no energy source terms).

$$\rho c \left[\frac{\partial T}{\partial t} + \nabla \cdot (Tu) \right] = \nabla \cdot (k \nabla \mathrm{T}) \qquad \text{B.1}$$

This simplifies to equation B.2 for two-dimensional flow, constant thermal properties, and neglect stream-wise diffusion

$$\alpha \frac{\partial^2 T}{\partial y^2} = U \frac{\partial T}{\partial x} \quad \text{B.2}$$

It is useful to make the equation non-dimensional by scaling the variables as follows

$$\theta = \frac{T - T_c}{T_h - T_c} \quad \text{B.3}$$

$$\bar{x} = \frac{x}{L} \quad \text{B.4}$$

$$\bar{y} = \frac{y}{D/2} \quad \text{B.5}$$

The non-dimensional equation is now given by

$$\frac{\partial^2 \theta}{\partial \bar{y}^2} = \left[4\, Re \cdot Pr \cdot \frac{D}{L}\right] \cdot \frac{\partial \theta}{\partial \bar{x}} \quad \text{B.6}$$

Where Re is the Reynolds number, Pr is the Prandtl number, and D/L is the aspect ratio of the nozzle. The specified boundary conditions for this problem are as follows

BC1:	$\theta(\bar{x} = 0, \bar{y}) = 1$	Known temperature of the fluid at the inlet of the orifice
BC2:	$\frac{\partial \theta}{\partial y}(\bar{x}, \bar{y} = 0) = 0$	Symmetry condition
BC3:	$\theta(\bar{x}, \bar{y} = 1) = 0$	Constant temperature at the nozzle walls

The energy equation for the fluid can now be solved using the method of separation of variables in order to yield the temperature distribution

$$\theta(\bar{x},\bar{y}) = \sum_{n=1}^{\infty} A_n e^{-C\lambda_n{}^2\bar{x}} \cos\lambda_n\bar{y} \qquad \text{B.7}$$

The constant C is due to the non-dimensionalization of the equations and is given by

$$C = \frac{1}{4Re\,\mathrm{Pr}\,D/L} \qquad \text{B.8}$$

The eigenvalues λ_n are given by solving the characteristic equation

$$\lambda_n = \pm(2m+1)\frac{\pi}{2} \qquad \text{B.9}$$

And the series coefficients A_n are given by the following expression obtained by invoking orthogonality of the eignefunctions

$$A_n = \frac{2\sin\lambda_n}{\lambda_n} = \frac{4(-1)^n}{(2m+1)\pi} \qquad \text{B.10}$$

Now that the temperature distribution has been determined, an energy balance at the orifice wall can be performed and a local heat transfer coefficient, h, can be defined.

$$h(T_h - T_c) = -\frac{\partial T}{\partial y}\bigg|_{wall} \qquad \text{B.11}$$

$$h = \frac{-\frac{\partial T}{\partial y}\Big|_{wall}}{(T_h - T_c)} \qquad \text{B.12}$$

When using the non-dimensional variables defined earlier, the form of the heat transfer coefficient simplifies to

$$h = -\frac{k}{L} \cdot \left.\frac{\partial \theta}{\partial y}\right|_{wall} \tag{B.13}$$

The corresponding Nusselt number is then given by

$$Nu_x = \frac{hL}{k} = -\left.\frac{\partial \theta}{\partial y}\right|_{wall} \tag{B.14}$$

The total heat transfer to the nozzle walls is characterized by the total Nusselt Number, which is obtained by integrating along the orifice length, from $\bar{x} = 0$ to $\bar{x} = 1$.

$$Nu = \int_{\bar{x}=0}^{\bar{x}=1} \frac{hL}{k}\, dx = \int_{\bar{x}=0}^{\bar{x}=1} -\left.\frac{\partial \theta}{\partial y}\right|_{wall} dx \tag{B.15}$$

$$Nu = \sum_{n=1}^{\infty} \frac{A_n \lambda_n \sin \lambda_n}{C\, \lambda_n} \left(1 - e^{-C\lambda_n{}^2}\right) \tag{B.16}$$

Thus, the convection heat transfer is simply characterized by calculating the non-dimensional temperature gradient at the surface of the nozzle walls. The solution is in terms of an infinite series, and the heat transfer coefficient can be computed by evaluating properties and writing a numerical code that can compute enough terms of the series so that a solution will be converged upon.

APPENDIX C: SCHLIEREN OPTICAL HEAD

An optical head was designed so that a sheet of light can be passed through the sides of the head, while direct combustion visualization can be performed through the end window access.

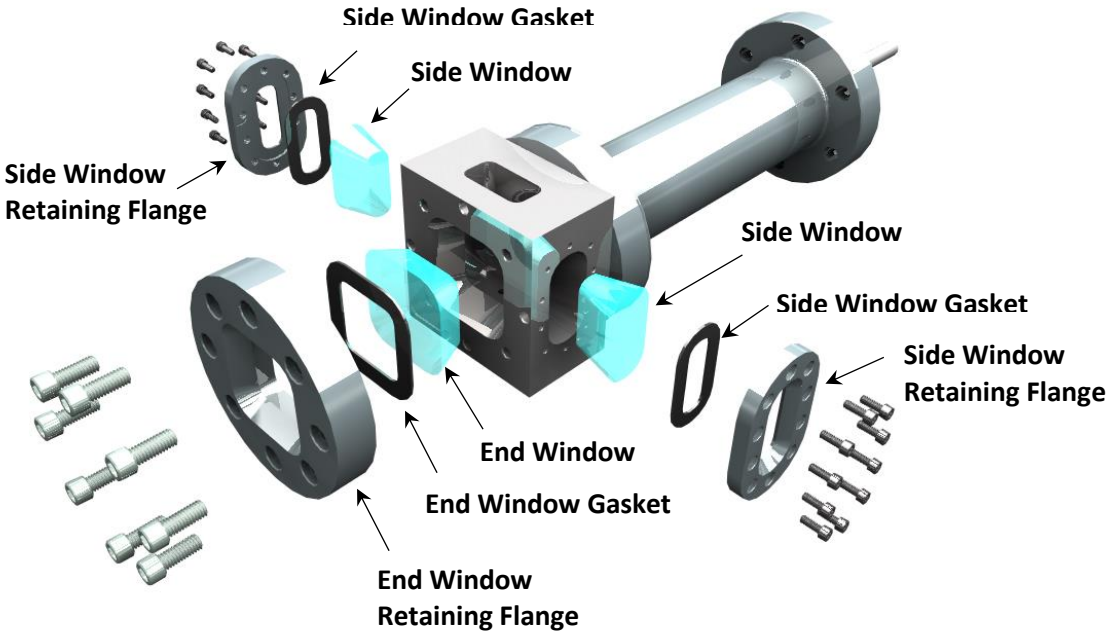

Figure C-1. Exploded view of Schlieren optical head assembly

REFERENCES

REFERENCES

[1] J.E. Dec, Advanced compression-ignition engines—understanding the in-cylinder processes, Proceedings of the Combustion Institute 32 (2009) 2727-2742.

[2] M.D. Checkel, D.S.-K. Ting, Turbulence Effects on Developing Turbulent Flames in a Constant Volume Combustion Chamber, International Congress and Expoistion, SAE International, Detroit, Michigan, 1993.

[3] R.M. Modien, M.D. Checkel, J.D. Dale, The Effect of Enhanced Ignition Systems on Early Flame Development in Quiescent and Turbulent Conditions, International Congress and Exposition, SAE International, Detroit, Michigan, 1991.

[4] J.D.D.a.A.K. Oppenheim, Enhanced Ignition for I.C. Engines with Premixed Gases, SAE Technical Paper 810146, doi:10.4271/810146(1981).

[5] E. Toulson, H.J. Schock, W.P. Attard, A Review of Pre-Chamber Initiated Jet Ignition Combustion Systems, SAE Technical Paper 2010-01-2263, 2010.

[6] R. Sadanandan, D. Markus, R. Schießl, U. Maas, J. Olofsson, H. Seyfried, M. Richter, M. Aldén, Detailed investigation of ignition by hot gas jets, Proceedings of the Combustion Institute 31 (2007) 719-726.

[7] H. Schock, G. Zhu, E. Toulson, T.R. Stuecken, Internal combustion engine, Google Patents, 2014.

[8] C.K. Law, Combustion Physics, Cambridge University Press2006.

[9] I. Glassman, R.A. Yetter, Chapter 7 - Ignition, in: I. Glassman, R.A. Yetter (Eds.), Combustion (Fourth Edition), Academic Press, Burlington, 2008, pp. 379-408.

[10] R.W. Schefer, W.G. Houf, T.C. Williams, B. Bourne, J. Colton, Characterization of high-pressure, underexpanded hydrogen-jet flames, International Journal of Hydrogen Energy 32 (2007) 2081-2093.

[11] S. Turns, An Introduction to Combustion: Concepts and Applications, 3rd ed., McGraw Hill.

[12] A.N.N. Semenov, Chapter 1 - THERMAL IGNITION [1]*, in: A.N.N. Semenov (Ed.), Some Problems of Chemical Kinetics and Reactivity, Pergamon1959, pp. 1-18.

[13] A.N.N. Semenov, Chapter 2 - CHAIN SELF-IGNITION, in: A.N.N. Semenov (Ed.), Some Problems of Chemical Kinetics and Reactivity, Pergamon1959, pp. 19-46.

[14] B.F. Gray, Critical behaviour in chemically reacting systems: I—Difficulties with the Semenov theory, Combustion and Flame 20 (1973) 313-316.

[15] B.F. Gray, Critical behaviour in chemically reacting systems: II—An exactly soluble model, Combustion and Flame 20 (1973) 317-325.

[16] J.M. Kuchta, Investigation of Fire and Explosion Accidents in the Chemical, Mining, and Fuel-Related Industires- A Manual, Bureau of Mines, Bulletin 680.

[17] Appendix E - Flammability limits in air, in: I.G.A.Y.G. Glumac (Ed.), Combustion (Fifth Edition), Academic Press, Boston, 2015, pp. 689-696.

[18] J.D. Dale, M.D. Checkel, P.R. Smy, Application of high energy ignition systems to engines, Progress in Energy and Combustion Science 23 (1997) 379-398.

[19] S.E. Hosseini, S. Salehirad, M.A. Wahid, M.M. Sies, A. Saat, Effect of diluted and preheated oxidizer on the emission of methane flameless combustion, AIP Conference Proceedings 1440 (2012) 1309-1312.

[20] M. Gholamisheeri, B.C. Thelen, G.R. Gentz, I.S. Wichman, E. Toulson, Rapid compression machine study of a premixed, variable inlet density and flow rate, confined turbulent jet, Combustion and Flame 169 (2016) 321-332.

[21] V. Vuorinen, J. Yu, S. Tirunagari, O. Kaario, M. Larmi, C. Duwig, B.J. Boersma, Large-eddy simulation of highly underexpanded transient gas jets, Physics of Fluids 25 (2013) 016101.

[22] E. Franquet, V. Perrier, S. Gibout, P. Bruel, Free underexpanded jets in a quiescent medium: A review, Progress in Aerospace Sciences 77 (2015) 25-53.

[23] G. Pawlak, C. Marugan Cruz, C. Martínez Bazán, P. García Hrdy, Experimental characterization of starting jet dynamics, Fluid Dynamics Research 39 (2007) 711-730.

[24] H. Daneshyar, J.M.C. Mendes-Lopes, G.S.S. Ludford, Effect of strain fields on burning rate, Symposium (International) on Combustion 19 (1982) 413-421.

[25] A.K. Oppenheim, Prospects for Combustion in Piston Engines, SAE 2002 World Congress, SAE International, Detroit, Michigan, 2002.

[26] A.K. Oppenheim, A.L. Kuhl, Paving the Way to Controlled Combustion Engines (CCE), SAE Technical Paper 951961, 1995.

[27] L.A. Gussak, Karpov, V., and Tikhonov, Y., The Application of Lag-Process in Prechamber Engines, SAE Technical Paper 790692, doi:doi:10.4271/790692.(1979).

[28] L.A. Gussak, Turkish, M., and Siegla, D., High Chemical Activity of Incomplete Combustion Products and a Method of Prechamber Torch Ignition for Avalanche

Activation of Combustion in Internal Combustion Engines, SAE Technical Paper 750890, (1975).

[29] P. Wolanski, A.K. Oppenheim, Controlled Combustion Engines (CCE), SAE International, 1999.

[30] D.M. Hensinger, J.A. Maxson, K. Hom, A.K. Oppenheim, Jet Plume Injection and Combustion, SAE Technical Paper 920414, 1992.

[31] J.A. Maxson, D.M. Hensinger, K. Hom, A.K. Oppenheim, Performance of Multiple Stream Pulsed Jet Combustion Systems, SAE International, 1991.

[32] J.A. Maxson, A.K. Oppenheim, Pulsed jet combustion—Key to a refinement of the stratified charge concept, Symposium (International) on Combustion 23 (1991) 1041-1046.

[33] E. Murase, S. Ono, K. Hanada, A.K. Oppenheim, Pulsed Combustion Jet Ignition in Lean Mixtures, SAE Technical Paper 942048, 1994.

[34] E. Murase, K. Hanada, Enhancement of Combustion by Injection of Radicals, SAE Technical Paper 2001-01-0194, 2000.

[35] E. Murase, K. Hanada, Control of the Start of HCCI Combustion by Pulsed Flame Jet, SAE Technical Paper 2002-01-2867, 2002.

[36] G. Lumsden, H.C. Watson, Optimum Control of an S.I. Engine with a λ=5 Capability, SAE Technical Paper 950689, 1995.

[37] E. Toulson, H.C. Watson, W.P. Attard, Gas Assisted Jet Ignition of Ultra-Lean LPG in a Spark Ignition Engine, SAE Technical Paper 2009-01-0506, 2009.

[38] N. Glasson, G. Lumsden, R. Dingli, H. Watson, Development of the HAJI System for a Multi-Cylinder Spark Ignition Engine, SAE Technical Paper 961104, 1996.

[39] E.K. Anderson, W.P. Attard, A. Brown, P. Litke, K. Grinstead, J. Hoke, Experimental Study of a Pre-Chamber Jet Igniter in a Turbocharged Rotax 914 Aircraft Engine, SAE Technical Paper 2013-01-1629, 2013.

[40] W.P. Attard, P. Parsons, Flame Kernel Development for a Spark Initiated Pre-Chamber Combustion System Capable of High Load, High Efficiency and Near Zero NOx Emissions, SAE Int. J. Engines 3 (2010) 408-427.

[41] W.P. Attard, H. Blaxill, A Gasoline Fueled Pre-Chamber Jet Ignition Combustion System at Unthrottled Conditions, SAE Int. J. Engines 5 (2012) 315-329.

[42] W.P. Attard, H. Blaxill, E.K. Anderson, P. Litke, Knock Limit Extension with a Gasoline Fueled Pre-Chamber Jet Igniter in a Modern Vehicle Powertrain, SAE Int. J. Engines 5 (2012) 1201-1215.

[43] W.P. Attard, H. Blaxill, A Lean Burn Gasoline Fueled Pre-Chamber Jet Ignition Combustion System Achieving High Efficiency and Low NOx at Part Load, SAE Technical Paper 2012-01-1146, 2012.

[44] W.P. Attard, H. Blaxill, A Single Fuel Pre-Chamber Jet Ignition Powertrain Achieving High Load, High Efficiency and Near Zero NOx Emissions, SAE Int. J. Engines 5 (2011) 734-746.

[45] W.P. Attard, E. Toulson, A. Huisjen, X. Chen, G. Zhu, H. Schock, Spark Ignition and Pre-Chamber Turbulent Jet Ignition Combustion Visualization, SAE Technical Paper 2012-01-0823, 2012.

[46] E. Toulson, A. Huisjen, X. Chen, C. Squibb, G. Zhu, H. Schock, W.P. Attard, Visualization of Propane and Natural Gas Spark Ignition and Turbulent Jet Ignition Combustion. SAE Technical Paper: 2013-32-0002, SAE Int. J. Engines 5 (2012) 1821-1835.

[47] G. Gentz, B. Thelen, M. Gholamisheeri, P. Litke, A. Brown, J. Hoke, E. Toulson, A study of the influence of orifice diameter on a turbulent jet ignition system through combustion visualization and performance characterization in a rapid compression machine, Appl. Therm. Eng. 81 (2015) 399-411.

[48] G. Gentz, B. Thelen, P. Litke, J. Hoke, E. Toulson, Combustion Visualization, Performance, and CFD Modeling of a Pre-Chamber Turbulent Jet Ignition System in a Rapid Compression Machine, SAE Int. J. Engines 8 (2015) 538-546.

[49] R.M. Modien, M.D. Checkel, J.D. Dale, The Effect of Enhanced Ignition Systems on Early Flame Development in Quiescent and Turbulent Conditions, SAE Technical Paper: 910564, SAE International, 1991.

[50] S. Shiga, S. Ozone, H.T.C. Machacon, T. Karasawa, H. Nakamura, T. Ueda, N. Jingu, Z. Huang, M. Tsue, M. Kono, A study of the combustion and emission characteristics of compressed-natural-gas direct-injection stratified combustion using a rapid-compression-machine, Combustion and Flame 129 (2002) 1-10.

[51] C.A. Schneider, W.S. Rasband, K.W. Eliceiri, NIH Image to ImageJ: 25 years of image analysis, Nat Meth 9 (2012) 671-675.

[52] M. Jakob, T. Hülser, A. Janssen, P. Adomeit, S. Pischinger, G. Grünefeld, Simultaneous high-speed visualization of soot luminosity and OH∗ chemiluminescence of alternative-fuel combustion in a HSDI diesel engine under realistic operating conditions, Combustion and Flame 159 (2012) 2516-2529.

[53] E. Mancaruso, B.M. Vaglieco, Spectroscopic measurements of premixed combustion in diesel engine, Fuel 90 (2011) 511-520.

[54] J. Zhang, W. Jing, T. Fang, High speed imaging of OH* chemiluminescence and natural luminosity of low temperature diesel spray combustion, Fuel 99 (2012) 226-234.

[55] L.C.R. Johansen, S. Hemdal, In cylinder visualization of stratified combustion of E85 and main sources of soot formation, Fuel 159 (2015) 392-411.

[56] A.M. Rusly, M.K. Le, S. Kook, E.R. Hawkes, The shortening of lift-off length associated with jet–wall and jet–jet interaction in a small-bore optical diesel engine, Fuel 125 (2014) 1-14.

[57] A. Ghorbani, D. Markus, G. Steinhilber, U. Maas, A numerical approach to investigate the maximum permissible nozzle diameter in explosion by hot turbulent jets, Journal of Loss Prevention in the Process Industries 36 (2015) 539-543.

[58] A. Ghorbani, G. Steinhilber, D. Markus, U. Maas, Ignition by transient hot turbulent jets: An investigation of ignition mechanisms by means of a PDF/REDIM method, Proceedings of the Combustion Institute 35 (2015) 2191-2198.

[59] J. Heywood, Internal Combustion Engine Fundamentals, McGraw Hill1988.